Norwegian University
of Life Sciences

Master's Thesis 2021 30 ECTS
Faculty of Science and Techonolgy
Associate Professor Themistoklis Tsalkatidis

Three-Dimensional Finite Element Analysis of a Bolted Steel-Timber Composite Shear Connection

Lars Christoffer Haug Rath
Structural Engineering and Architecture

Preface

This thesis marks the end of a five-year master's study in Structural Engineering and Architecture at the Norwegian University of Life Sciences. The thesis investigates numerical modelling of steel-timber composite connections, based on experimental testing, with the use of FEM-software.

The motivation for this thesis came from a deep interest into the field of timber construction and FEM-software, which has emerged during my years as a student at NMBU. Timber construction has strong traditions in Norway and is currently among the leading nations, when it comes to modern applications of timber. New large-scale timber structures are being built at an increasing rate, which indicates that expertise in this field will be sought after.

However, this does not mean that there is little left to be investigated when it comes to timber construction. Timber has yet to make a noticeable impact on the modern building practice in large parts of the world. Thus, further research will be necessary to make its use widespread and to develop more innovative solutions. This thesis can hopefully contribute to that.

I want to express my deepest appreciation to Associate Professor Themistoklis Tsalkatidis for his guidance throughout this project. His straightforward and constructive feedback encouraged me to put my best efforts into this work.

Finally, I wish to thank my family and closest friends for all the support that I have received during my years at NMBU.

Ås, June 2021

Lars Christoffer Haug Rath

Lars Christoffer Haug Rath

Abstract

Timber use in construction has been growing in popularity in recent years. Increased awareness regarding sustainability is one of the main causes for this, as timber shows evidence of being less harmful to the environment than other construction materials. The construction industry contributes to nearly 40 % of the global CO_2 emissions. Efforts to develop and implement sustainable solutions will therefore be necessary, to address these concerning figures. It is likely that timber will take part in some of these solutions.

A construction technique that has received increased interest recently, is steel-timber composite (STC) structures. This method aims to limit the use of concrete and steel, by replacing some of the load-bearing elements with timber. In order to join different materials together, knowledge about hybrid connections is essential.

The purpose of this thesis is to advance the research on STC connections, by conducting a finite element analysis (FEA) of a bolted STC shear connection. The connection consists of two Dahurian larch glulam elements, which are bolted to the flanges of a steel H-section, using four 6 mm bolts. A study where this connection was subjected to a pull-out test, acted as the basis for this work. The load-slip results from the experimental study were used to assess the accuracy of the FEA.

The FEM-software, Ansys Mechanical R2 2020, was used for conducting the analysis. As timber is an anisotropic material, capturing its behaviour in a numerical simulation is challenging. As a result, several modelling approaches have been developed for analysing STC connections. For this work, a method called the "foundation material model" was used.

Promising results were obtained by the analysis, and a conservative estimation of the connection capacity was provided. Similar to the experimental study, the bolts in the model were the critical parts that failed first. A two-hinge yield of the bolts developed in the model, which is the same failure mode as the experiment. The bolts failed when 47.5 kN had been applied, which is 88 % of that of the physical test. The resulting slip of the model was 5.4 mm, as opposed to the 7.5 mm seen in the experiment. Some of the other main observations from the experiment could also be captured by the model. This included initial no-slip, caused by bolt pretension, and embedment of bolt heads.

Further work involving physical tests is recommended to enable better determination of the timber material properties. Other connection configurations can also be examined, in order to investigate the potential of the foundation material model.

Sammendrag

Bruk av treverk i byggebransjen har økt i popularitet de siste årene. Større bevissthet rundt bærekraft er en av hovedgrunnene til dette, ettersom treverk viser tegn på å være mindre skadelig for miljøet enn andre konstruksjonsmaterialer. Byggeindustrien bidrar til nesten 40 % av det globale CO_2 utslippet. Innsats rettet mot utvikling og implementering av bærekraftige løsninger vil derfor være nødvendig, for å adressere disse dystre tallene. Det er sannsynlig at treverk kommer til å bidra til noen av disse løsningene.

En byggemåte som har fått større interesse i det siste, er stål-tre kompositt (STK) strukturer. Denne metoden søker å begrense bruken av betong og stål, ved å erstatte deler av de lastbærende elementene med treverk. For å forbinde forskjellige materialer sammen, er kunnskap om hybridforbindelser essensielt.

Formålet med denne avhandlingen er å videreføre forskningen på STK forbindelser, ved å utføre en finite element analyse (FEA) av en boltet STK skjærforbindelse. Forbindelsen består av to mongollerk limtre elementer, som er boltet fast på flensene til en stål H-profil, ved bruk av fire 6 mm bolter. En studie hvor denne forbindelsen ble utsatt for en "pull-out" test, fungerte som et grunnlag for dette arbeidet. Last-deformasjons-resultatene fra den eksperimentelle studien ble brukt for å vurdere nøyaktigheten av FEA'en.

FEM-programvaren, Ansys Mechanical R2 2020, ble brukt i gjennomføringen av analysen. Siden treverk er et anisotropisk materiale, er det å fange dets oppførsel i en numerisk simulering krevende. Som et resultat, er det utviklet flere fremgangsmåter for å modellere STK forbindelser. For dette arbeidet, ble en metode kalt "foundation material model" brukt.

Lovende resultater ble oppnådd av analysen, og en konservativ estimering av forbindelseskapasiteten ble gitt. I likhet med den eksperimentelle studien, var boltene i modellen de kritiske delene som feilet først. To-leddet flyt i boltene utviklet seg i modellen, noe som er den samme bruddformen som i eksperimentet. Boltene feilet da 47.5 kN hadde blitt påført, noe som er 88 % av det i den fysiske testen. Den resulterende deformasjonen i modellen var 5.4 mm, i motsetning til de 7.5 mm fra eksperimentet. Noen av andre hovedobservasjonene fra eksperimentet kunne også bli fanget opp av modellen. Dette inkluderer innledende "no-slip", forårsaket av forstramming av boltene, og inntrenging av boltehodene.

Videre arbeid ved fysiske tester er anbefalt for å kunne bestemme materialverdiene til treverket bedre. Andre knutepunktskonfigurasjoner kan også bli undersøkt, for å utforske potensialet til foundation material modellen.

Contents

List of Figures

List of Tables

1. Introduction

1.1 Background

Timber use in construction has been growing in popularity in recent years, particularly in parts of Europe and North America (Ahmed & Arocho, 2020; Toppinen et al., 2018). Increased focus on sustainability has been one of the main contributing factors, as timber shows better environmental and sustainability credentials than other construction materials (Woodard & Milner, 2016). A 2019 report by the International Energy Agency (IEA) shows that global emissions tied to the construction industry keep rising every year. In 2018 the construction industry contributed to 39 % of the global CO_2 emissions, which was a 2 % increase from 2017 (IEA, 2019). Timber is the only renewable construction material, therefore it is expected that it will play an important role in turning the construction industry sustainable.

Apart from sustainability, other benefits to timber construction include favourable weight-to-strength ratio, durability, ease of assembly and cost competitiveness (Ramage et al., 2017). Developments in modern wood products such as glued-laminated timber (glulam) and cross-laminated timber (CLT), have made it possible to utilize timber in new applications. Traditionally wood has been limited by the size and quality of the tree it is harvested from, but these engineered products make it possible to improve the capabilities of wood. This has led to increasingly complex timber structures being constructed. One example is the recently completed Mjøstårnet in Norway, which with a height of 85.4 meters makes it the tallest timber building in the world today (Abrahamsen & Moelven Limtre AS, 2018). However, replacing the current building practice dominated by steel and concrete completely with timber, might not be feasible in most parts of the world. The availability of quality timber can be limited, or certain areas might pose challenges which makes timber less suitable. Instead, alternatives where timber is partially replacing these materials should be explored (Valipour, n.d).

A construction technique that has received increased interest recently is steel-timber composite (STC) structures. These are known as hybrid structures where multiple materials are combined to form the main load-bearing components. Traditional timber constructions typically use fasteners made from steel. However, true hybridization of a structure is done on a larger scale, where the different materials complement each other to overcome their weaknesses (Schober & Tannert, 2016). The idea is to limit the use of concrete, as this constitutes a major part of emissions in construction (De Brito & Kurda, 2021). By using steel as the framework for these structures, timber can replace concrete in parts such as floors and walls (Loss et al., 2016; Nouri et al., 2019; Vogiatzis et al., 2019). To realize these structures, knowledge about ways of connecting them is crucial.

Connections are the most critical components of any structure (Schober & Tannert, 2016). Thus, a clear understanding about how they perform and ways of designing them is essential, in order to construct effective and safe structures (Tsalkatidis et al., 2018). Steel-timber composite structures are still relatively new, which means that further research into STC connections is going to be necessary. Modern engineering tools, such as software based on the finite element method (FEM), has become hugely important to the civil engineers of today. This has enabled them to effectively analyse design proposals and perform calculations too complicated to be done by hand. However, no generally accepted modeling approach exists to handle STC connections in these software. As a result, several different approaches exist to handle STC connections. This has to do with the complex nature of timber caused by its highly anisotropic properties (Pichler et al., 2018).

This thesis aims to advance the research on STC connections, by conducting a finite element analysis (FEA) of a bolted STC shear connection. The presented analysis has been done in the FEM-software Ansys Mechanical R2 2020. The connection in question was found in an experimental study conducted by R. Yang et al. (2020), and the results from that study will be compared to the analysis results in Ansys. A modelling approach called the "foundation material model" proposed by (Hong, 2007), will work as a basis for the model in this study. The connection involves the use of glulam made from Dahurian larch, a timber species found in the forests of the Far East including Northern China. As China consumes 60 % of the world's cement, efforts to introduce sustainable solutions into this market can have a significant impact (Lin et al., 2017). One obstacle timber construction has to overcome in the Chinese market, is the public scepticism concerning the safety of timber structures (Hu et al., 2016). For people living in areas where timber is more commonly seen in buildings, this scepticism might seem foreign. But for many parts of the world, this is a barrier preventing timber from being used. More research into the topic of timber construction can be a way to gradually convince more people that timber is a feasible alternative.

1.2 Previous work

Numerical studies on dowel-type connections based on the idea of a foundation surrounding the fasteners, have already been conducted. For instance by (Hong, 2007), (Hassanieh et al., 2017), (Leitner, 2011). But none of these use glulam made from Dahurian larch. The connection setups are also different for several of them, and various other fastener sizes were used.

Hassanieh et al. (2017) examined a STC shear connection similar to the one in this study. However, there are some differences. The main ones are that CLT made from a different timber species was used, together with significantly larger bolts. The study by Hassanieh et al. (2017) also aimed to capture the post-failure mode, which involved the use of a different material definition for the timber. This part of the analysis was beyond the scope of this thesis.

The thesis by Hong (2007) is an early example where a three-dimensional foundation material had been used to simulate bolted timber connections. Hong's work does not specifically focus on STC connections, but rather dowel-type timber connections as a whole. Several different analysis was conducted, including physical tests, that was later modelled in the software Ansys APDL. This allowed material properties for the timber to be determined, which could then be used in the numerical model. Leitner (2011) adopted the idea for a foundation material from Hong (2007). In Leitner's thesis, numerical modelling of timber moment connections was investigated along with experimental tests for finding material properties. This happened to be useful for this thesis as well, due to some unobtainable material properties for the timber. Both Hong (2007) and Leitner (2011) used Hill's yield criterion to define the timber material in their models, which was also adopted for this work.

The foundation material model approach produced promising results for all these three studies. Thus, this approach was selected for this research too.

1.3 Aim

One of the most important contributors to the development of the finite element method was Ray William Clough. Clough stated that physical experiments will always be necessary for the validation of computational models (R. W. Clough, 1990). This is also the fundamental idea behind the thesis.

This thesis aims to propose a FEM-simulation of a bolted STC shear connection, based on an experimental study conducted by R. Yang et al. (2020). This will be done with a modelling approach proposed by Hong (2007) called the foundation material model, to assess this approach's ability to accurately simulate the behaviour of the connection. The primary results from the experiment, that will be used for evaluation of the model, are the load-slip results.

1.4 Limitations

This work is limited to a numerical study of a STC connection that was tested by R. Yang et al. (2020). Experimental tests were not conducted. Due to the Covid-pandemic, which restricted access to test facilities at the university. The model created in the study therefore relies on available data from the literature. Efforts were made to make the model as close as possible to the experiment. Multiple connection cases were tested in the experimental study, but this work focused on a single case named "Group A" from R. Yang et al. (2020), where M6 bolts were used. The numerical data collected in the experiment was not available. Figures from the article was therefore used to compare against the model. This will have some effect on the accuracy.

There are many commercial FEM-software currently offered on the market. In this study Ansys Mechanical R2 2020 on an academic licence was used, since it was provided by the university. The hardware used was also provided by the university, but this is neither the latest or the most powerful hardware out there. Better equipment could potentially have enabled faster development of the model, and also allowed more demanding analyses to be performed.

Post-failure behaviour has not been considered for this work, as accurate simulation up to the point of failure was viewed as more useful for design applications. Engineers will always strive to avoid failure, thus accounting for what happens after failure has occurred was not prioritized.

2. Theory

2.1 Timber

Trees are often categorized into two primary groups, evergreens and deciduous. The main distinction between the two is that evergreens have foliage that remain green for more than one growing season, while deciduous trees shed their foliage every year. Most conifers are evergreens, but some share characteristics from both evergreens and deciduous trees. One of these exemptions is Larix gmelinii which in the summer have green needles, but change color in the fall and shed their needles during winter. Larix gmelinii is therefore categorised as a deciduous conifer. Despite losing its needles, the tree structure is still similar to other conifers. The tree structure is also something that distinguishes the conifers from deciduous trees, but as Larix gmelinii was used in the experiment this work is based on, conifers will be in focus.

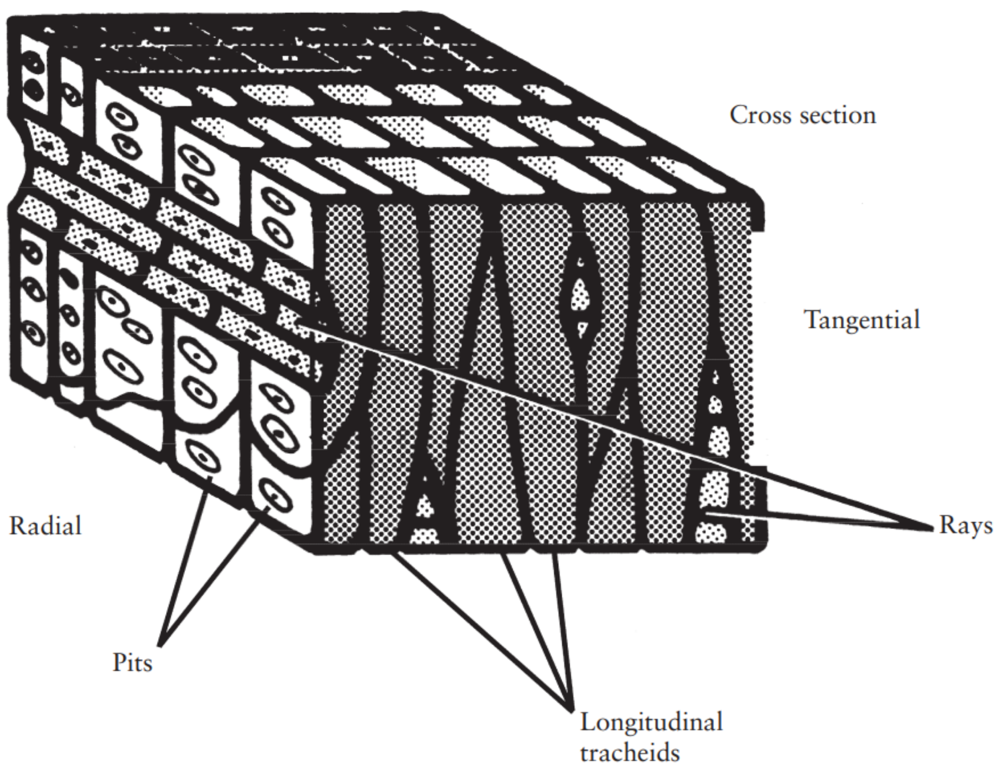

Fig. 2.1. Illustration of the microscopic structure in conifers (Shmulsky & Jones, 2011)

Wood is composed mainly of carbon, hydrogen and oxygen (Shmulsky & Jones, 2011). These make up three polymers, cellulose, hemicellulose and lignin, which together form the cell walls in the wood structure (Union, 2003). The most common cells in conifers are tracheids which are elongated cells that can be orientated in either the longitudinal or the radial direction of the tree (Richter, 2015). Most tracheids are longitudinal and their purpose is to provide strength to the tree as well as vertical transport of water and minerals (The Editors of Encyclopedia Britannica, 2016). The support from the longitudinal tracheids is required as external factors such as wind may cause tall trees to bend, which generates large stresses in the longitudinal direction. Because of this, timber is stronger in its longitudinal direction often referred to as "parallel to grain". Each tracheid can be as long as 6 mm for certain wood species, before they overlap into a new tracheid (Sperry et al., 2006).

The longitudinal tracheids are what make the characteristic annual growth rings that can be seen in the cross-section of timber. The rings are caused by seasonal dependent growth rate. During spring is when the tree undergoes the most rapid growth, which can account for 40-80% of the total growth in one year (Domec & Gartner, 2002). This portion of the annual ring is called earlywood. As it gets later in the season the earlywood transitions to latewood, the growth begins to slow down and the tracheids become smaller with thicker cell walls as can be seen in figure 2.2 (Wheeler, 2001). This causes higher density in the latewood which appears as a darker color in the annual ring. Diffusion of water between cells happens through something called "pits", and many of them can be found in the walls of the tracheids which allows for horizontal transport. Radial transport of nutrients happens through "rays" which consist of radial parenchyma and sometimes radial tracheids. Unlike tracheids, parenchyma are living cells that can alter their function depending on the need of the tree (The Editors of Encyclopedia Britannica, 2016).

Wood is one of the oldest building materials, with the earliest hard evidence of its use found in the archeological site Terra Amata, in Southern France. Here, archeolgists discovered traces of wooden huts made by hunters and gatherers some 300 000 years (de Lumley, 1969). Back then, primitive tools would have been used to harvest the trees and only simple alterations in the material would be made during construction. In the modern age however, several wood products have been developed for different purposes. Ordinary dimension timber sawn from logs is still commonly used, but techniques seeking to improve wood's durability and strength have allowed timber construction to advance into more complex and demanding applications. These products are known as engineered wood. The first product of this kind was plywood, which is made from "plies" or thin sheets of timber that are glued together in layers orientated 90° to each other (APA – The Engineered Wood Association, n.d). This produces stiff plates which benefit from the strength parallel to grain, in multiple directions. Another example of an engineered wood product which has had a significant impact on modern architecture is glulam.

2.2 Glulam

Glulam is an abbreviation for glued laminated timber and is one of the oldest engineered wood products (Moody & Hernandez, 1997). First invented in the 1890s and then later patented in Switzerland in 1901, glulam has since become a widely used construction material, especially in the Nordic countries where the demand is increasing (APA – The Engineered Wood Association, n.d; Gross, 2013). Glulam is composed of multiple layers of dimension lumber called lamellas which are stacked on top of each other and glued together. Prior to the introduction of glulam, timber constructions were limited by the natural height of the trees which determined the maximum length of the timber pieces. This is one of the main challenges that glulam solved.

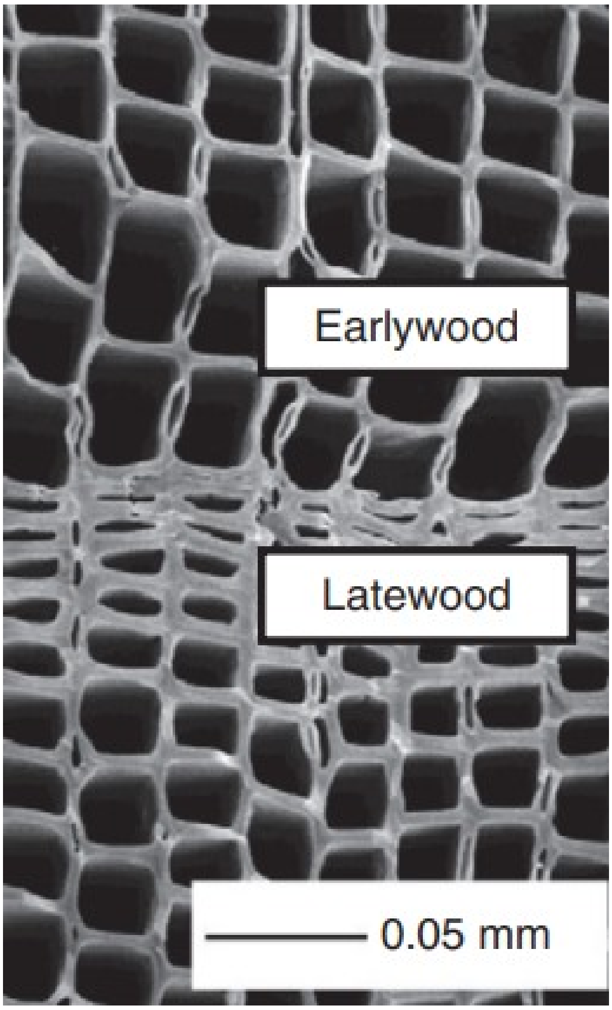

Fig. 2.2. Transistion from earlywood to latewood in conifers (Mleziva & Wang, 2012)

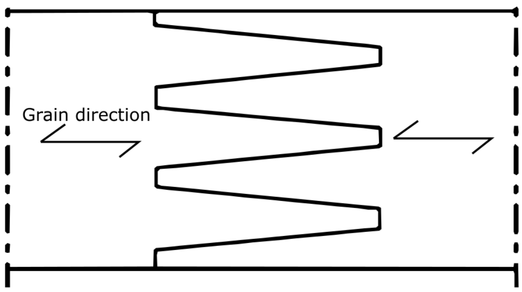

Fig. 2.3. Illustration of a finger joint

Extending timber sections requires a method to join separate wood pieces together. A way of doing this would simply be to apply adhesives to the ends and stick them together. However, this will not create a sufficient bond if the ends are just flat. This is because the bonds between end grains are poor, making the adhesive act as the sole contributor to the strength (Jokerst, 1981). A technique called finger joining addresses this issue. An illustration of a finger joint is shown in 2.3. The idea is to cut out profiles at the end of each section, which will interlock with each other. This promotes improved bonding between side grains instead of end grains, increased rigidity from mechanical interlocking, and also significantly increases the contact area where the adhesive can be applied

(Jokerst, 1981). An illustration of a finger joint joining two timber sections together is shown in figure 2.3. This technique allows longer timber sections to be made compared to traditional non-engineered timber. Another key benefit of glulam is the increased strength. The added height from several layers of timber evidently stiffens the glulam element, but another contribution comes from the "lamella-effect". Timber is prone to defects like knots and cracks which can cause localized strength reductions. But in glulam, these defects are distributed randomly as it is composed of several layers of different timber pieces. This reduces the risk of the defects from multiple lamellas getting concentrated near each other and is known as the lamella-effect (Moelven Limtre AS, n.d).

The manufacturing process of glulam starts with the delivery of dimension lumber from a sawmill that has been cut to the requested dimensions of the lamellas, and dried to an average moisture content of 12 +/-2 (%) (Leśko, 2021). The timber is assorted based on strength grades and the glulam manufacturer will have to decide which strength class it wants. Glulam consisting of lamellas with the same strength grade is called homogeneous glulam. Glulam can also be made with a variety of different strength grades and this is called combined glulam. For combined glulam beams it is common to place the strongest lamellas in the outermost layers where the stresses are the highest as shown in figure 2.4a (Serano et al., 2015). The timber pieces are then joined together with finger joints, before they are planned on the top and bottom to get an even gluing surface for the assembly of the layers. Glue is applied after, and the lamellas are arranged in the right order before entering a press what holds the glulam in place while the glue hardens. This is the stage where glulam elements can be bent into desired shapes, often used for roof supports or arch bridges. Wood is inherently hygroscopic, meaning that it can absorb water. Wood swells when it absorbs moisture and shrinks when it releases it (Pouzet et al., 2018). The dimension changes from this are not uniform and are dependent on the grain direction. To account for this phenomena in glulam, all the internal lamellas are orientated the same way, to minimize the internal stresses caused by shrinking or expansion of the timber. The outermost layers are always orientated with the core side facing outwards (Serano et al., 2015).

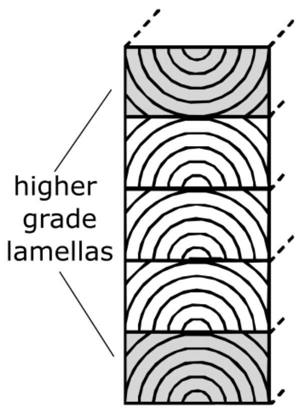

(a) Lamella configuration in glulam

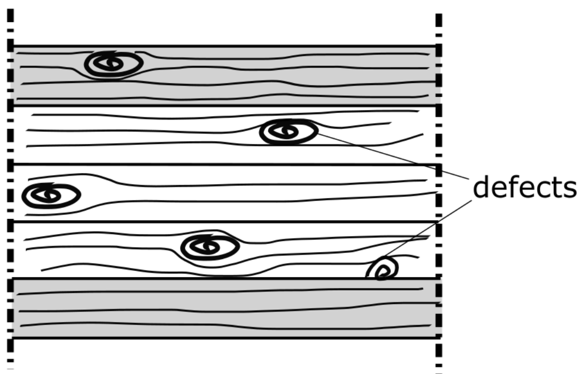

(b) Random distribution of defects, the "lamella effect"

Fig. 2.4. Glulam composition

2.3 Larix Gmelinii

Larix gmelinii, also known as Larix dahurica or Dahurian larch, is the northernmost growing tree species in the world (Bergstedt et al., 2007). Its habitat stretches itself across Eastern Russia, Mongolia, Northeast China and North Korea (Farjon, 2010). The forest regions east of the Ural mountains, are estimated to contain about 40 billion m^3 of trees in which Dahurian larch makes up about $\frac{1}{6}$ of the total volume (R. Gupta & Ethington, 1996). A significant percentage of China's larch forest is also made up of Dahurian larch, accounting for around 75% of the total larch forest volume (Zhou et al., 2002). Due to the number of trees, large habitat, excellent wood properties and affordable price, Dahruian larch is of great importance in both the Chinese and Russian market (Abaimov et al., 1998; Farjon, 2010; R. Yang et al., 2020). Several industries use Dahurian larch, and some of its applications include railway sleepers, construction material in buildings and the paper industry (Farjon, 2010).

2.4 Steel

Steel is one of the most important materials in the world today. The use of steel in some form or another can be found in nearly any industry, which makes it a vital part of the world's economy. So much so, that total monthly steel production in the world has been proposed as an indicator of the real global GDP and for forecasting commodity prices (Ravazzolo & Vespignani, 2017). Countless technological advancements have been achieved by exploiting steel's potential. The main reason behind steel's popularity is its versatility. With the help of heat, steel can be shaped to almost any size and form. Its ability to shift phases from solid to liquid as it gets melted, makes it possible to pour into casts which is practical for large quantity production, but also makes it possible to recycle. Its mechanical properties can also be altered in many different ways. A large variety of different steel grades exists with strength and stiffness properties engineered to suit different purposes.

Steel manufacturing is energy-intensive and two of the most common methods are Blast-Furnace Basic-Oxygen (BF-BOF) and Electric Arc Furnace (EAF) (Y. Yang et al., 2014). The EAF method is used for recycling scrap pieces of steel, by using the tremendous heat created by an electric arc to melt the scrap. The BF-BOF technique on the other hand uses less scrap but adds more of the raw material to make steel from scratch. Instead of using an electric arc, the heat is generated by blowing hot air at high velocities into a melting bucket containing iron ore, coke and lime (Y. Yang et al., 2014). The hot temperature is maintained by the coke burning from the hot air blast. Lime is added because it reacts with impurities and forms a substance called "slag" on top of the molten steel (Haynes, 2017). The slag makes it easier to remove the impurities as it can be skimmed off. During this stage, the steel composition is carefully monitored to ensure the right quality is produced.

All steels are alloys made with iron and carbon. But many methods exist to alter the properties of steel, like adding additional elements or various heat treatments. Steel is therefore categorized, often into four main groups; carbon steels, alloy steels, stainless steels and tool steels. They differ from each other based on the carbon content and the composition of other elements. Carbon steel is the most common steel type on the market, accounting for nearly 90% of the total steel production (Jones & Ashby, 2005). It mainly contains iron and carbon, but may contain small amounts of impurities by other elements. Carbon steels can be sorted into mild, medium and high carbon steel, depending on the amount of carbon. This can vary from as little as 0,05% up to 2%. Beyond that and the material is known as cast iron (Garrison, 2001). Like other metals and alloys, the atoms in the steel are arranged in periodically repeating arrays forming crystal structures (Clemens et al., 2017). This form of structure allows atoms to be tightly packed creating strong metallic bonds that provide strength, and also makes some alloys and metals perform excellently as conductors of heat and electricity.

The crystalline structure however is not fixed. Multiple structures exist which can drastically change the properties of the material. Many metals and alloys can even have several crystalline structures present at once, and experience transition phases depending on the temperature. This allows heat treatments to be used to alter the properties of metals and alloys. Among these crystalline structures are the Simple Cubic (SC), Face-Centered Cubic (FCC) and Body-Centered Cubic (BCC). They can be represented as cubes called "unit cells" which are the simplest repeating units for the global structure. The difference between them is how atoms are arranged and how much empty space there is in each cell.

An SC unit cell has $\frac{1}{8}^{\text{th}}$ of an atom in all eight corners or lattice points of the cube, one atom in total. BCC unit cells also have $\frac{1}{8}^{\text{th}}$ of an atom in each corner, but have one additional atom in the center of the cube. Therefore containing two atoms. In FCC unit cells, half an atom is present in the center of all six faces in addition to $\frac{1}{8}^{\text{th}}$ atoms in all corners. This makes the FCC structure the most populated structure of the three with four atoms. The effective volume that the atoms take up in each structure is 52%, 68%, 74% for SC, BCC and FCC respectively. This has an effect on the mechanical properties of the material, as the structure affects the ability of the atoms to move when subjected to stresses. These structures are not perfect. Sometimes extra atoms are present or atoms might be vacant which causes distortions in the crystalline structure. Imperfections like this will also affect the material properties just like knots and cracks will in timber. But due to the much smaller scale at which these imperfections occur compared to timber, the effect on the material properties is not as pronounced.

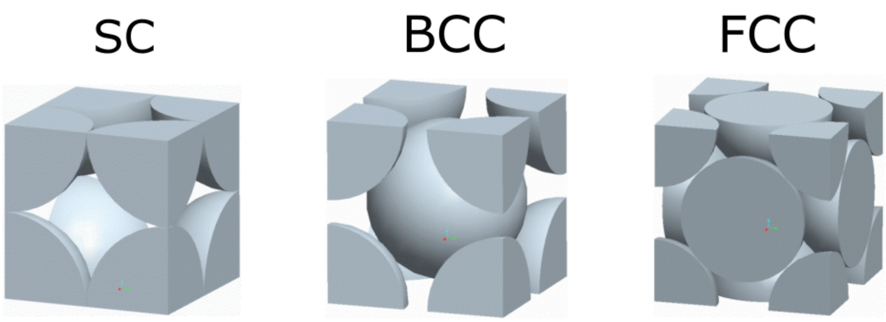

Fig. 2.5. Crystalline structures (J. Yang et al., 2019)

On a microscopic scale, the crystals work together to form grains. Grains are also important for the mechanical properties, and they can vary greatly in shape and size (Morris, 2001). When the material is put under stress, the grains will get warped and slide against each other (H. Yang et al., 2021). The properties of the grains are therefore a factor when it comes to the ductility and strength of the material. In steel, higher carbon content causes a change in the grain structure. Pure iron, also known as "ferrite", is ductile but not strong. But when carbon is present it reacts with the iron to produce cementite, which is much harder and stronger than ferrite (Gonzaga, 2013). If carbon steel is put under a microscope, the grain structure shows grains of ferrite, but also grains composed of ferrite and cementite. In these grains, cementite and iron form a laminate structure called pearlite which benefits from both the ductility provied by the iron, and the increased strength from cementite (Embury, 2012; Gonzaga, 2013). By increasing the amount of carbon, the steel becomes even stronger at the cost of ductility.

One of the main disadvantages of carbon steel is that it is prone to corrosion. Corrosion occurs when oxygen reacts with iron. This produces ferric oxide, more commonly referred to as "rust" (Featherstone, 2015). Oxidization of iron begins as soon as it comes in contact with oxygen. This

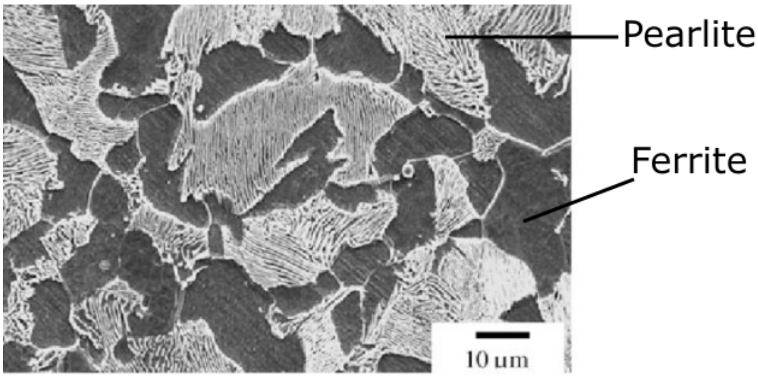

Fig. 2.6. Grain structure in carbon steel (Zrnik et al., 2010)

process is slow in low humidity and temperatures, but heating the steel up or subjecting it to water speeds this process up, making rust a concern for steel structures in wet environments (Pint et al., 2012). Rust is damaging to the steel as it is porous, providing no strength and will continue to spread in the steel until it is completely corroded (Bensabra & Azzouz, 2013). This issue is costly and potentially dangerous, as it can significantly compromise structures and cause them to fail. Corrosion is a problem that some of the other types of steel address by adding various elements into the mix. Stainless steel for example holds a large amount of chromium. The chromium oxidizes easier than iron, and in the process, it creates a protective film on the surface of the steel which prevents further corrosion. It seems logical then to just use stainless steel and not having to worry about corrosion, but there are trade-offs with every steel type. In the case of stainless steel, it tends to be more expensive due to more elements required to produce it and its poor workability. Another disadvantage is that it is less suitable for welding. Because of the large variety of steel types on the market, engineers have to pick the type that is able to perform in a safe and satisfactory way, but also within budget.

2.5 Hooke's law

Hooke's law was derived by the English scientist Robert Hooke back in 1660 (Rao, 2011). By observing the displacement in vertically suspended springs with masses attached at the ends, he realized that there was a proportional relationship between the mass of the objects and the distance the springs were stretched (Keaton, 2018).

$$F = -k\Delta x \tag{2.1}$$

Where:

$$F = \text{force [N]}$$
$$k = \text{stiffness } [\frac{N}{m}]$$
$$\Delta x = \text{displacement [m]}$$

The negative sign comes from the fact that the force calculated is the force generated by the spring. This force will always point in the opposite direction to where it is displaced. Springs are the classical example used when explaining Hooke's law, as the displacement is clearly observable and most people have encountered them at some point in their life. They have a spring coefficient (K) with the unit $\frac{kN}{m}$, which can also be referred to as the stiffness. K describes how much force is required to displace the spring, with the force getting increasingly larger the more displaced the spring gets. Anyone who has tried stretching a spring will have experienced this phenomenon. But Hooke also realised that many other solid materials exert the same behavior as springs when subjected to forces and stresses, even though it is not as easily observable. Any material that shows deformations proportional to some range of forces or stresses, follows this law. K depends on the material but also on the size and shape of the object. Another way Hooke's law can be written is in terms of stress and strain. This way only the material properties matter. The normal stress-strain relationship can be derived as follows;

$$\Delta x = x - x_0 \tag{2.2}$$

Where:

$$\begin{aligned} \Delta x &= \text{displacement [m]} \\ x &= \text{deformed length [m]} \\ x_0 &= \text{nominal length [m]} \end{aligned}$$

$$\Delta x = \frac{1}{E}\frac{F}{A}x_0 \quad \rightarrow \quad \frac{F}{A} = E\frac{\Delta x}{x_0} \tag{2.3}$$

Where:

$$\begin{aligned} F &= \text{force [N]} \\ A &= \text{area of cross-section } [m^2] \\ E &= \text{modulus of elasticity [Pa]} \\ \Delta x &= \text{displacement [m]} \\ x &= \text{deformed length [m]} \\ x_0 &= \text{nominal length [m]} \end{aligned}$$

This can be written as Hooke's law for normal stress and normal strain in a single dimension (Atanackovic & Guran, 2000);

$$\sigma = E\varepsilon \tag{2.4}$$

Where:

$$\begin{aligned} \sigma &= \text{normal stress [Pa]} \\ E &= \text{modulus of elasticity [Pa]} \\ \varepsilon &= \text{nominal strain} \end{aligned}$$

ε is unitless and measures how much an object is deformed relative to its nominal size. This tells us that there is a linear relationship between stress and strain. Thus it only applies when a material behaves linear elastic, which will be explained further in section 2.6. Hooke's law can also be expressed in terms of shear stress and shear strain (B. Yang, 2005);

$$\tau_{xy} = G\gamma_{xy} \tag{2.5}$$

Where:

$$\begin{aligned}\tau_{xy} &= \text{shear stress in the xy-plane [Pa]}\\ G &= \text{shear modulus [Pa]}\\ \gamma_{xy} &= \text{shear strain in the xy-plane}\end{aligned}$$

There is a relationship between the shear modulus, Poisson's ratio and modulus of elasticity, which allows the shear modulus to be calculated with Huber's formula. Huber's equation for the shear modulus is given by (B. Yang, 2005);

$$G = \frac{E}{2(1+v)} \tag{2.6}$$

Where:

$$\begin{aligned}E &= \text{modulus of elasticity [Pa]}\\ v &= \text{Poisson's ratio}\end{aligned}$$

Poisson's ratio is a linear relationship between longitudinal strain and lateral strain.

$$v = -\frac{\varepsilon_{lat}}{\varepsilon_{long}} \tag{2.7}$$

Where:

$$\begin{aligned}\varepsilon_{lat} &= \text{lateral strain}\\ \varepsilon_{long} &= \text{longitudinal strain}\end{aligned}$$

Hooke's law can be generalized for cases where normal stresses are applied in multiple directions. For such a case the total strain of the object can be calculated by adding the strain contribution from the individual strains. The generalized Hooke's law can be expressed as follows (B. Yang, 2005);

$$\begin{aligned}\varepsilon_x &= \frac{1}{E}[\sigma_x - v(\sigma_y + \sigma_z)]\\ \varepsilon_y &= \frac{1}{E}[\sigma_y - v(\sigma_x + \sigma_z)]\\ \varepsilon_z &= \frac{1}{E}[\sigma_z - v(\sigma_x + \sigma_y)]\end{aligned} \tag{2.8}$$

Shear strains in one plane will not cause shear strains in another, a generalized Hooke's law for shear strains, therefore, does not exist.

2.6 Elasticity

Elasticity is the non-permanent deformation of materials caused by stress. This means that if the stress is removed, the material should return to its original shape. There is a linear relationship between stress and strain in this region, and therefore Hooke's law is valid. The slope of the elastic curve is the modulus of elasticity (Vaidya & Pathak, 2019). The material reaches the end of the elastic region when the stress-strain relationship seizes to be linear. At this point, plastic deformation starts to occur, which is permanent. Soon after the material starts to deform plastically, it reaches its yield point. Some materials experience a reduction in stress right after the upper yield point, before the stress starts to increase again. This is seen in figure 2.7. This point is called the lower yield point. However, some materials do not have a distinct upper and lower yield point, or even a distinctive yield point at all. For such materials, using an offset yield point can be more practical. Aluminium for instance does not have a clear yield point, therefore a line parallel to the MOE is drawn from a point on the strain axis, often the 0.1% or 0.2% strain, until it intersects the stress-strain curve. That point is then defined as the yield strength (Gedeon, 2012). The ultimate strength is the highest point on the curve. In tensile tests, the ultimate strength is followed by a region where stress decreases until it fractures and breaks. This decrease of stress happens because of plastic instability, which causes a local reduction in cross-section called necking (Tu et al., 2020).

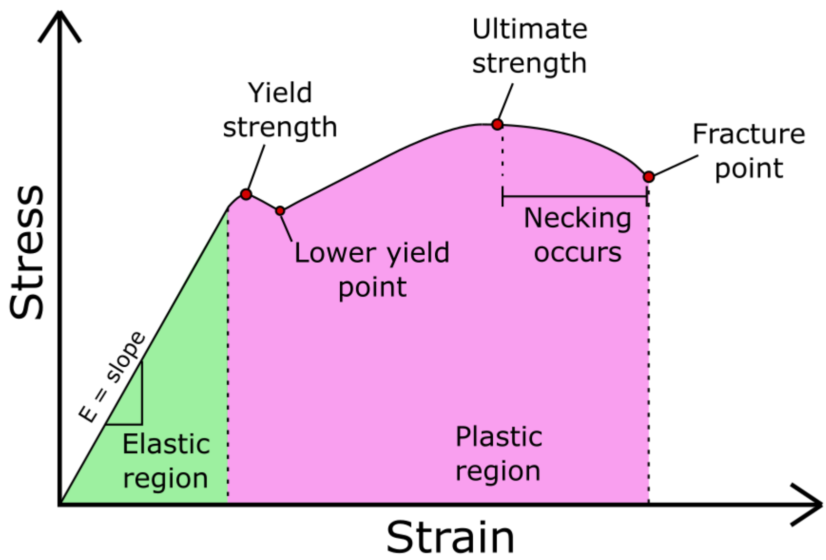

Fig. 2.7. Stress-strain diagram

Necking is often associated with ductile materials, but brittle materials can also experience some degree of necking. Because fracture occurs soon after the ultimate stress, necking in brittle materials can be difficult to observe. Due to the nature of the testing equipment, the load that is applied decreases slightly in this phase, but deformation still continues. There are two ways of expressing the stress-strain curve. Engineering stress-strain and true stress-strain. For engineering stress, the nominal cross-section area is used for calculating the stress during the test. True stress accounts for the reduced area due to deformations. The reduction of the cross-section will cause the localized stress to increase during the necking phase. Because it is challenging to monitor the reduction of cross-section area throughout the test, engineering stress is often used when conducting tensile tests.

Ductile materials can undergo more plastic deformation than brittle materials. Figure 2.9 illus-

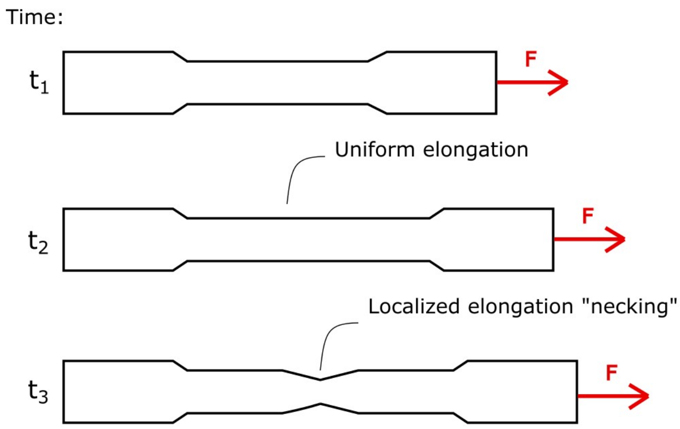

Fig. 2.8. Necking in a tensile test sample

trates this by showing a potential stress-strain curve for a ductile and a brittle material.

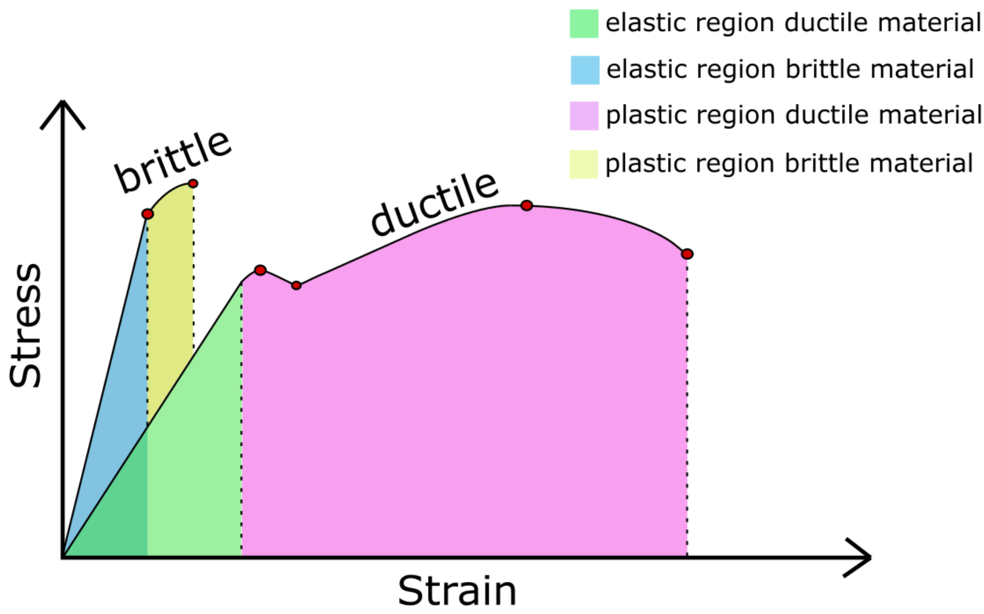

Fig. 2.9. Stress-strain curves for ductile and brittle materials

2.6.1 Anisotropic Elasticity

Anisotropic materials are materials that have no plane of symmetry where the mechanical properties are the same. General anisotropy is the simplest form and requires 21 elastic tensor components (Sedlák et al., 2014). However, no successful attempt has been made to fully determine all 21 constants for truly general anisotropic materials (Sedlák et al., 2014). The stress and strain tensors are written as follows (Vannucci, 2018):

$$\{\sigma\} = \begin{Bmatrix} \sigma_1 = \sigma_{xx} \\ \sigma_2 = \sigma_{yy} \\ \sigma_3 = \sigma_{zz} \\ \sigma_4 = \sigma_{yz} \\ \sigma_5 = \sigma_{xz} \\ \sigma_6 = \sigma_{xy} \end{Bmatrix}, \quad \{\varepsilon\} = \begin{Bmatrix} \varepsilon_1 = \varepsilon_{xx} \\ \varepsilon_2 = \varepsilon_{yy} \\ \varepsilon_3 = \varepsilon_{zz} \\ \varepsilon_4 = \varepsilon_{yz} \\ \varepsilon_5 = \varepsilon_{xz} \\ \varepsilon_6 = \varepsilon_{xy} \end{Bmatrix} \tag{2.9}$$

The generalised Hooke's law for a linear elastic material (Kelly, 2013);

$$\{\sigma\} = [C]\,[\varepsilon] \rightarrow \begin{Bmatrix} \sigma_1 \\ \sigma_2 \\ \sigma_3 \\ \sigma_4 \\ \sigma_5 \\ \sigma_6 \end{Bmatrix} = \begin{bmatrix} C_{11} & C_{12} & C_{13} & C_{14} & C_{15} & C_{16} \\ C_{21} & C_{22} & C_{23} & C_{24} & C_{25} & C_{26} \\ C_{31} & C_{32} & C_{33} & C_{34} & C_{35} & C_{36} \\ C_{41} & C_{42} & C_{43} & C_{44} & C_{45} & C_{46} \\ C_{51} & C_{52} & C_{53} & C_{54} & C_{55} & C_{56} \\ C_{61} & C_{62} & C_{63} & C_{64} & C_{65} & C_{66} \end{bmatrix} \begin{Bmatrix} \varepsilon_1 \\ \varepsilon_2 \\ \varepsilon_3 \\ \varepsilon_4 \\ \varepsilon_5 \\ \varepsilon_6 \end{Bmatrix} \tag{2.10}$$

C is the stiffness matrix. This can also be inverted so the strain is on the left side of the equal symbol. This is done using $C^{-1} = S$. S is known as the compliance matrix.

$$\{\varepsilon\} = [S]\,[\sigma] \rightarrow \begin{Bmatrix} \varepsilon_1 \\ \varepsilon_2 \\ \varepsilon_3 \\ \varepsilon_4 \\ \varepsilon_5 \\ \varepsilon_6 \end{Bmatrix} = \begin{bmatrix} S_{11} & S_{12} & S_{13} & S_{14} & S_{15} & S_{16} \\ S_{21} & S_{22} & S_{23} & S_{24} & S_{25} & S_{26} \\ S_{31} & S_{32} & S_{33} & S_{34} & S_{35} & S_{36} \\ S_{41} & S_{42} & S_{43} & S_{44} & S_{45} & S_{46} \\ S_{51} & S_{52} & S_{53} & S_{54} & S_{55} & S_{56} \\ S_{61} & S_{62} & S_{63} & S_{64} & S_{65} & S_{66} \end{bmatrix} \begin{Bmatrix} \sigma_1 \\ \sigma_2 \\ \sigma_3 \\ \sigma_4 \\ \sigma_5 \\ \sigma_6 \end{Bmatrix} \tag{2.11}$$

2.6.2 Orthotropic Elasticity

Orthotropic elastic materials have three orthogonal planes of symmetry. The compliance matrix of anisotropic elasticity can thus be reduced to having 9 independent constants as opposed to 21 (Wickeler & Naguib, 2020).

$$\begin{Bmatrix} \varepsilon_1 \\ \varepsilon_2 \\ \varepsilon_3 \\ \varepsilon_4 \\ \varepsilon_5 \\ \varepsilon_6 \end{Bmatrix} = \begin{bmatrix} \frac{1}{E_x} & \frac{-\upsilon_{yx}}{E_y} & \frac{-\upsilon_{zx}}{E_z} & 0 & 0 & 0 \\ \frac{-\upsilon_{xy}}{E_x} & \frac{1}{E_y} & \frac{-\upsilon_{zy}}{E_z} & 0 & 0 & 0 \\ \frac{-\upsilon_{xz}}{E_x} & \frac{-\upsilon_{yx}}{E_y} & \frac{1}{E_z} & 0 & 0 & 0 \\ 0 & 0 & 0 & \frac{1}{2G_{yz}} & 0 & 0 \\ 0 & 0 & 0 & 0 & \frac{1}{2G_{zx}} & 0 \\ 0 & 0 & 0 & 0 & 0 & \frac{1}{2G_{xy}} \end{bmatrix} \begin{Bmatrix} \sigma_1 \\ \sigma_2 \\ \sigma_3 \\ \sigma_4 \\ \sigma_5 \\ \sigma_6 \end{Bmatrix} \tag{2.12}$$

Note that the matrix contains three independent elasticity moduli, shear moduli and Poisson's ratios. The remaining Poisson's ratios can be determined using the relationship;

$$\frac{v_{yz}}{E_y} = \frac{v_{zy}}{E_z}, \frac{v_{zx}}{E_z} = \frac{v_{xz}}{E_x}, \frac{v_{xy}}{E_x} = \frac{v_{yx}}{E_y} \tag{2.13}$$

2.6.3 Isotropic Elasticity

Isotropic elastic materials are considered to have direction-independent mechanical properties. This reduces the number of independent elastic constants to two (Kelly, 2013).

$$\begin{Bmatrix} \varepsilon_1 \\ \varepsilon_2 \\ \varepsilon_3 \\ \varepsilon_4 \\ \varepsilon_5 \\ \varepsilon_6 \end{Bmatrix} = \begin{bmatrix} \frac{1}{E} & \frac{-v}{E} & \frac{-v}{E} & 0 & 0 & 0 \\ \frac{-v}{E} & \frac{1}{E} & \frac{-v}{E} & 0 & 0 & 0 \\ \frac{-v}{E} & \frac{-v}{E} & \frac{1}{E} & 0 & 0 & 0 \\ 0 & 0 & 0 & \frac{1}{2G} & 0 & 0 \\ 0 & 0 & 0 & 0 & \frac{1}{2G} & 0 \\ 0 & 0 & 0 & 0 & 0 & \frac{1}{2G} \end{bmatrix} \begin{Bmatrix} \sigma_1 \\ \sigma_2 \\ \sigma_3 \\ \sigma_4 \\ \sigma_5 \\ \sigma_6 \end{Bmatrix} \tag{2.14}$$

2.7 Elasticity in Wood

All the different variables that come into play to make up the wood structure such as, cell types, cell orientation, cell size, cell shape, density and moisture variations make timber an anisotropic material. Lignin is for example isotropic, hemicellulose and cellulose are transversely isotropic, which means it has one plane of symmetry (Katz et al., 2008). Therefore no plane of symmetry exists for wood, thus implying that wood is highly direction dependant. This makes the behaviour of timber difficult to predict with mathematical formulations, with a large number of parameters required to be defined. Because of this timber is often simplified to reduce the number of constants needed to describe it. Through strength tests in the different directions of the timber, three distinct directions stand out where the properties between them differ the most. These are the longitudinal, radial and tangential directions. The longitudinal direction is in the same direction as the height of the tree, often referred to as parallel to grain. The radial direction is orthogonal to the growth rings, while the tangential direction is the tangent of the growth rings. This means that wood can be assumed to be an orthotropic material.

Two methods of sawing timber are shown below in figure 2.11, but several others exist. The difference between them is the size of the pieces and the grain pattern. Plain sawn timber is effective as it utilizes nearly all of the overall timber volume, but many of the pieces will have an unfavorable grain pattern. This is because wood shrinks and expands at different rates in the longitudinal, radial and tangential direction, when moisture content varies. Not much change happens longitudinally. However, wood shrinks and swells the most tangentially, and typically half as much radially Eckelman and Service (2000). The top and bottom-most sections in figure 2.11a have a curved grain pattern which increases the risk of the section being bent from tangential shrinking. The other sawing method is called quarter-sawing, which is used to get more sections with favorable grain patterns. Grains that run straight across the sections will have less of a tendency to bend the pieces. A downside to quarter sawing is that more waste is produced and it is more labour-

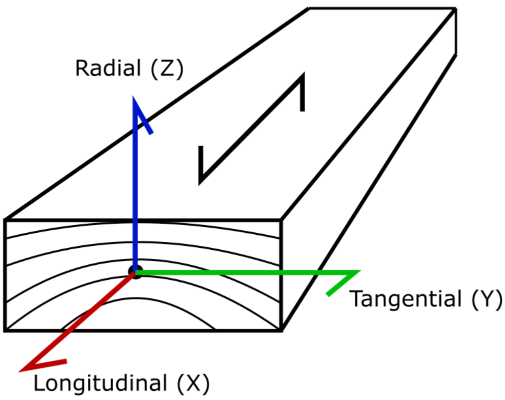

Fig. 2.10. Orthotropic directions in wood

intensive to perform. Plain sawn is a cheaper alternative than quarter-sawn, but is considered to have lower quality.

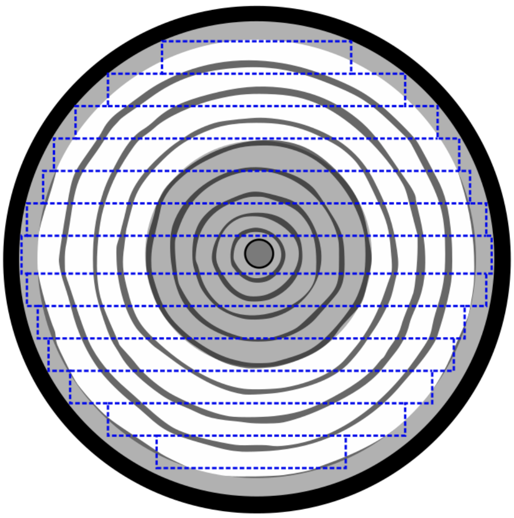

(a) Plain sawn timber

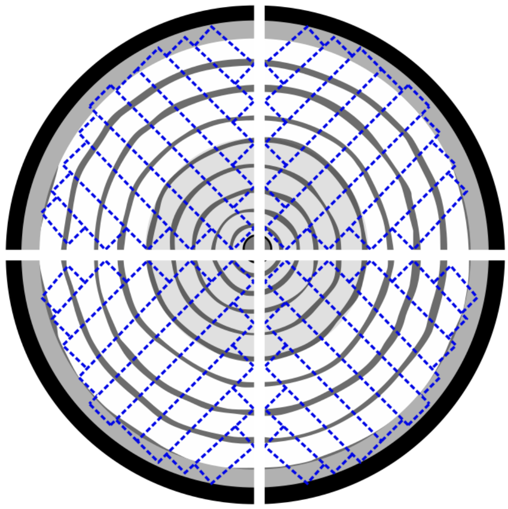

(b) Quarter sawn timber

Fig. 2.11. Sawing methods for timber

Because the grain pattern in sawn lumber varies depending on the way the lumber has been cut, the tangential and radial direction is not fixed. Knowing exactly how wood has been cut from a supplier is impossible for an engineer to predict during the design process. Therefore another simplification is often added which reduces the radial and tangential to just one common direction. This direction is perpendicular to the grain. For experiments however, the grain patterns in the test specimens are easier to identify, thus orthotropic elasticity can be considered. No emphasis was put on the grain pattern of the glulam in the experiment by R. Yang et al. (2020), but judging by the photos the glulam lamellas look like they have been plain sawn. See figure 2.12.

Fig. 2.12. One of the glulam specimens used in the experiment (R. Yang et al., 2020)

2.8 Elasticity in Steel

In contrast to wood, the structure of steel is less complex with fewer irregularities that can affect its mechanical properties. Steel is considered an isotropic material with identical material properties in all directions. Even though crystalline structures are not perfect, the imperfections happen on an atomic scale as opposed to wood where imperfections like knots and grains can even be seen with the naked eye. However, some treatments of steel like cold working, may cause directionality to the material properties by elongating the grains in the microstructure (Voort, 2014). But generally, steel is viewed as isotropic.

2.9 Plasticity

2.9.1 von Mises yield criterion

The von Mises yield criterion is one of the most commonly used yield criteria in engineering. It was developed for ductile isotropic metals in complex stress states, that initially deform elastically but transition to plastic deformation. The idea is to use the contribution from different stresses to determine if the material has yielded. If the von mises stress σ_{vm} exceeds the yield strength, then yield has been reached.

$$\sigma_{VM} = \sqrt{\frac{(\sigma_{xx}-\sigma_{yy})^2 + (\sigma_{yy}-\sigma_{zz})^2 + (\sigma_{zz}-\sigma_{xx})^2 + 6(\sigma_{xy}^2+\sigma_{yz}^2+\sigma_{zx}^2)}{2}} \tag{2.15}$$

Where $\sigma_{xx}, \sigma_{yy}, \sigma_{zz}$ are the principal stresses and $\sigma_{xy}, \sigma_{yz}, \sigma_{zx}$ are the shear stresses acting in the material.

2.9.2 Hill's yield criterion

Hill's yield criterion builds on the von Mises yield criterion, but aims to predict initiation of plastic deformation in anisotropic materials. It uses three planes of symmetry for the material properties, which simplifies the anisotropic material as an orthotropic. Hill's yield criterion can be written as (Zadpoor et al., 2011);

$$F(\sigma_{yy}-\sigma_{zz})^2+G(\sigma_{zz}-\sigma_{xx})^2+H(\sigma_{xx}-\sigma_{yy})^2+2L\sigma_{yz}^2+2M\sigma_{zx}^2+2N\sigma_{xy}^2=1 \tag{2.16}$$

Where the σ's are the three principle stresses in the x-,y-,z-direction and the three shear stresses. F, G, H, L, M, N are material constants. The material constants can be calculated like this (Arvidsson, 2018);

$$F=\frac{1}{2}(\frac{1}{R_{yy}^2}+\frac{1}{R_{xx}^2}+\frac{1}{R_{xx}^2}) \tag{2.17}$$

$$G=\frac{1}{2}(\frac{1}{R_{zz}^2}+\frac{1}{R_{xx}^2}+\frac{1}{R_{yy}^2}) \tag{2.18}$$

$$H=\frac{1}{2}(\frac{1}{R_{xx}^2}+\frac{1}{R_{yy}^2}+\frac{1}{R_{zz}^2}) \tag{2.19}$$

$$L=\frac{3}{2}(\frac{1}{R_{yz}^2}) \tag{2.20}$$

$$M=\frac{3}{2}(\frac{1}{R_{xz}^2}) \tag{2.21}$$

$$N=\frac{3}{2}(\frac{1}{R_{xy}^2}) \tag{2.22}$$

The stress ratios are determined using the yield strengths in normal stress and shear for the material, and are calculated as follows (dos Santos et al., 2015):

$$R_{xx}=\frac{\sigma_{xx}^y}{\sigma_y} \tag{2.23}$$

$$R_{yy}=\frac{\sigma_{yy}^y}{\sigma_y} \tag{2.24}$$

$$R_{zz}=\frac{\sigma_{zz}^y}{\sigma_y} \tag{2.25}$$

$$R_{xy}=\sqrt{3}\frac{\tau_{xy}^y}{\sigma_y} \tag{2.26}$$

$$R_{yz} = \sqrt{3}\frac{\tau_{yz}^{y}}{\sigma_y} \tag{2.27}$$

$$R_{xz} = \sqrt{3}\frac{\tau_{xz}^{y}}{\sigma_y} \tag{2.28}$$

Where σ_y is a reference stress (Colby, 2013).

3. Methodology

3.1 Finite element method

The origin of the term "finite element method" (FEM) can be traced back to the 1960 book "The Finite Element Method in Plane Stress Analysis" by R. Clough (1960), but contributions to the development of this method started back in the early 1940s. It is unclear exactly who the first person was to introduce the FEM, and several efforts have been made to put this discussion to rest, for instance by K. K. Gupta and Meek (1996), R. W. Clough (1990) and Stein (2014). They all acknowledge the work by Courant (1943), but K. K. Gupta and Meek (1996) were hesitant to give Courant the credit as a founder of FEM because of the lack of calculations provided in his paper. R. W. Clough (1990) argues however, that Courant had proposed the concept of regional discretization which is a key part of the finite element method. But due to the lack of computers at the time, the usefulness of Courant's proposal was not acknowledged until long after the FEM had become an accepted tool. Stein (2014) concludes that the first modern application of 2D FEM was developed by Turner et al. (1956) who were members of the Structural Dynamics Unit at the Boeing Airplane Company. Demand for more lightweight construction of aircraft grew, as airplane configurations became more complex. This led the unit to be assigned the task of developing lighter aircraft wings. Few companies could afford powerful computers at the time, but the large aircraft manufacturers were one of the exceptions, which enabled them to develop the FEM. No immediate adaptation of FEM was seen in other industries, until it was introduced to civil engineering a few years later with the publication of (R. Clough et al., 1962).

The FEM has since become widely used across several fields of engineering, mainly due to its effectiveness and general applicability (Bathe, 2006). Aeronautics engineers of the 1950s recognised the practicality of using matrix notation for formulating equations, as this notation was well suited as inputs for computers. This turned out to be an essential discovery in the development of FEM, as awareness for the potential of computer-aided engineering grew (R. W. Clough, 1990). Computational power is a factor that has always impeded the use of FEM, preventing the most complex problems to be solved and forced simplifications to be made to cut down on computational cost. But as advancements in technology continue to move forward, these limitations become less apparent, enabling increasingly demanding tasks to be completed in less time. As demand for FEM has grown, numerous software have entered the market, often with a premium price attached. For this work however, Ansys R2 2020 was chosen as it can be accessed for free through a student licence. Nevertheless, Ansys is a professional tool with powerful analysis capabilities which were viewed as necessary for this research.

The purpose of the finite element method is to simulate the behavior of complex physical problems by solving partial differential equations (PDEs) numerically. The fundamental idea is to divide a larger problem (a domain) which is difficult or even impossible to solve analytically, into smaller simpler parts (subdomains) (Thompson & Thompson, 2017). These subdomains are what are known as finite elements (FEs). First thought of as a method for designing lightweight airplane wings, it turned out to be a versatile method across multiple engineering fields. According to Miller and Mattuck (2010) "Differential Equations are the language in which the laws of nature are expressed", which suggests that the FEM can be applicable to any natural phenomena. Some of the most common uses of the FEM include structural analysis, fluid mechanics, heat transfer and multiphysics systems (Bi, 2017). Many FEM-software including Ansys have capabilities to compute several types of FEAs, so it is up to the users to specify what type of analysis they want to conduct. After selecting an analysis, the software interface gets restricted to include only relevant options for that specific type of analysis. This makes the software user-friendly and minimizes the information that the program must handle.

The process of transforming a continuous problem into a finite number of elements is called discretization, which in FEM terminology is known as meshing. The reason for dividing a domain into a finite number of subdomains, is to limit the number of variables that can affect the problem. This is a way of "idealising" a problem to make it easier to solve, by removing factors considered nonessential for solving the problem. Idealization is a technique invented by Galileo Galilei, which he used to argue the concept of "free-fall" where air resistance of falling objects is ignored (Song et al., 2002). The meshing process is where the type and number of elements are decided. Many element types exist, and they all have different capabilities that must be taken into consideration when performing a finite element analysis (FEA). Each element has a certain shape, size and what is known as degrees of freedom (DOF). Some examples of DOFs are ways in which an object can move or other more abstract variables such as heat transfer or electromagnetic properties. The DOFs are defined at nodes, which are coordinate points located on the FEs. Calculations on each FE are conducted at integration points that are found within the elements. Extrapolation or interpolation are then performed on the solutions from the integration points, to obtain the results for the rest of the element.

Many different element types exist, all with a unique set of characteristics. Elements can be as simple as just a point, which is represented as a single node that can be used for example to define a mass element, or they can be complicated solids with a high number of nodes. The selection of the right element type for a problem is important, because the element must be able to accurately depict the behaviour of the problem, while keeping the computational cost as low as possible. The more complex an element gets, the longer it takes to solve. This leads back to degrees of freedom. Elements cannot provide results for certain calculations if they do not have the required DOF's to do so. It is therefore crucial to be cautious when picking the element types for a FEA. An example of a commonly used element type for structural analysis is line elements. Line elements are simple as they only require at least two nodes, one for each end of the element. They are often used for modelling truss elements, beams or columns in structural analysis. FEM-software usually have a large library with different element types that can be selected, often with encrypting names like the line element BEAM161 from the Ansys library. Note that more complex geometric elements such as solids, do not necessarily have more DOFs than simpler geometries like lines. The BEAM161 for example has three nodes and eleven DOFs, while the SOLID186 has twenty nodes and only three DOFs (ANSYS, Inc, 2011).

Executing a finite element analysis requires some general steps. According to (Bathe, 2006) the first step is to choose the correct mathematical model for the given physical problem. Some of the fundamental processes in this step are defining the geometry, materials, boundary conditions and loading. It is essential to understand that the finite element solution will only consider the

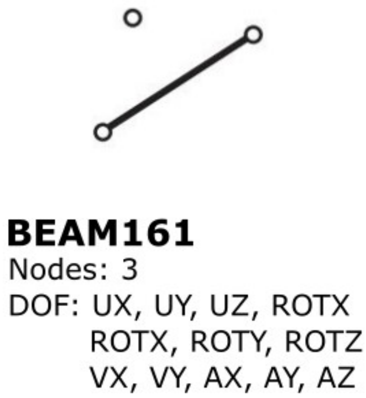

(a) BEAM161

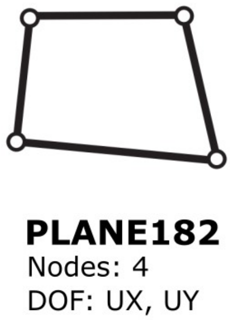

(b) PLANE182

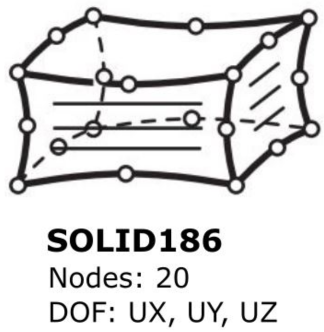

(c) SOLID186

Fig. 3.1. Examples of element types from (ANSYS, Inc, 2011)

input given by the user, 'We cannot expect any more information in the prediction of physical phenomena than the information contained in the mathematical model' (Bathe, 2006, p. 2). After selecting the element types, mesh and solution parameters, the problem is then ready to be solved. The next step is assessing the accuracy of the finite element solution. If the results aren't accurate enough then refinements need to be done before rerunning the solution step. When the results are perceived as accurate, the last step is to interpret the results and perhaps work out optimizations to the structural problem. An overview of the FEA process is shown in figure 3.2

The FEM has proved to be one of the most important tools in modern engineering (Plevris & Tsiatas, 2018). This is certainly the case for structural engineering, which has continuously evolved into making larger, taller and more groundbreaking structures. A large portion of the credit for these achievements has to be given to the development of FEM-software, which has enabled better insight and improved the decision-making during the design process. We can now build safer and with more efficient use of materials. Despite all this however, it is still important to remember that the FEM is just a tool made to aid engineers. R. W. Clough (1980) explicitly states that computational models can not replace physical experiments. Validation of a FEM-model can only be achieved if it can be compared to knowledge gained from actual tests. The FEM will in all likelihood continue to grow in popularity, but it is important to understand the theory behind it and be critical to its results. To better explain how the finite element method is applied to practical problems, two examples will be presented and solved in section 3.1.1 and 3.1.2.

Each example will focus on a method from a specific formulation of the finite element method. Since FEM can be used for numerous engineering fields, these examples are limited to its appli-

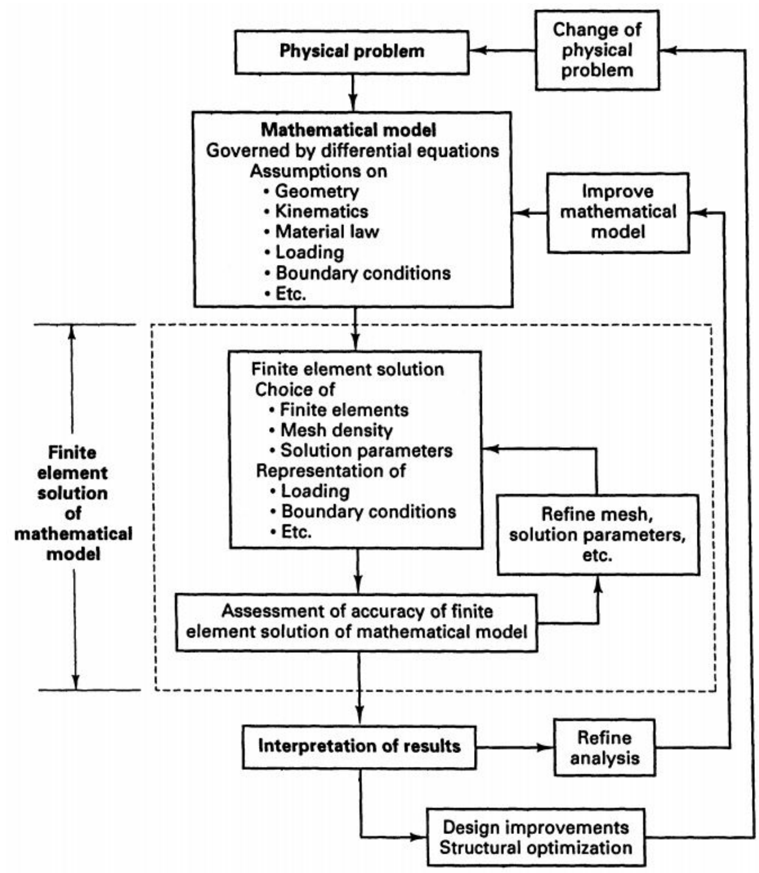

Fig. 3.2. The process of finite element analysis (Bathe, 2006)

cation in structural engineering as this is the relevant topic for this work. The two formulations which will be used for solving the examples are the "direct approach" and "weighted residuals approach". These differ in that the direct approach is used for solving structural problems that can be expressed through Hooke's law, by solving the governing equations directly for the elements in the model, while the weighted residuals approach utilizes trial equations to approximate a solution to a problem that can be expressed as a differential equation. Each formulation contains several methods, but the most common ones will be highlighted here. From the direct approach, the direct stiffness method will be used for the first example. For the other example, Galerkin's method which is the most widely used methods of the weighted residuals, will be used (Zohdi, 2018).

3.1.1 Application of FEM: direct stiffness method

The direct stiffness method uses the relationship between force, stiffness and displacement. This is one of the most common applications of the FEM, and is used extensively in structural analysis. For linear analysis Hooke's law can be applied as $\{F\} = [-K]\{u\}$. The stiffness of each element can be defined by the shape, size and the material properties assigned to the element. This means that the stiffness matrix of each element can be determined and assembled into a global stiffness matrix. When solving structural problems the force is often known, which means that the unknown coefficient usually is the displacement. Still, as long as two of the coefficients are known, the third can be found. Knowing the stiffnesses, forces and displacements makes it possible to calculate other results such as reaction forces, stresses, and strains.

The application of the direct stiffness method is shown below by an example with two one-dimensional springs, where one is constrained and the other is applied a load P. This can be discretized into two spring elements, each with a stiffness K_i and nodes at both ends. Assume that the stiffnesses $k_1 = k_2 = k$. As the springs are connected to each other at nodal points, a node from each spring can be made shared resulting in a system with a total of three nodes as shown in 3.3.

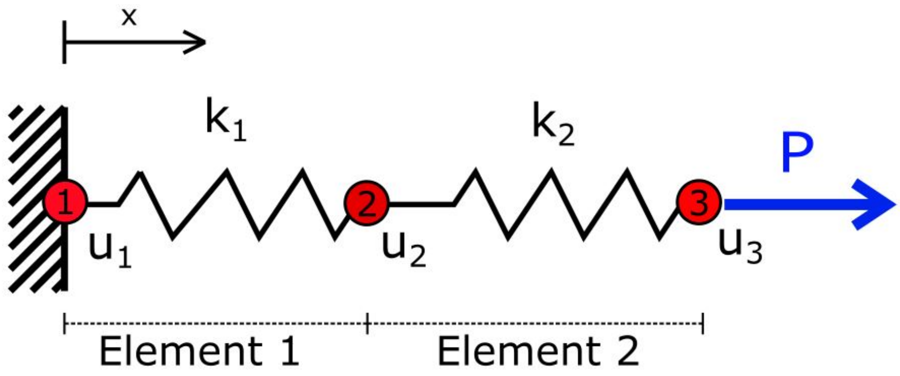

Fig. 3.3. Example: loaded springs

We begin by recognising that Hooke's law applies for the problem;

$$\text{Hooke's law:} \qquad F = -kdx$$

Then the problem is separated into two one-dimensional spring elements;

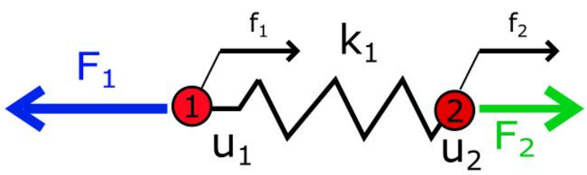

Fig. 3.4. Element 1

Hooke's law can be rewritten in terms of local stiffness, forces and displacements. For element 1 this looks like;

$$\begin{aligned} F = -f_1 &= k_1(u_2 - u_1) \\ f_1 &= k_1(u_1 - u_2) \\ F = f_2 &= k_1(u_2 - u_1) \\ f_2 &= k_1(-u_1 - u_2) \end{aligned}$$

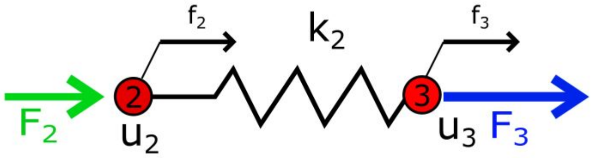

Fig. 3.5. Element 2

For element 2;

$$
\begin{aligned}
F = -f_2 &= k_2(u_3 - u_2) \\
f_2 &= k_2(u_2 - u_3) \\
F = f_3 &= k_2(u_3 - u_2) \\
f_3 &= k_2(-u_2 + u_3)
\end{aligned}
$$

This can be written as force-displacement relationship in matrix form;

$$
\begin{Bmatrix} f_1^{(1)} \\ f_2^{(1)} \end{Bmatrix} = \begin{bmatrix} k_1 & -k_1 \\ -k_1 & k_1 \end{bmatrix} \begin{Bmatrix} u_1 \\ u_2 \end{Bmatrix}
$$

$$
\begin{Bmatrix} f_2^{(2)} \\ f_3^{(2)} \end{Bmatrix} = \begin{bmatrix} k_2 & -k_2 \\ -k_2 & k_2 \end{bmatrix} \begin{Bmatrix} u_2 \\ u_3 \end{Bmatrix}
$$

We can then start assembling the global stiffness matrix [K] and global nodal force vector {F};

$$
K = [K] = \sum_{e=1}^{N} k^{(e)} \qquad F = \{F\} = \sum_{e=1}^{N} f^{(e)}
$$

Where e is the element number

We can write the nodal equilibrium equation at each node as;

$$
F_1 = f_1^{(1)} \qquad F_2 = f_2^{(1)} + f_2^{(2)} \qquad F_2 = f_3^{(2)}
$$

$$
\begin{aligned}
F_1 &= k_1 u_1 - k_1 u_2 \\
F_2 &= (-k_1 u_1 + k_1 u_2) + (k_2 u_2 - k_2 u_3) \\
F_3 &= -k_2 u_2 + k_2 u_3
\end{aligned}
$$

From this we can assemble the global matrix system;

$$\begin{Bmatrix} F_1 \\ F_2 \\ F_3 \end{Bmatrix} = \begin{bmatrix} k_1 & -k_1 & 0 \\ -k_1 & k_1+k_2 & -k_2 \\ 0 & -k_2 & k_2 \end{bmatrix} \begin{Bmatrix} u_1 \\ u_2 \\ u_3 \end{Bmatrix}$$

We can then apply boundary conditions. For this case we know that there is no movement at the constraint in node 1 so $u_1 = 0$:

$$\begin{Bmatrix} F_1 \\ F_2 \\ F_3 \end{Bmatrix} = \begin{bmatrix} k_1 & -k_1 & 0 \\ -k_1 & k_1+k_2 & -k_2 \\ 0 & -k_2 & k_2 \end{bmatrix} \begin{Bmatrix} 0 \\ u_2 \\ u_3 \end{Bmatrix}$$

We can ignore the equation for F_1 and continue with just the equations for F_2 and F_3. From here it is just a matter of solving the equations with respect to u_2 and u_3. In this example, the external force is equal to P and the stiffness for both springs are the same $k_1 = k_2 = k$. This means that $F_3 = P$, and $F_2 = 0$ as there is no global force applied to node 2. For the system to be in force equilibrium, the reaction force at node 1 has to be $F_1 = -P$.

3.1.2 Application of FEM: Galerkin's method

Galerkin's method is a form of weighted residuals approach. It is used for approximating the solution of differential equations. First, a solution function is assumed for the differential equation, which needs to be valid for the boundary conditions. The assumed solution will have a certain number of unknown coefficients. From the assumed solution, we can make the so-called weighting functions. These follow the same form as each part/unknown coefficient of the assumed solution. Simple differential equations can be solved and there is a possibility that the assumed solution is correct, but in the instances where the weighted residual approach is useful, we know that there will be an error in the end. This error is called the residual. The governing differential equation can be set to zero for the analytical solution, but in this case, the zero is replaced with a residual, R. The weighing functions can then be multiplied with the residual and integrated throughout the element. The output will be the unknown coefficients, which can then be put into the assumed solution function.

Below is a simple example of solving a structural problem governed by a differential equation using weighted residuals with Galerkin's method.

Determine the function *U(x)* for displacement of the simply supported beam of length L and subjected to moment M_0 at both ends. Assume that EI is constant and the boundary conditions $U(0) = 0$ and $U'(0.5L) = 0$.

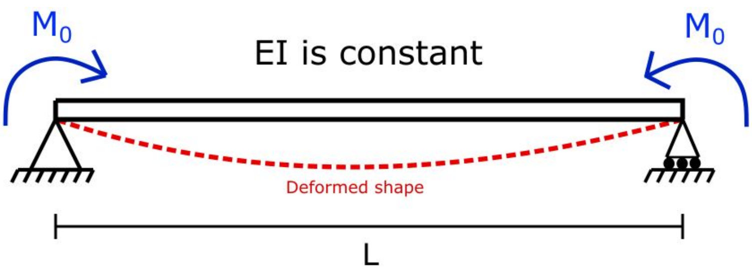

Fig. 3.6. Example: simply supported beam under pure bending

The governing differential equation is;

$$EI\frac{d^2U(x)}{dx^3} - M(x) = 0$$

$$\text{Analytical solution:} \qquad U(x) = \frac{M_0L^2}{2EI} - \frac{M_0Lx}{2EI} = \frac{M_0}{2EI}(x^2 - Lx)$$

Where $M(x) = M_0$ for all values of x in this problem. This is a simple problem that can be solved analytically to get the exact solution. The analytical solution is displayed above, but to illustrate how Galerkin's method can be applied to approximate the solution we assume that the analytical solution is unknown.

We start by assuming a solution for the displacement function $U(x)$. This is called a "trial function" and it must respect the boundary conditions of the problem. For this example we will assume it to be;

$$U(x) = A\sin\frac{\pi x}{L}$$

Where area A is an unknown coefficient. We then define the residual function, or error function by replacing the 0 in the governing DE to R;

$$EI\frac{d^2U(x)}{dx^3} - M(x) = R$$

Where:

$$\begin{aligned} U(x) &= A\sin\frac{\pi x}{L} \\ \frac{dU}{dx} &= A\frac{\pi}{L}\cos\frac{\pi x}{L} \\ \frac{d^2U}{dx^2} &= -A\frac{\pi^2}{L^2}\sin\frac{\pi x}{L} \end{aligned}$$

Substituting the equations yields;

$$R = EI(-A\frac{\pi^2}{L^2}\sin\frac{\pi x}{L}) - M_0$$

Galerkin's method is solved by taking the integral of the residual equation, R, times a weighting function, Φ and set it equal to 0.

$$\int_0^L \Phi_i R dx = 0 \qquad i = 1, 2, \ldots \text{ unknown coefficient}$$

The weighting functions are chosen to be of the same form as each part of the approximate solution to $U(x)$. In this example we only have one unknown coefficient A, therefore we only need one weighting function, Φ_1 over one integral $\int_0^L$. For this example we use the weighting function;

$$\Phi_1 = sin\frac{\pi x}{L}$$

Substitute in Φ_1 and R, then solve for A;

$$\int_0^L \sin\frac{\pi x}{L}\left[EI(-A\frac{\pi^2}{L^2}\sin\frac{\pi x}{L}) - M_0\right]dx = 0$$

Solving for A gives;

$$A = -\frac{4M_0L^2}{\pi^3 EI}$$

A is then substituted back into our assumed solution;

$$U(x) = -\frac{4M_0L^2}{\pi^3 EI}\sin\frac{\pi x}{L}$$

This is the approximated solution for the deflection function of the simply supported beam. A comparison between the exact solution and the approximation is displayed in Table 3.1, which shows that the error is only a few percent.

x	Galerkin	Exact
0	0	0
L/4	-0.091$\frac{M_0L^2}{EI}$	-0.094$\frac{M_0L^2}{EI}$
L/3	-0.112$\frac{M_0L^2}{EI}$	-0.111$\frac{M_0L^2}{EI}$
L/2	-0.129$\frac{M_0L^2}{EI}$	-0.125$\frac{M_0L^2}{EI}$

Table 3.1. Comparison between Galerkin's method and the exact solution

3.2 Deciding the approach for the model

3.2.1 Mathematical Model

When deciding on an appropriate mathematical model, the physical problem in question needs to be assessed. The aim is to "construct an abstract representation of a structure which can capture its structural behavior" (Bucalem & Bathe, 2011, p. 2). Some FEM-software such as Ansys have capabilities to conduct several types of analysis depending on what type of calculation needs to be considered. Examples of some of the analysis packages provided by Ansys are thermal, fluid, static and dynamic analysis (ANSYS, Inc, 2020c). Engineers working in different fields may only be interested in specific results depending on the type of engineering field they are in. If a structural engineer were to design a residential building, then fluid simulation might not be relevant, unless wind performance is critical. But in general, a building not subjected to any dynamic loads would be modelled as a static structural problem, where the changes in applied loading are slow enough that dynamic influence is negligible.

The physical problem in question, is the experiment by R. Yang et al. (2020). A bolted hybrid steel to timber composite (STC) connection, between an H-section and two glulam elements, was tested by applying load to the H-section with a hydraulic press. This is known as a push-out test and an illustration showing the configuration of the experiment is shown in figure 4.3a. Several connection configurations were tested, but this work is based on the configuration named "Group A" in R. Yang et al. (2020). The objective was to investigate the failure modes and yield characteristics of the connection. Looking at the loading regime for the test, the rate of load applied was low suggesting a static behavior. Deformation and load were measured, before load-slip graphs were made showing the correlation between the two. Plastic deformation was experienced by the glulam elements and the bolts, thus the analysis needed to be able to consider non-linear analysis. By evaluating this information, the necessary results would be stresses, deformations and loads. It was decided that a suitable approach would be to proceed with a structural model using the "static structural analysis" feature in Ansys Mechanical, as it contains all the previously mentioned calculation abilities.

Another challenge however, is to capture crushing of timber when using FEM. Not only does timber have distinctive strength characteristics based on grain direction, dowel bearing tests also show varying mechanical properties when small areas of the timber are compressed by dowels, bolts or nails.

3.2.2 Foundation material model

The crushing phenomenon was reported by R. Yang et al. (2020) in their experiment, which made crushing an important factor for the model to consider. Crushing in timber cannot be captured with strength results obtained from standard uniaxial tests. The behavior of the wood in the interaction between dowels, is determined by the wood fibres themselves. Compared to standard uniaxial tests, the embedment tests typically show a more rapid deformation of the timber. This points to a lower modulus of elasticity (MOE) than what is usually observed for global compression in timber. Hassanieh et al. (2017) also attributes some of this strength weakening to the fact that drilling of holes in timber can cause damage to the fibres. This incited the need for an alternative modeling approach. By researching existing literature on the subject, several proposed methods were found. The foundation material model (FMM) in the article by Hong (2007) showed promising results and was also modelled with Ansys, which is why this method was adopted for this work. The FMM aims to simulate the crushing behavior of timber more accurately, by assigning a separate timber material around the holes with material properties obtained from dowel bearing tests. An illustration of a typical dowel bearing test can be seen in figure 3.7. A dowel bearing test is prepared by taking a woodblock of some wood species, drill a half hole on one side of it, inserting a dowel before a load is applied evenly on the bolt. It is important that load is distributed evenly on the bolt, to prevent it from bending. By registering the load and the deformation of the timber, the dowel bearing strength or embedment strength of the timber can be determined. In figure 3.7 the specimen is oriented so the load is applied parallel to the grain direction, but the test would be repeated in other directions as well.

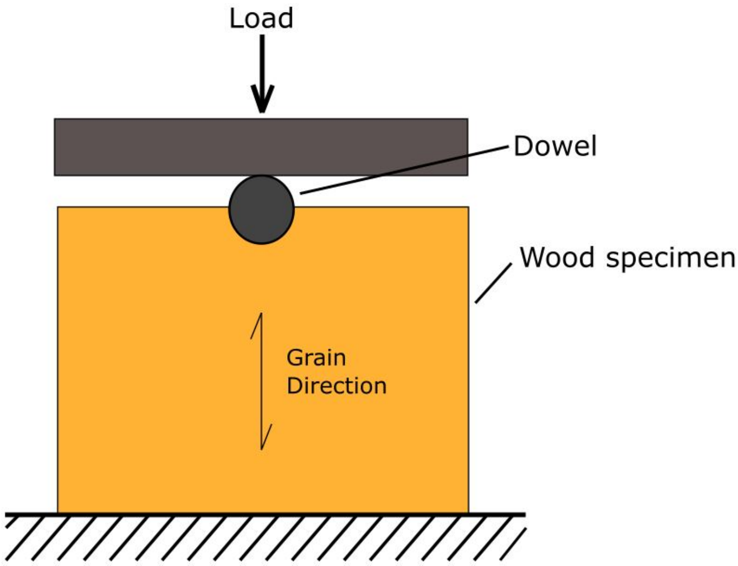

Fig. 3.7. Dowel bearing test

3.3 Simplified models approach

This section was included because it was a technique that was used extensively during the development of the model. Creating a model can be challenging, as many parameters and settings need to be considered and understood before logical decisions can be made. Sometimes a trial and error approach may be necessary, to visualize the impact the different settings have on the results. Large models can take a considerable time to run, which makes the process of trying out settings time-consuming. Errors are not uncommon either, which at times can be hard to identify the cause of. By making separate models that are smaller and simpler make this process much easier and more efficient. Reducing the size means reducing the risk of something going wrong, and if it does then finding the reason for it is easier when fewer elements have to be investigated. An example of a model that was made was one with just one bolt and shorter lamellas and H-section. The fundamental problem still remains, analysing the behavior of bolted STC connections, but testing out improvements takes considerably less time. This enables errors to be overcome and the optimal settings to be found, before implementing them in the main model.

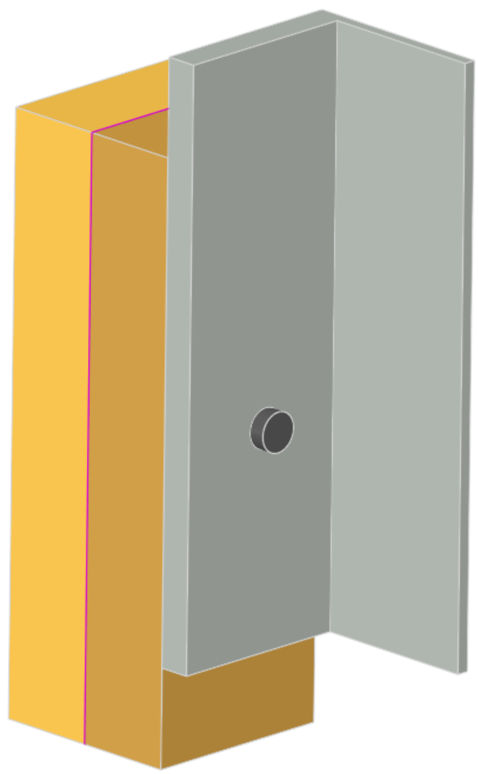

Fig. 3.8. Simplified model with a single bolt

4. Application

4.1 Overview

This chapter aims to show the application of the finite element method through structural analysis using Ansys Mechanical 2020 R2 (ANSYS, Inc, 2020b). This is a student licence that has some limitations when it comes to the size of the model. A maximum of 128K nodes/elements can be defined. An effort has therefore been made to take measures to reduce the problem size of the model. The order of the sections in this chapter follows the same order as the analysis outline in Ansys which is shown in figure 4.1. Explanations for each step are given together with arguments as to why certain settings have been chosen for the analysis.

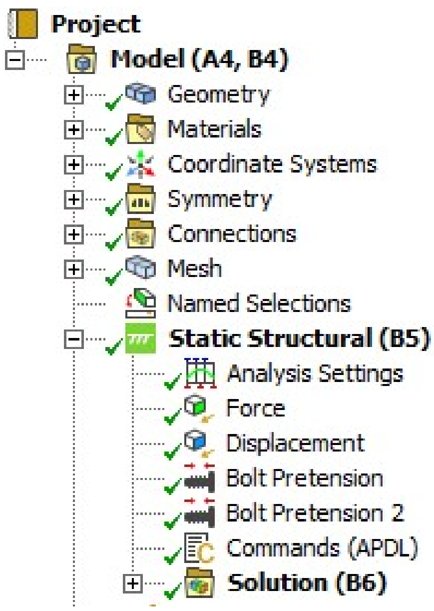

Fig. 4.1. Analysis outline

4.2 Geometry

This section contains the methods used for creating the geometry. These steps were done in a software called SpaceClaim 2020 R2 (ANSYS, Inc, 2020a) prior to transferring the geometry model to Ansys.

4.2.1 Coordinate system

The coordinate system used is shown in figure 4.2, with a red, green and blue axis. This corresponds to the x-,y- and z-axis respectively. This system has been chosen to match the direction of the timber as presented and explained in the theory chapter. The x-axis points in the longitudinal direction, the y-axis points in the tangential direction, and the z-axis points in the radial direction.

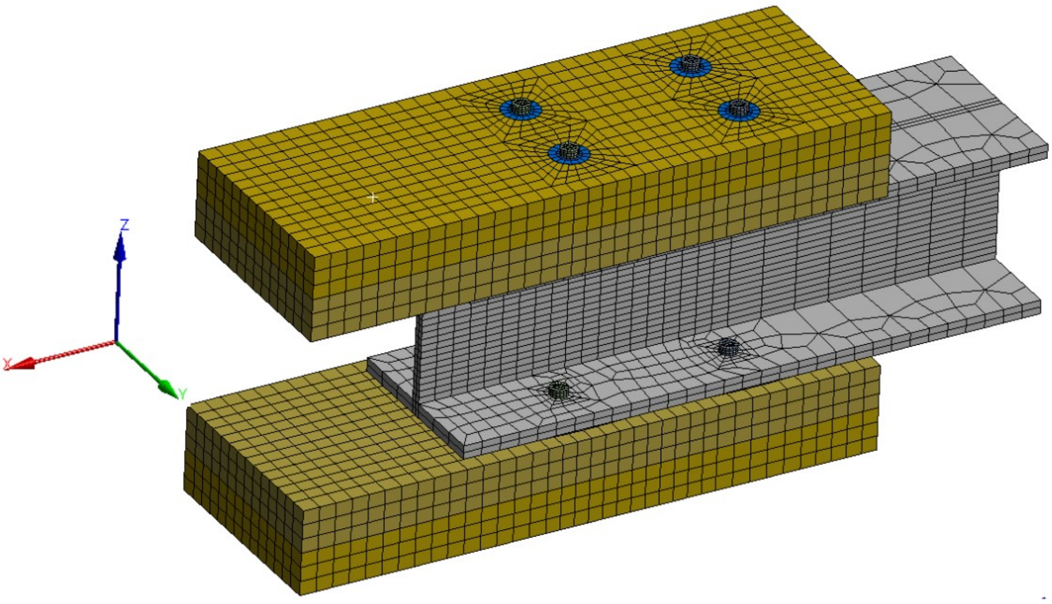

Fig. 4.2. Model geometry and coordinate system

4.2.2 Dimensions

The same dimensions as the original experiment by R. Yang et al. (2020) have been used in the model. However, some minor differences exist which will be presented in the next subsection. The steel element used is a 100 x 100 mm H-section, with the thickness of flange 8 mm and of web 6 mm. Eight M6 bolts, four on each flange, connect the glulam elements to the steel section. Each bolt is threaded across the entire length, with a washer and a hexagonal nut attached to both ends. Each glulam element is made up of two 25 mm thick Dahurian larch lamellas, which are glued together. Figure 4.3 shows the experiment setup next to the Ansys model. Note that a full model is displayed, however, this is just a mirroring effect in Ansys. The actual model is just a quarter of the full model.

4.2.3 Geometry differences and simplifications

The greatest difference between the model and the experiment is that only a quarter of the geometry has been modelled for the analysis. Because the specimen from the experiment is symmetric around two planes, symmetry can be introduced to the model and reduce the size. This is a common technique to utilize for FEM analysis involving geometry with symmetry planes and was also done in the models by Hassanieh et al. (2017) and Nguyen and Kim (2009). The advantage of symmetric models compared to full models is the significant reduction of the total number of nodes and elements, which in turn makes for a lower computational cost. This leads to another benefit which is the possibility of mesh refinements in critical areas of the model, that otherwise could

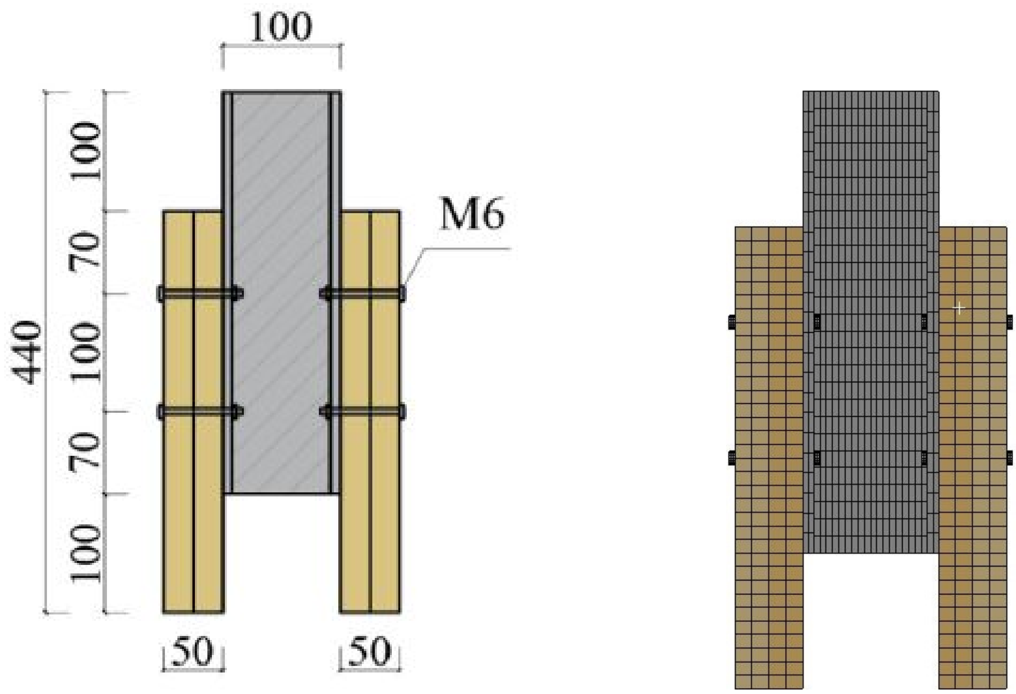

(a) Experiment dimensions (R. Yang et al., 2020)

(b) Ansys model

Fig. 4.3. Side-by-side comparison of model and experiment

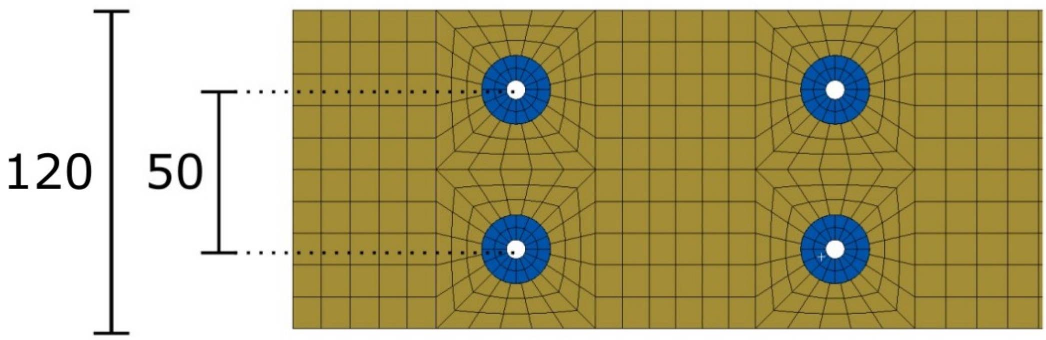

Fig. 4.4. Width of lamella and horizontal distance between holes

not be possible due to the problem size limit of the academic license. Figure 4.5 shows where the symmetry planes are located.

In real life application, assembling bolted connections can be challenging as the margins required to align holes and then fit bolts in them are slim. A common solution is therefore to make what is known as clearance holes, which are slightly larger than the diameter of the bolts. In the experiment, the holes are 1 mm larger than than the actual bolts. Initially, the model was made just like in the experiment, but a problem became apparent when assigning the contact elements between the bolts and the interior walls of the holes. Since contacts are defined between parts that touch each other, Ansys had trouble understanding why contact was defined when the bolts and the holes were not actually in contact. The first stage of the analysis would be the bolts moving until they came into contact with the holes, known as rigid-body motion. Rigid-body motion is not allowed in static-structural analysis (ANSYS, Inc, 2010). A decision was therefore made to make the dimension of holes and bolts the same, to avoid this problem.

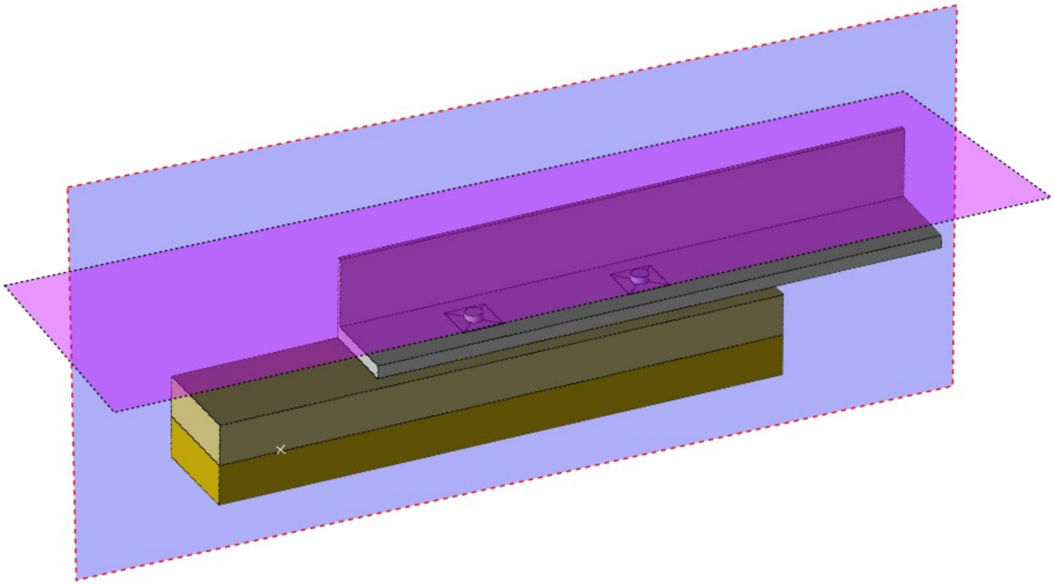

Fig. 4.5. Symmetry planes in the model

A minor simplification was done to the geometry of the H-section. The radius between the step and the flanges was ignored, as it was assumed to not play a critical role in the experiment and therefore just adds unnecessary detail to the model.

(a) H-section in the experiment (R. Yang et al., 2020)

(b) Simplified H-section

Fig. 4.6. H-section differences

As mentioned in 4.2.2 the bolts used in the experiment are threaded across the entire length. Modelling threads is possible to do when creating the geometry for the bolts and the holes, but it is time-consuming and makes for a more complicated analysis. Measures to reduce the problem size were constantly in mind, and the conclusion was that the extra nodes and elements required for modeling threads would be better spent elsewhere. This is the reason why the bolt shanks were modelled as solid cylinders, and frictional contact between the bolts and the holes was established instead. Simplifications were also done to the nuts, which were modelled as round rather than hexagonal as the nuts in the experiment. The width of the nuts was not specified in the experiment, but were assumed to meet the standard width of 10 mm following the American standard on hex nuts (ASME, 2010). The nuts and bolt shanks were finally combined into one solid element, as the experiment showed no signs of the nuts being torn off. This resulted in no additional contacts to be assigned between the shanks and the nuts. The simplified bolt geometry is shown in figure 4.7.

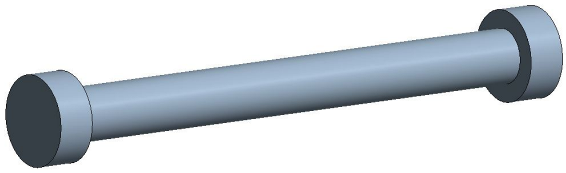

Fig. 4.7. Simplified bolt model

4.2.4 Shared topology

Shared topology is a feature in Spaceclaim that allows the user to share the nodes at the interface between objects in contact. This creates what is known as "multi-bodied parts" in SpaceClaim. When transferred to Ansys these parts act as bonded together, which eliminates the need to define bonded contacts in Ansys. Sharing nodes between elements reduces both the node count and the number of contact elements. One drawback to this however, is that local mesh refinements can be restricted. Two parts that have shared topology can not be meshed differently, since the mesh must align with the shared nodes. The foundation material in the model was expected to deform significantly more than the rest of the timber, so there is a need for a finer mesh in this part of the model. Bonded contact between the foundation material and the general timber material was used instead, to allow the foundation to be meshed separately. Shared contact was therefore only used in the adhesive layer between the two lamellas, and also on the interface between the foundations.

4.2.5 Foundation material geometry

The radius of the cylinder for the foundation material was set to 1.8*d, where d is the diameter of the hole. This value was determined by Hong (2008), who compared physical dowel bearing tests with tests modelled in Ansys. It was stated by Hong (2007) that the multiplier for the radius was an empirical value defined to contain the crushing of the timber, without reducing the material integrity of the surrounding timber. However, the value was based on tests done on Douglas-fir with a larger bolt diameter of 12.4 mm. A similar study on Douglas-fir was conducted by Leitner (2011) who used the same methodology as Hong (2007), but also performed tests with 6.4 mm bolts which are closer to the 6 mm bolts used in the experiment by R. Yang et al. (2020). No similar work could be found on Dahurian larch, thus the same radius for the foundation as utilized by Leitner (2011) and Hong (2007) was used for this model.

4.2.6 Mesh refinement guidelines

There are some convenient measures that can be taken in SpaceClaim when creating the geometry, that can simplify the meshing process. Parts of the model that experience high stresses, deformations, or have certain geometric shapes, can be sensitive to the mesh selection. An example of shapes that require delicate handling are curves such as holes and cylinders. Identifying challenging areas of the model early makes it possible to utilize some useful techniques. Ansys will not always provide the most suitable mesh when encountering these shapes, providing boundaries that can be used to affect the mesh can therefore be helpful. A technique used for this work was creating "guidelines" for the mesh around the holes. The guidelines were made by drawing lines on the faces of the lamellas and the H-section in SpaceClaim. The first step was to draw a square around the holes, and then diagonals from the corners of the squares to the edge of the holes. This split the larger face into smaller faces around each hole, which can be selected for mesh refinements in Ansys Workbench later.

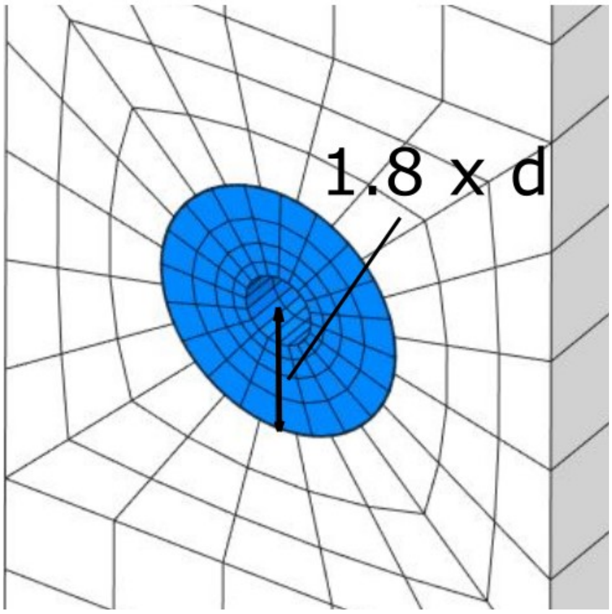

Fig. 4.8. Foundation material radius as defined in Hong (2007)

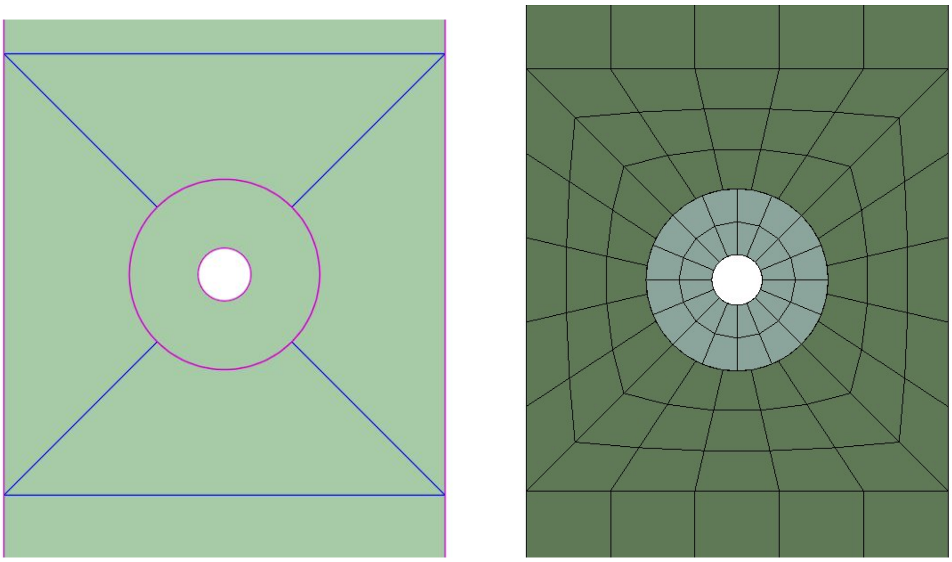

(a) Mesh refinement guidelines

(b) Resulting mesh

4.3 Contacts

Contact elements are used to define the behaviour between parts of the model that are touching. Ansys offers several types of contacts, but for this work, only two types have been used and these are frictional and bonded. Frictional contacts are used for parts that are in contact but can slide independently of each other while causing friction. The magnitude of the friction has to be expressed by the right frictional coefficient, which has to be specified in Ansys. Bonded contacts are used for parts that are fixed together, and they do not allow any independent movement or separation of the bonded objects.

4.3.1 Contact formulation

Several contact formulations are available in Ansys, which affect how the contacts behave. The default setting is the "pure penalty" method, which has been used for all the contacts in the model (ANSYS, Inc, 2004). Pure penalty allows some penetration to occur between contacting bodies to fulfill the equilibrium equations in each iteration. It is therefore necessary to assess the penetration results in the solution to determine if the penetration is acceptable. This can be done by comparing the penetration to the local deformation or the dimensions of the geometry, to see if it is considerably large or not. Actions to reduce the penetration can be taken by changing the penetration tolerance or increasing the normal stiffness of the contact. For this work, these settings have been left as program controlled. The normal stiffness was set to be updated for each iteration, as this is recommended by the Ansys user manual if there is uncertainty surrounding the normal stiffness factor (ANSYS, Inc, 2010). This allows Ansys to change the contact stiffness in each iteration, to minimize the penetration.

4.3.2 Contact behaviour

When defining contact between parts in the model, a "target" and a "contact" body have to be selected. This is only relevant for certain behaviour types associated with the contact. One of these behaviours is called "asymmetric" which means that all contact elements are assigned to one body while all the target elements are assigned to the other. The effect this has is that penetration between the contact and the target element is allowed. A contact element can never penetrate a target element, but a target element can penetrate a contact element (ANSYS, Inc, 2004). There are some general advice that can be followed to determine which body should be the target and which body should be the contact.

One recommendation from the Ansys manual is that the more rigid object of the two should be the target, and the less rigid one should be the contact (ANSYS, Inc, 2004). There are however many exceptions to this rule, which can make the choice unclear. An alternative is to use "symmetric" behavior. Instead of defining a designated target and contact body, this behaviour assigns contact pairs consisting of target and contact elements to both bodies. This doubles the number of contact elements, thus making it less efficient (ANSYS, Inc, 2004). But it does reduce the risk of penetration between the bodies. After some testing of the model in the early stages, defining the appropriate target and contact bodies proved challenging, resulting in excessive penetration. Symmetric behaviour was therefore chosen for the contacts instead.

4.3.3 Contact types

Only bonded and frictional contacts have been used for the model. Bonded contact was established between the foundations and the rest of the lamellas, as the foundations were meant to behave as part of the lamellas themselves and not as separate pieces. As previously explained, shared topology could also be used to get bonded contact, but this method would restrict the mesh refinements options for the foundations. The remaining contacts were frictional, which required a frictional coefficient to be specified. A frictional coefficient of 0.7 was used for steel to timber contacts, which includes bolt shanks to holes, bolt heads to lamellas, lamellas and foundations to the H-section. This value was taken from Hong (2007), but another study by Mckenzie and Karpovich (1968) on the frictional behaviour between wood and steel suggested a similar value of 0,65. For steel to steel contacts, which include the contact between bolt shanks to the holes and bolt heads to the flanges, a frictional constant of 0,3 was used. This was the same value used by Hong (2007) and is also supported byFarris et al. (2003) who stated that metal to metal friction coefficients are of the order 0.1-0.3.

Table 4.1. Contact settings overview

Contact bodies	Formulation	Contact type	Behaviour	Update normal stiffness	Frictional constant
Foundations to surrounding timber	pure penalty	bonded	symmetric	each iteration	none
Bolt shanks to timber	pure penalty	frictional	symmetric	each iteration	0.7
Bolt heads to timber	pure penalty	frictional	symmetric	each iteration	0.7
Lamella to H-section	pure penalty	frictional	symmetric	each iteration	0.7
Foundations to H-section	pure penalty	frictional	symmetric	each iteration	0.7
Bolts shanks to H-section	pure penalty	frictional	symmetric	each iteration	0.3
Bolt heads to H-section	pure penalty	frictional	symmetric	each iteration	0.3

4.4 Meshing

When loading the geometry model into Ansys, an automatic unstructured mesh will be created with some default settings. For simple models, this mesh may be sufficient. But when challenging geometry is involved, it might take some changes to produce a more suitable mesh. For this model, curved elements in the form of holes, bolts and foundation materials were involved. By assessing the automatic mesh, it became clear that it did not represent the geometry well around these areas of the model. The bolts, holes and foundations were also the parts of the model thought of as the most critical, as the experiment showed large localized deformations in these areas. Therefore, a finer mesh was assumed to be necessary for these areas of the model. Ansys is not capable of predicting what the critical parts of the model are, so it will not understand that mesh refinements are required in certain locations. It all comes down to the user's judgment to create an appropriate mesh for the problem.

4.4.1 Element types

By default, Ansys will choose tetrahedral elements for the mesh. Even though tetrahedral elements are capable of representing geometric shapes well, there are some disadvantages to them. One of these is the risk of "shear locking", which can result in artificially stiff elements (Rohan et al., 2017). Another is the high mesh density they produce with a large number of nodes. An alternative element type is hexahedral elements. Individually, these elements contain more nodes than individual tetrahedrons, but far fewer hexahedrons are needed to generate a mesh. This significantly reduces the computational cost of the analysis and several studies have suggested it does this without sacrificing accuracy (Cifuentes & Kalbag, 1992). Because of this, the mesh was chosen to be built up by hexahedrons using the "multizone" mesh setting in Ansys. This was used for the entire model, but other refinements were also done in the critical parts.

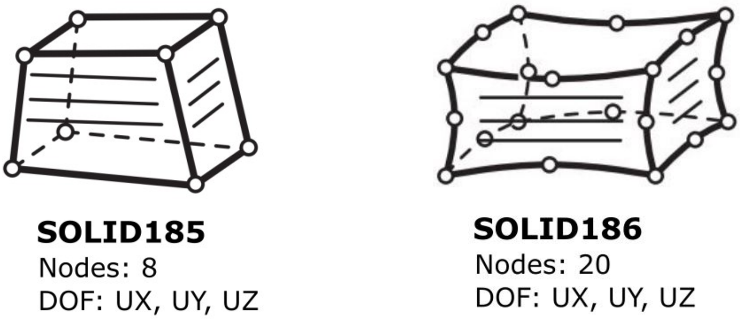

(a) SOLID185 (b) SOLID186

Fig. 4.10. Linear and quadratic hexagonal mesh elements tested in the model (ANSYS, Inc, 2011)

The number of nodes in the elements can also be altered. Hexahedrons are a part of the "SOLID" element type family, which includes multiple types of hexahedrons with a varying number of nodes. This is referred to as the "order" of the element. A higher-order element has more nodes than a lower-order one. In Ansys, this can be specified by selecting "linear" elements for lower order types, or "quadratic" for higher-order types. With a hexahedron mesh, linear elements used are the 8-node SOLID185 and 20-node quadratic SOLID186. The default setting is quadratic, but this means generating a mesh with substantially more nodes than with linear elements. This translates to an increase in computational cost, but the level of accuracy is in many cases higher (Ferris, 2020). A reason for this is that the extra nodes are found on the mid-sides of the elements. This makes quadratic elements better suited for representing curved elements and produce more integration points, which reduce the interpolation and extrapolation region in each element (Younis, 2010). Both element orders were tested to see if there was any significant change in the accuracy, and if the increase in computational time for quadratic elements was worthwhile.

4.4.2 Mesh sensitivity study setup

The meshing process is an important step in FEA, and it is crucial to apply an appropriate mesh for the results to be accurate. A common way to check if the results obtained are accurate or not, is to rerun the analysis with a finer mesh. If the results change substantially, it can indicate that the initial mesh was too coarse. If further refinements show less change in the results, it suggests that the solution is approaching the actual solution of the problem. Finer meshes take longer to run, and in some cases, there might be limitations to the number of elements and nodes the software will allow you to analyse. Which is the case with the student licence from Ansys used for this work. Still, a small mesh sensitivity study was conducted using two different levels of mesh refinements for the model. These were categorised as coarse and fine. The focus was on the result differences and computational time. Table 4.2 shows the relevant mesh settings and the resulting node and element count for both cases.

Integrated with the multizone mesh is the option to choose "sweep body size", which will sweep the mesh body by a certain incremental size. This option together with the "body-size" feature was used extensively to adjust the size of the elements in the critical parts. Another setting used for the foundations was the "face mesh". This was applied to the faces of the foundations and used to control the number of divisions in the mesh. Zero divisions mean that an element in the

Table 4.2. Mesh sensitivity study overview

	Bolt mesh		Foundation mesh			
Case	sweep size (mm)	body size (mm)	sweep size (mm)	body size (mm)	no. of face mesh divisions	node/ element count
Coarse	8	8	8	8	1	15603/ 2615
Fine	4	5	4	5	2	21193/ 3645

foundation will be in contact with the bolt on one side and in contact with the surrounding timber material on the other. Increasing the number of divisions will therefore split larger elements into smaller ones.

4.5 Static structural

4.5.1 Analysis settings

The loading regime was divided into 24 load steps. The lack of numerical load data from the experiment, meant that figures provided in R. Yang et al. (2020) had to be used to be interpreted. A minimal amount of tick marks were on the axes, which made it difficult to determine the exact values. Every half a millimeter of slip was marked on the x-axis in the load-slip result for the Group A configuration. This amounted to a total of 24 tick marks which is why 24 load steps were used. The first being the step where only the bolt pretension is initiated. "Auto time stepping" was turned on which allows Ansys to adjust the time increments for each load step to optimize the chance for convergence (ANSYS, Inc, 2009). The end times of the steps were still specified, but these just served the purpose of plotting the results to make them comparable to the experimental results. The number of substeps was set to an initial 100, minimum 10 and a maximum of 1000. This tells Ansys to attempt to converge each load step in 10 substeps. If that does not happen, it will then try to converge the load step within 100 substeps. Once the convergence of the load step is reached, Ansys will move over to the next load step and repeat the same procedure. If 100 substeps are not sufficient, a final attempt at convergence will be done with 1000 substeps.

The large deflection option enables Ansys to account for the stiffness change due to shape deformations of the elements (ANSYS, Inc, 2009). By default, Ansys assumes that the deformations are small and neglects the impact on the stiffness. Even though the experiment showed large deformations of the timber surrounding the bolts, it was not clear if the correct way to proceed was by activating large deflection or not. Both options were therefore tested to see which one produced the most similar results to the experiment.

When frictional contacts have friction coefficients greater than 0.2, an error message recommending to activate the "unsymmetric Newton-Raphson option" will be generated by Ansys. Other FEM-software, like Abaqus, activates this automatically (Boulbes, 2020). Friction cause unsymmetric terms to be added to the equations. The higher the friction coefficients, the greater these terms become. This can cause convergence issues, which was the case for the model (Boulbes, 2020). After activating unsymmetric Newton-Raphson, the analysis was able to be completed. The trade-off is that the computational cost for the unsymmetric option is twice as high as the symmetric.

4.5.2 Loading regime

The loading regime was adopted from the experiment. However, the exact load data was not available. The load-slip average curve provided in the article was therefore used to read off the load as accurately as possible. The load was then combined with time increments corresponding to the load duration in the experiment, before being divided by four to get the reduced symmetric load that was transferred to Ansys. The loading regime used in the model can be seen in figure 4.11b next to the full load applied in the experiment. At about the 2-minute mark, the loading in the experiment was decreased before ramping it up to the maximum load. This part of the loading regime was ignored because it did not affect the results after the loading was increased again, and essentially added unnecessary computational time.

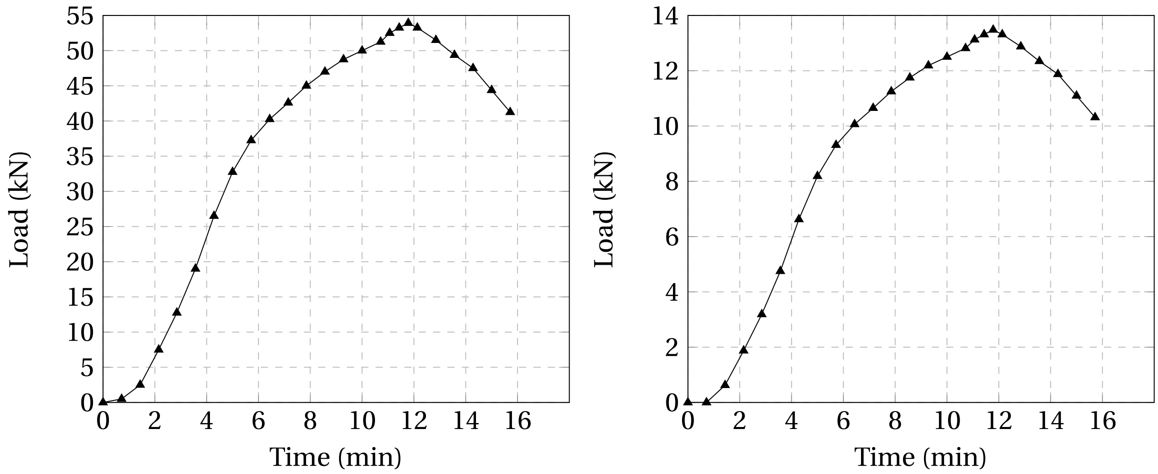

(a) Full load as in the experiment

(b) One quarter of the load as applied in the model

Fig. 4.11. Loading regime

4.5.3 Constraints

The bases of the lamellas were constrained in all three directions, in contrast to the experiment where the specimen was supported in the x-direction only. This was done with the "displacement" tool in Ansys where the displacement in the x-,y- and z-direction were set equal to zero. Constraining the model in just the x-direction was initially attempted, but the model experienced problems with convergence after a while. Since the only external load is applied in the x-direction, it was assumed to not be necessary to constrain it in the other directions. But after adding the other constraints, the model ran much quicker and was able to complete the analysis. Adding constraints removed DOFs and made the problem easier to compute. Nevertheless, the results up to the point where the initial model failed to converge, were nearly identical. The reaction forces in the y- and z-direction was checked to verify that they were small, otherwise there might be an instability issue with the model.

Constraints are needed at the symmetry planes, but when symmetry regions are defined in Ansys it automatically puts constraints in these regions which prevent the model from deforming normal to those planes. Alternatively, two frictionless supports could replace the need for symmetry regions. But an added benefit with defining symmetry was the option to mirror the model, which allowed the full model to be visualized.

4.5.4 Bolt pretension

An interesting result from the experiment was the occurrence of a "no-slip zone" at the first stage of the load-slip curve. Slip was not experienced as the load was initially being applied, and YANG concluded that this was caused by the pretension in the bolts. However, no information about the magnitude of the bolt pretension load was available from the experiment. A trial and error approach was therefore used to find a pretension force that would produce similar results as in the experiment. Bolt pretensioning of 0.5 kN, 1.0 kN, and 2.0 kN were applied to the faces of both bolt shanks and tested. The pretension was increased from zero to the specified load during the first load step, before being "locked" for the remaining load steps. This means that after the pretension has been set to lock, the load in the bolt is free to vary depending on the external loads being applied. If the bolt pretension is set to load while external loads are applied, the bolt will attempt to keep a constant load in the bolt through the whole simulation. This is not realistic, and it is therefore important to only apply external loads when the bolt pretension is set to lock.

4.5.5 APDL commands

APDL commands can be inserted into Ansys Mechanical, to activate certain features which are not available through the regular interface. The only APDL command used for the model was the "ERESX, NO" command. When Ansys reports the stress and strain results, it will extrapolate the results from the integration points to nodes by default. This is done to display the solution for the user, since integration points, unlike nodes, are not visible. For linear elastic elements, this method generally works well. The problems begin when the element is getting close to yielding. If the result at the integration point is just below the yield strength, the extrapolation might cause the nodal result to show a higher stress value than yield, especially for larger elements where the distance from the integration point to the nodes is considerable. This can cause some discrepancies in the stress-strain diagrams, where the yield point can be difficult to represent. The ERESX, NO command tells Ansys to copy the results at the integration points directly to the nodes without extrapolation (ANSYS, Inc, 2009).

4.6 Timber material properties

Ansys does not have an incorporated timber material definition, but has an extensive selection of options aimed at other materials such as steel. Therefore the material definition for the timber had to be adapted to fit these material definitions. This was done based on the material definitions proposed by Hong (2007) and Leitner (2011). The model had to account for plastic deformation following the experimental test results. To include plasticity, a bilinear isotropic hardening rule was defined. This requires an initial MOE, a yield point and a tangent modulus for the hardening rule in the plastic region.

Yield strength is used extensively for strength testing of metals, but is not something that is commonly associated with timber. As explained in the theory chapter, timber is not isotropic like steel, but is often regarded as orthotropic. To account for its direction dependency, orthotropic elasticity was assigned together with Hill's yield criterion. Hill's yield criterion allowed different yield strengths in shear and normal stress to be defined for the three orthotropic directions.

Physical testing was not conducted in this work, the material properties were therefore based on available literature. As a consequence of the material definition used for the timber, some of the properties proved to be difficult to obtain, especially for Dahurian larch. One reason is that the use of Dahurian larch is more confined to parts of China and Russia, which has led information to often be written in Chinese or Russian (Abaimov et al., 1998; Bergstedt et al., 2007). Some of the missing properties were therefore adopted from other wood species such as Douglas-fir and western larch.

4.6.1 Foundation material

The material properties for the foundation material were assumed to be of great importance to the model. The model had to be able to simulate the crushing behavior of the timber around the bolts, if deformations similar to the ones in the experiment were to occur. A method for determining the crushing properties of timber is by dowel bearing tests. One key property that can be derived from such tests is the effective elasticity of the timber. Dowel bearing tests show that the deformation of the timber is generally higher than that of uniaxial tests, indicating that the effective elasticity is lower. This is one of the properties that were difficult to find in the literature. Only two dowel bearing tests on Dahurain larch were found, conducted by R. Gupta and Vatovec (1996) and R. Yang et al. (2020). But they did not include the elasticity. The MOE had to be taken from Leitner (2011) who performed dowel bearing tests on Douglas-fir.

A comparative dowel bearing test needs to be done with the relevant timber species as well as with the same bolt diameter. This was an issue with the results from R. Gupta and Vatovec (1996), since a 19 mm (0.75in) bolt was used instead of a 6 mm bolt. The yield strength reported was 29 MPa parallel to grain and 13.2 MPa perpendicular to grain. This is much lower than the result by R. Yang et al. (2020), who reported an yield strength of 64.46 MPa parallel to grain and no result perpendicular to grain. R. Yang et al. (2020) used the same bolt diameter as the bolts in the model, but one problem with the test however, is that little information about how the data was evaluated is mentioned. Different methods exist to evaluate the embedment strength of timber. R. Gupta and Vatovec (1996) specifically stated that the reported dowel bearing capacity is the 5 % offset stress and included the ultimate stress reached in the test. But in some cases, the embedment strength is reported as the ultimate strength for the dowel bearing test (Wilkinson & (U.S.), 1991). The value from R. Yang et al. (2020) and R. Gupta and Vatovec (1996) were both tested, but the model experienced convergence issues with a yield strength of 64.46 MPa.

A significant part of the work by Leitner (2011) and Hong (2007) were dedicated to the use of calibration factors. These were used to calibrate the resulting properties from the dowel bearing tests, in order for the Ansys model to produce similar results. This was not possible in this work because of the lack of test data. A decision was made to proceed with the yield strength from R. Gupta and Vatovec (1996) as this made it possible for the solution to converge. Admittedly this will cause some inaccuracy in the results. But it suggests that the yield strength from Yang could not have been implemented directly in the model, without being calibrated first.

The values for the Poisson's ratios were found in the wood handbook by Forest Products Laboratory (2013). These however belonged to western larch, as values for Dahurian larch could not be found. The Poisson's ratios were important for calculating the shear moduli using the formula given by B. Yang (2005);

$$G = \frac{E}{2(1+\upsilon)} \tag{4.1}$$

Where:

$$E = \text{modulus of elasticity [Pa]}$$
$$\upsilon = \text{Poisson's ratio}$$

This was then used to calculate the shear yield strengths with the formulas used by (Leitner, 2011);

$$\gamma_{xy} = \gamma_{xz} = \frac{\sigma_y}{2(E_y - E_y^{'})}\sqrt{\frac{E_y}{G_{xy}}} \tag{4.2}$$

$$\gamma_{yz} = \frac{\sigma_y}{2(E_y - E_y^{'})}\sqrt{\frac{E_y}{G_{yz}}} \tag{4.3}$$

$$\tau_{xy} = \tau_{xz} = \gamma_{xy} G_{xy} \tag{4.4}$$

$$\tau_{yz} = \gamma_{yz} G_{yz} \tag{4.5}$$

Where:

γ_{xy} = shear yield strain parallel to grain
γ_{yz} = shear yield strain perpendicular to grain
σ_y = yield stress perpendicular to grain
E_y = elastic modulus perpendicular to grain
$E_y^{'}$ = tangent modulus perpendicular to grain
G_{xy} = shear modulus parallel to grain
G_{xz} = shear modulus perpendicular to grain
τ_{xy} = shear yield stress parallel to grain
τ_{yz} = shear yield stress perpendicular to grain

The stress ratios which need to be defined for the Hill yield criterion in Ansys can be calculated using the following equations from Arvidsson (2018);

$$R_{xx} = \frac{\sigma_{xx}^{y}}{\sigma_y} \tag{4.6}$$

$$R_{yy} = \frac{\sigma_{yy}^{y}}{\sigma_y} \tag{4.7}$$

$$R_{zz} = \frac{\sigma^y_{zz}}{\sigma_y} \tag{4.8}$$

$$R_{xy} = \sqrt{3}\frac{\tau^y_{xy}}{\sigma_y} \tag{4.9}$$

$$R_{yz} = \sqrt{3}\frac{\tau^y_{yz}}{\sigma_y} \tag{4.10}$$

$$R_{xz} = \sqrt{3}\frac{\tau^y_{xz}}{\sigma_y} \tag{4.11}$$

Table 4.3. Foundation material properties

Parameter	Value	Unit	Source
E_x	239	MPa	(Leitner, 2011)
E_y	120	MPa	(Leitner, 2011)
E_z	120	MPa	(Leitner, 2011)
E'_x	2.39	MPa	(Leitner, 2011)
E'_y	1.2	MPa	(Leitner, 2011)
E'_z	1.2	MPa	(Leitner, 2011)
G_{xy}	70.8	MPa	calculated
G_{yz}	43.4	MPa	calcluated
G_{xz}	70.8	MPa	calculated
σ_x	29	MPa	(R. Gupta & Vatovec, 1996)
σ_y	13.2	MPa	(R. Gupta & Vatovec, 1996)
σ_z	13.2	MPa	(R. Gupta & Vatovec, 1996)
τ_{xy}	5.1	MPa	calculated
τ_{yz}	4.0	MPa	calculated
τ_{xz}	5.1	MPa	calculated
υ_{xy}	0.276		(Forest Products Laboratory, 2013)
υ_{yz}	0.374		(Forest Products Laboratory, 2013)
υ_{xz}	0.292		(Forest Products Laboratory, 2013)
$\upsilon_{zy}*$	0.139		(Forest Products Laboratory, 2013)
$\sigma_{u,c}$	64.46	MPa	(R. Yang et al., 2020)
* - used for calculating the shear modulus			

4.6.2 General timber material

The task of finding the MOE for the general timber material surrounding the foundations was less challenging. MOE for Dahurian larch was available from various sources as results from uniaxial tests were more common than results from dowel bearing tests. The tangent moduli were calculated the same way as Leitner (2011) with 0.01*E. The yield strength parallel to grain however was not available, so the yield strength used by Leitner (2011) was adopted.

Table 4.4. General timber material properties

Parameter	Value	Unit	Source
E_x	13700	MPa	(R. Gupta & Ethington, 1996)
E_y	700	MPa	(Zhao & Zhao, 2015)
E_z	700	MPa	(Zhao & Zhao, 2015)
E'_x	137	MPa	calculated
E'_y	7	MPa	calculated
E'_z	7	MPa	calculated
G_{xy}	1359.7	MPa	calculated
G_{yz}	339	MPa	calculated
G_{xz}	1359.7	MPa	calculated
σ_x	39.9	MPa	(Leitner, 2011)
σ_y	13.2	MPa	(R. Gupta & Vatovec, 1996)
σ_z	13.2	MPa	(R. Gupta & Vatovec, 1996)
τ_{xy}	9.3	MPa	calculated
τ_{yz}	4.6	MPa	calculated
τ_{xz}	9.3	MPa	calculated
v_{xy}	0.276		(Forest Products Laboratory, 2013)
v_{yz}	0.374		(Forest Products Laboratory, 2013)
v_{xz}	0.292		(Forest Products Laboratory, 2013)
$v_{zy}*$	0.139		(Forest Products Laboratory, 2013)
$\sigma_{u,c}$	50.62	MPa	(R. Yang et al., 2020)
* - used for calculating the shear modulus			

4.7 Steel material properties

4.7.1 Bolts

The bolts in the experiment were of grade 6.8. This means an ultimate strength of no less than 600 MPa and a yield strength of 80 % of the ultimate strength. Strength tests of the bolts by R. Yang et al. (2020) however showed a yield strength lower than what was specified. The yield strength in the model was therefore selected to be the same value as the test results. The other parameters were kept the same as the steel material for the H-section which was a standard material in Ansys.

Table 4.5. Steel properties for the bolts

Parameter	Value	Unit
E	209.9	GPa
E'	1180	MPa
σ_y	425.35	MPa
K	174.92	GPa
G	80.731	GPa
σ_u	600	MPa
ν	0.3	

4.7.2 H-section

Q235 grade steel was used for the H-section in the experiment, compliant with the Chinese carbon steel standard GB/T-700. The Chinese standard subdivides the Q235 into four classes, A,B,C and D. In this case the properties remain the same as seen in table 4.6. A steel material included in the material library of Ansys called "Structural steel, S235J" was used. The material properties are shown in table 4.7.

Table 4.6. Q235 strength properties (National Standard Bureau, 2007)

<table>
<tr><th rowspan="4">Designation</th><th rowspan="4">Grade</th><th colspan="6">Yield Strength N/(mm^2)</th><th rowspan="4">Tensile Ultimate Strength N/(mm^2)</th></tr>
<tr><th colspan="6">Thickness of steel (mm)</th></tr>
<tr><th colspan="6">Not less than</th></tr>
<tr><th>≤ 16</th><th>>16-40</th><th>>40-60</th><th>>60-100</th><th>>100-150</th><th>>150</th></tr>
<tr><td>Q235</td><td>A
B
C
D</td><td>235</td><td>225</td><td>215</td><td>205</td><td>195</td><td>185</td><td>375-460</td></tr>
</table>

Table 4.7. Steel properties for the H-section

Parameter	Value	Unit
E	209.9	GPa
E'	1180	MPa
σ_y	253.8	MPa
K	174.92	GPa
G	80.731	GPa
σ_u	428.5	MPa
υ	0.3	

5. Results

5.1 Reaction forces

The reaction forces for the x-, y- and z-direction are plotted in figure 5.1 along with the load that was applied. The reaction force in the x-direction was identical to the applied load, which caused the two curves to overlap each other in the figure. Almost no force was present in the y-direction, while the z-direction experienced more force but considerably less than the in the x-direction.

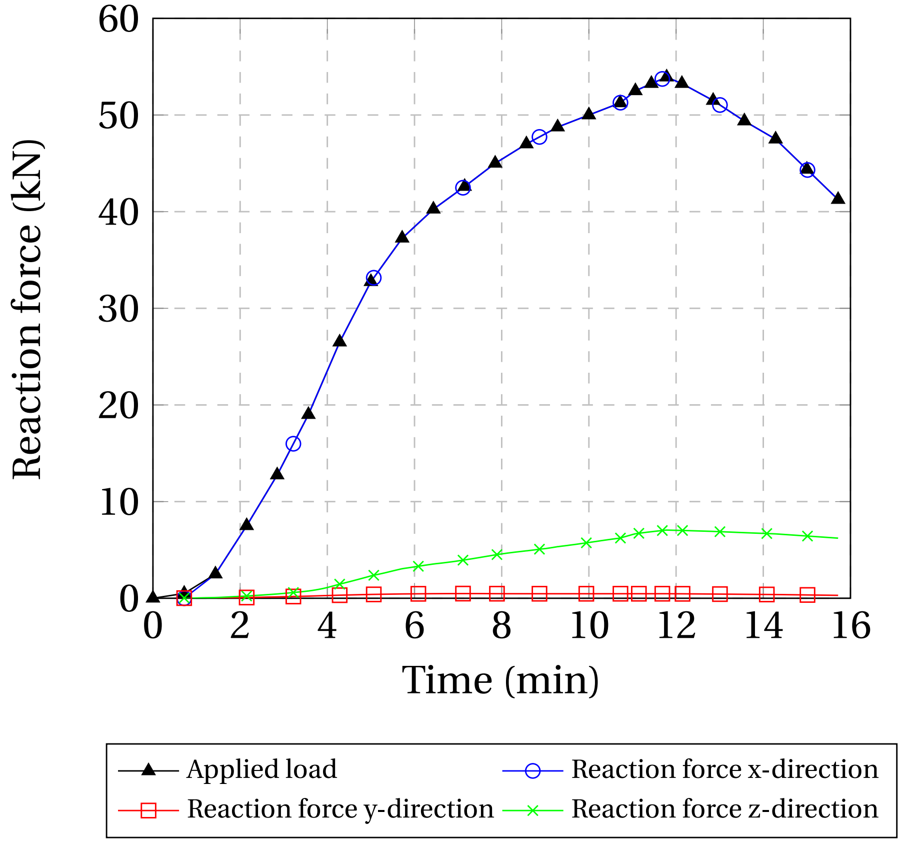

Fig. 5.1. Reaction forces in absolute values

5.2 Bolt pretension effect on load-slip

Figure 5.2 shows the results of the bolt pretension study that was done to investigate the relationship between the occurrence of no-slip and bolt pretension. The load-slip curve from the experiment is displayed in black. The bolt pretension of 0.5 kN produced the most similar result to the experiment by R. Yang et al. (2020). The following analyses in this study were therefore conducted using 0.5 kN as the bolt pretension.

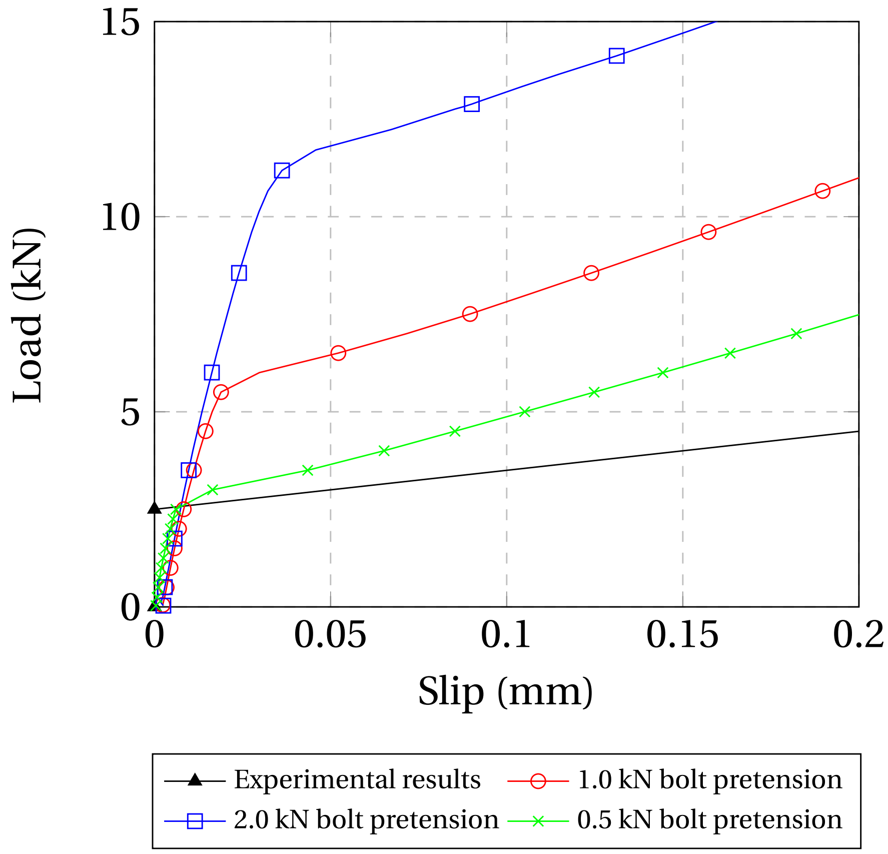

Fig. 5.2. Bolt pretension and no-slip zone

5.3 Large deflection on or off

A case where the large deflection option was turned on and a case where it was turned off was tested. The results for the two cases are displayed in figure 5.3. The figure shows that with large deflection off, the overall slip in the model increased compared to the case where it was active. Better agreement with the experimental results was achieved by activating the large deflection option, and was kept active for the rest of the work.

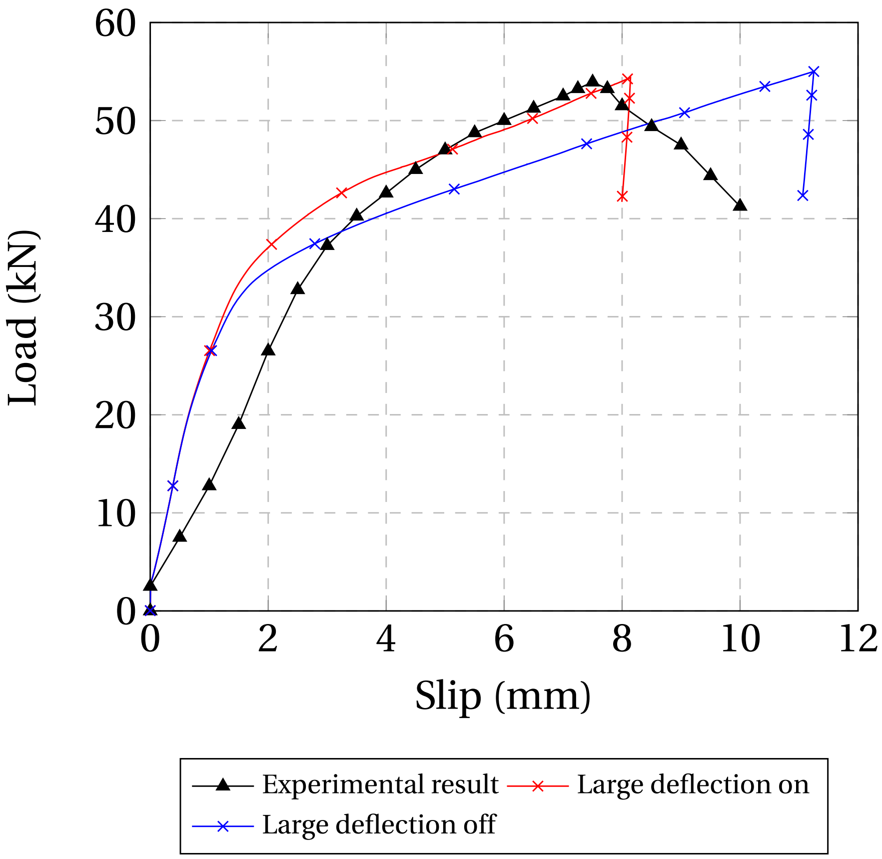

Fig. 5.3. Comparison between large deflection on and off

5.4 Mesh sensitivity study

Two different meshes with various refinement grades were tested to see what effect they had on the results. Table 5.1 highlights the distinct mesh settings for each case, the resulting node/element count and computational time. The load-slip curves are plotted in figure 5.4. The fine mesh provided the most similar result to the experiment of the two, while still completing the analysis within a reasonable time. As a consequence, the fine mesh was used for the model.

Table 5.1. Mesh sensitivity study results

	Bolt mesh		Foundation mesh				
Case	sweep size (mm)	body size (mm)	sweep size (mm)	body size (mm)	no. of face mesh divisions	node/ element count	time elapsed
Coarse	8	8	8	8	1	15603/ 2615	23m 11s
Fine	4	5	4	5	2	21193/ 3645	44m 45s

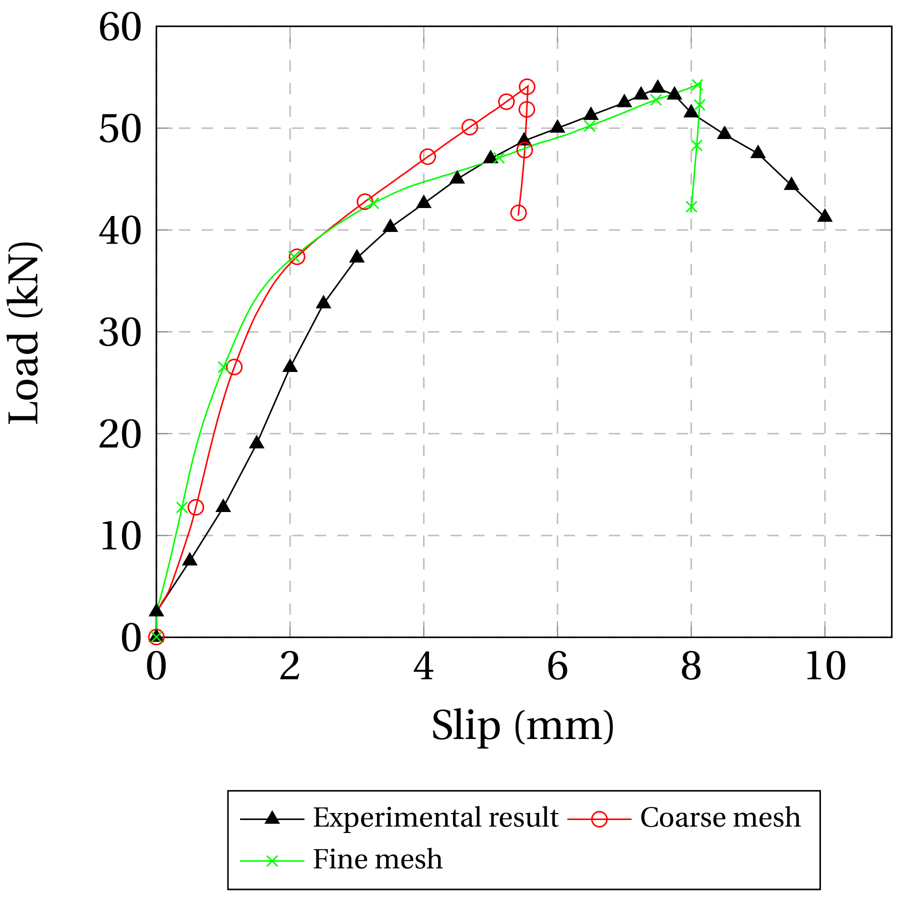

Fig. 5.4. Mesh influence on load-slip results

5.5 Linear and quadratic elements

In order to reduce the computational time of the model, lower-order linear hexagonal elements were tested. Table 5.2 show the node/element count as well as the computational time for the two cases. Linear elements required less time to complete the analysis, but the case with the quadratic elements provided more similar results to the experiment. The model was therefore meshed with quadratic elements.

Table 5.2. Element type influence on computational time

Case	Node/element count	Elapsed time
Linear elements	5913/3645	12 m 36 s
Quadratic elements	21193/3645	44 m 45 s

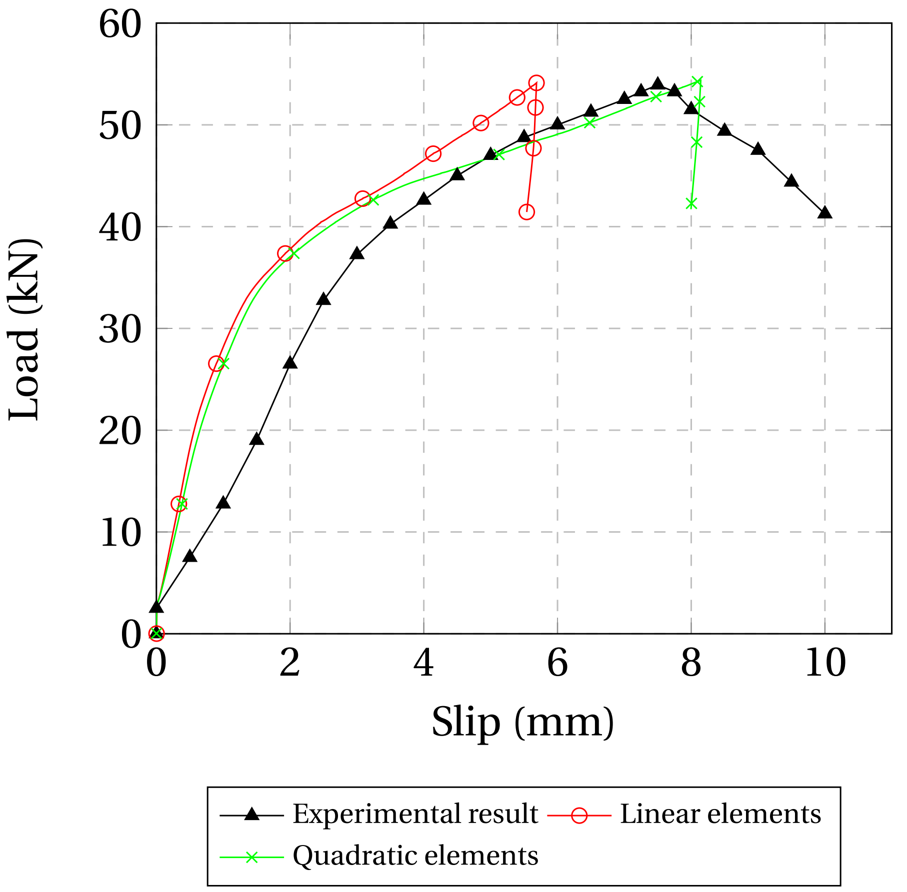

Fig. 5.5. Load-slip curves for linear and quadratic elements

5.6 Stress-strain results for the connection

The stress and strain results from each part of the element were investigated to determine if the model was able to capture plastic deformation, and if so where these deformations occurred. Figure 5.6 show the individual stress-strain curves for each part.

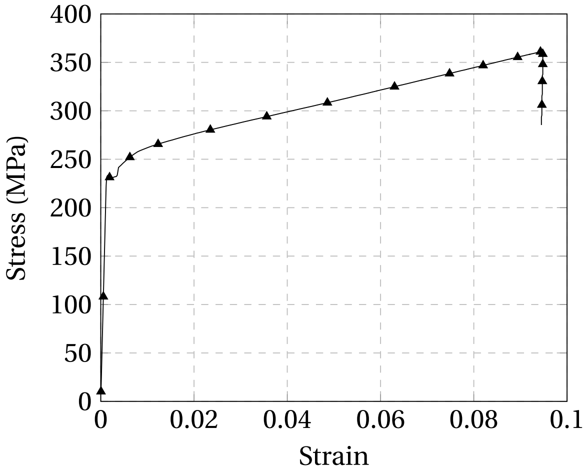

(a) Stress-strain curve H-section

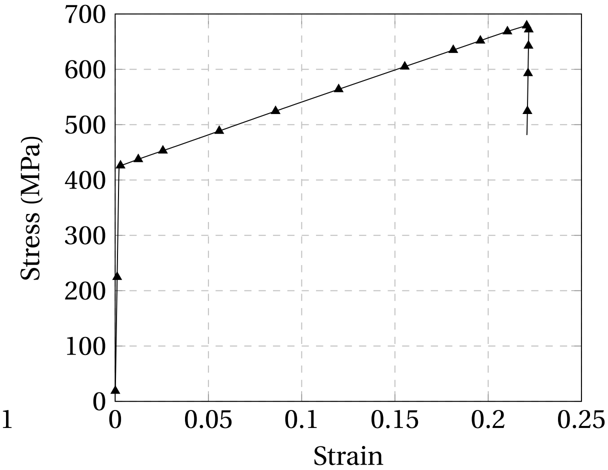

(b) Stress-strain curve bolt

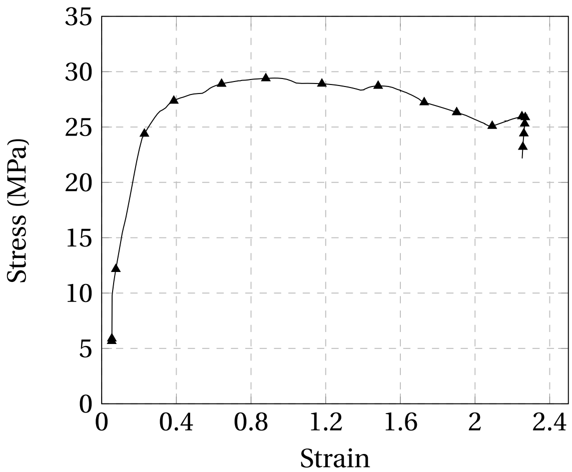

(c) Stress-strain curve foundations

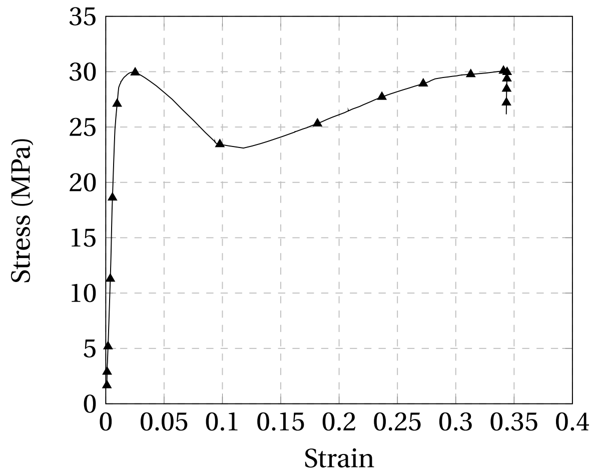

(d) Stress-strain curve lamellas

Fig. 5.6. stress-strain diagrams for each part of the model

5.7 Penetration results

Figure 5.7 show the penetration result for the bolt, and figure 5.8 show the penetration in the foundations.

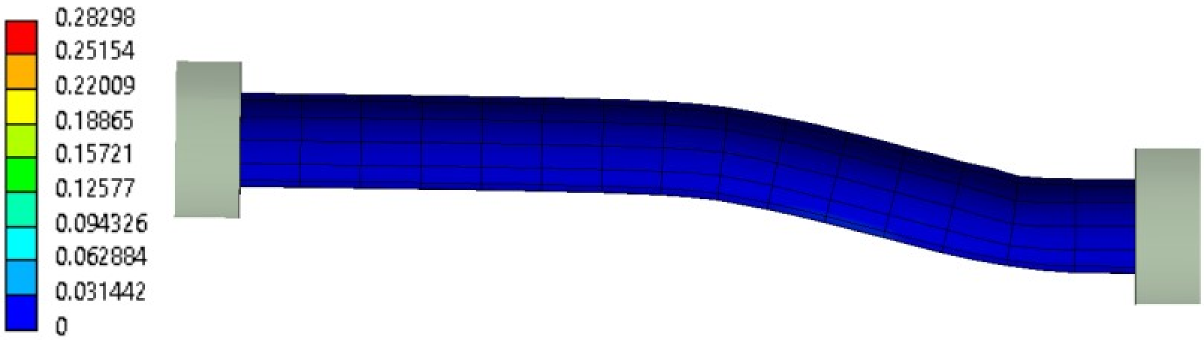

Fig. 5.7. Penetration of bolt t = 523 s (mm)

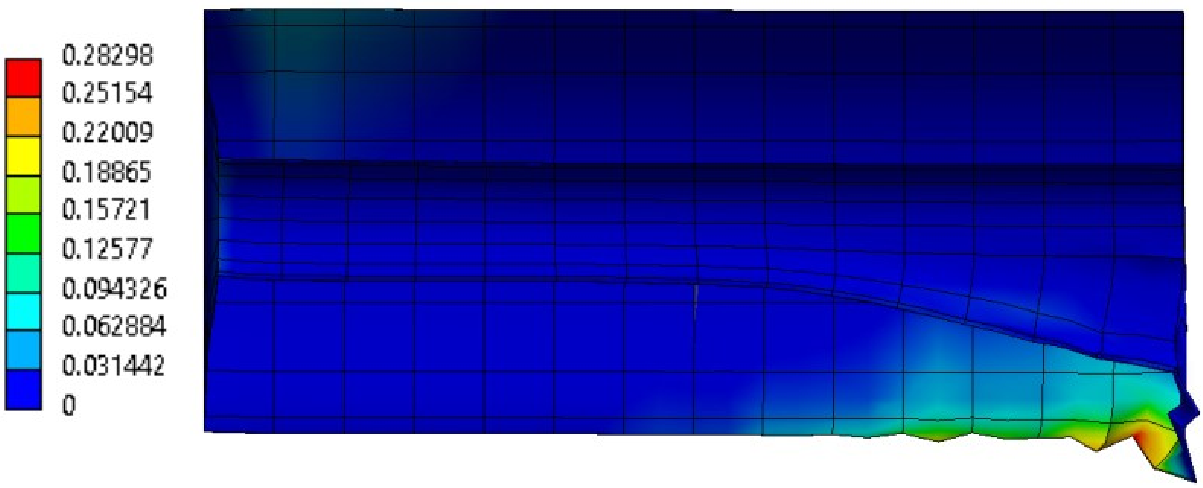

Fig. 5.8. Penetration of foundation t = 523 s (mm)

6. Discussion

6.1 Reaction forces

The model did not converge when constrained only in the x-direction. The use of additional constraints in the y- and z-direction as well helped the model reach convergence, suggesting that there was some instability in the first model. When increasing the number of constraints, the number of DOFs that Ansys have to consider reduces. Thus, Ansys does not have to account for the model moving in the y- and z-direction. This makes the set of equations in each iteration easier for Ansys to solve, and the total computational time reduces. A static structural analysis requires the model to be in static equilibrium. Rigid-body motion is, as mentioned, not permitted (ANSYS, Inc, 2010). The results in figure 5.1 confirmed that there were forces present in the other directions besides the x-direction. These forces however were small compared to the reaction force in the x-direction, but without constraints the model had difficulties establishing static equilibrium. This caused the model to be under-constrained which can explain why convergence was not reached initially.

Adding the two more constraints is an idealization of the experiment, where the test specimen was just supported in the x-direction. The reaction force results must therefore be assessed, to determine the impact this simplification might have on the solution. As the external load was only applied in the x-direction, the reaction force result should be governed mainly by the reaction force in the same direction. This is the case when checking the result, suggesting that that the model is working properly with regards to the constraints and the load being applied. If large forces were present in either the y- or the z-direction it could have indicated that there was something wrong in how the model was constrained or subjected to the load. Without the possibility to compare the results between the two constraint setups, due to the convergence issues. It is assumed that any inaccuracies caused by the extra constraints are minimal, as the main resulting reaction force in the x-direction is substantially larger than the other two forces. As the extra constraints led to convergence and less computational time, this simplification significantly benefited the model and was considered justifiable.

6.2 Bolt pretension effect on load-slip

As shown in figure 5.2, it appears that there is no slip at all at the start of the load regime. This may not be entirely accurate, as the results from the experiment had to be read off the curve provided in R. Yang et al. (2020). From the provided plot, it was not clear whether some minor slip had occurred or not. Nevertheless, the deformation was almost zero and the same can be said for the other pretensions that were tested. The curve marked in blue had the largest pretension of the three cases with 2.0 kN, and did also experience the largest no-slip zone. However, the no-slip zone was significantly larger than the experimental result. Reducing the pretension provided gradually more similar results to the experiment, and with 0.5 kN the result matched the curve from the experiment quite well.

It is important to emphasize that the purpose of the bolt-pretension study was not to determine the actual magnitude of the bolt pretension used in the experiment. Without the specified bolt pretension from the experiment, validation of the derived bolt pretension becomes impossible. The aim was to investigate the conclusion by R. Yang et al. (2020) whether the bolt pretension would cause no-slip and if this effect could be captured by the simulation. Several different magnitudes for the bolt pretension had to be tested, but the results show that the effect of the bolt pretension is similar to the effect it had in the experiment. There was no slip found initially and the bolt heads embedded themselves into the foundations in a realistic manner as seen in figure 6.5.

6.3 Large deflection on or off

The large deflection option showed an effect on the load-slip results for the model. When turned off, the slip became greater than the resulting slip from the experiment. By activating the large deflection option, the slip decreased and agreed better with the experimental result. This suggests that the deformation experienced in the model is great enough that it should be accounted for with regards to the stiffness. The model developed lower stiffness than expected with large deflection off, which indicates that the shape change of the elements caused the stiffness to increase.

6.4 Mesh sensitivity

The results in figure 5.4 showed that the two cases were initially similar. But as the load increased to around 40 kN, the dissimilarities became evident. This was the stage in the analysis where non-linear behaviour of the model began. The coarse mesh behaved the stiffest during this stage, and had the steepest load-slip curve until it reached the maximum load. The fine mesh had a flatter curve in this part of the load-slip analysis, which was almost parallel to the experimental result. The maximum load was reached at a slightly higher deformation than the experiment. For a linear analysis, both the coarse and fine mesh would provide similar results. But the coarse mesh would have taken half the time of the fine mesh to do so. Since the non-linear stage was of interest to this study, and the fine mesh showed enhanced accuracy, the fine mesh was selected for the model. A mesh study was done by Hassanieh et al. (2017), which produced similar results. The load-slip curves in the study would result in lower ultimate load as the meshes got finer.

One of the main challenges faced during the development of the model was distortion of the elements in the foundation, leading to convergence issues. Deformation of elements can cause the solution to fail when the distortion becomes so large, that the shape of the element is no longer compliant with the element type selected. The fine mesh case in figure 6.4 revealed that distortion was present, but small enough that convergence could be reached. However, distortion of any degree is not desirable, as it can cause abrupt local changes to the results. This effect is clearly seen in the stress-strain results for the lamellas, which will be discussed further in section 6.9

6.5 Linear and quadratic elements

From table 5.2 it was clear that the node count was much lower for the mesh with the linear elements, resulting in almost a quarter of the computational time for the medium mesh. The load-slip curves in figure 5.5 show that for the linear part of the analysis the results were nearly identical, but once the non-linear stage was reached they started to differ. The quadratic elements provided better accuracy which was expected as stated by Ferris (2020). The increase in integration points helped to capture the deformation of the elements in the foundation, while it seemed like the linear elements were acting too stiff. However, if only a linear analysis of the connection were to be performed, the reduced run time for the linear elements would be beneficial without sacrificing accuracy.

6.6 Failure mode

The stress-strain diagrams in figure 5.6 show that the only parts in the model that surpassed their ultimate strength were the bolts. The capacities of the bolts were specified as 600 MPa, which was reached before the peak load had been applied. A red line has been drawn from the 600 MPa mark in figure 6.2a, which intersects the stress-strain curve at about 0.15 strain. This corresponds to 523 seconds, or 8.72 minutes, into the loading regime which can be seen in the stress-time plot in figure 6.2b. The bolts failed when 47.5 kN had been applied as seen in figure 6.2c. This resulted in a slip of 5.4 mm. Similar to the experiment, the bolts in the model were the critical parts that failed first. However, the maximum load which the connection supported in the experiment was 54 kN, and around 7.5 mm slip had occurred at that point. This means that the capacity of the model is 88 % of that of the experiment, and therefore provides a conservative result.

Figure 6.1 shows that the maximum stress in the bolt occurred at the boundary between the H-section and the lamellas. This resulted in the development of a two-hinge yield of the bolt, which was the same failure mode reported in the experiment.

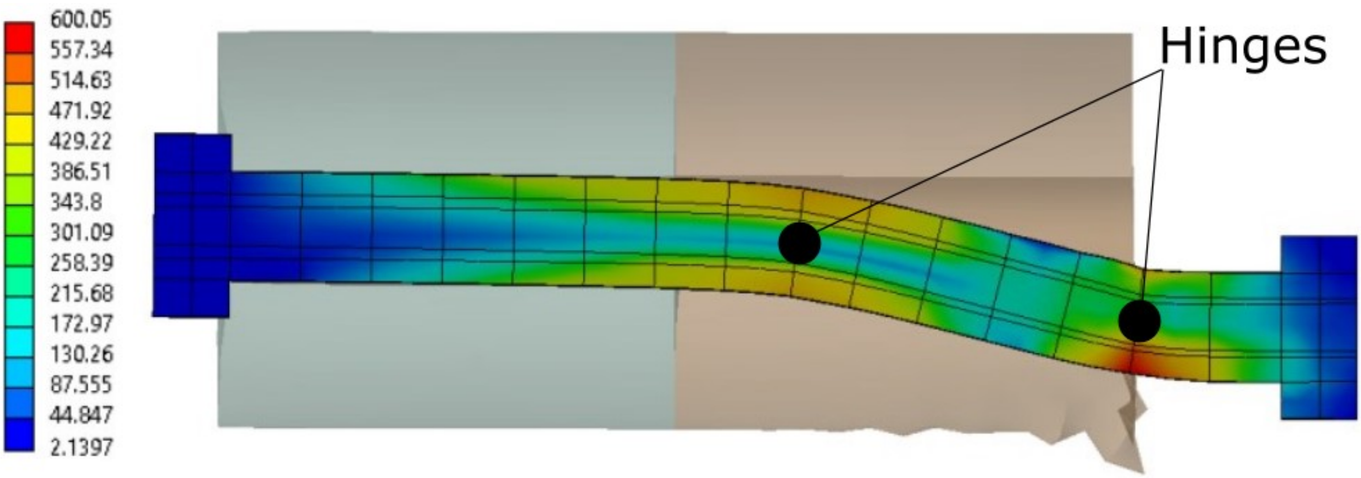

Fig. 6.1. Bolt failure location t = 523 s (MPa)

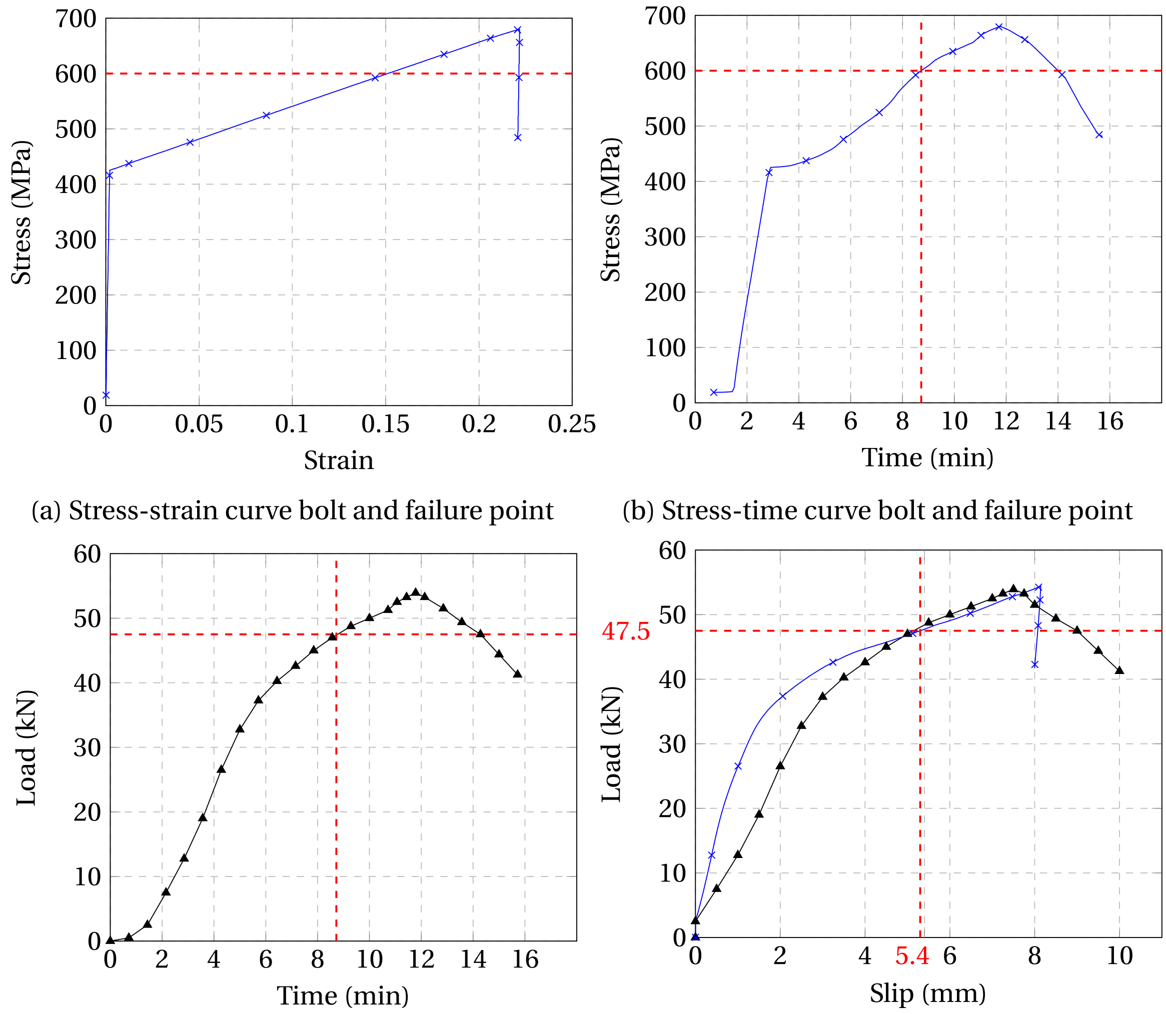

(a) Stress-strain curve bolt and failure point

(b) Stress-time curve bolt and failure point

(c) Applied load at failure

(d) Load-slip and failure point

Fig. 6.2. Load-slip and failure point results

6.7 Bolt and foundation deformation

The stress-strain diagram in figure 5.6c makes it clear that most of the deformation in the model occurred in the bolts and foundations. The deformation of the bolt at failure can be seen in figure 6.3, which showed that the mesh remains undistorted. However, the foundation seen in 6.4 showed some distortion in the elements at the edge of the hole. But still, the model was able to converge.

To the left in figure 6.4 it can be observed that the head of the bolt has embedded itself slightly into the foundation. This was caused by the pretension and propagated as the external load was applied. The resulting embedment of the bolt head can be seen in figure 6.5. Embedment of the bolt head was also observed in the experiment, but the resulting deformation was not provided.

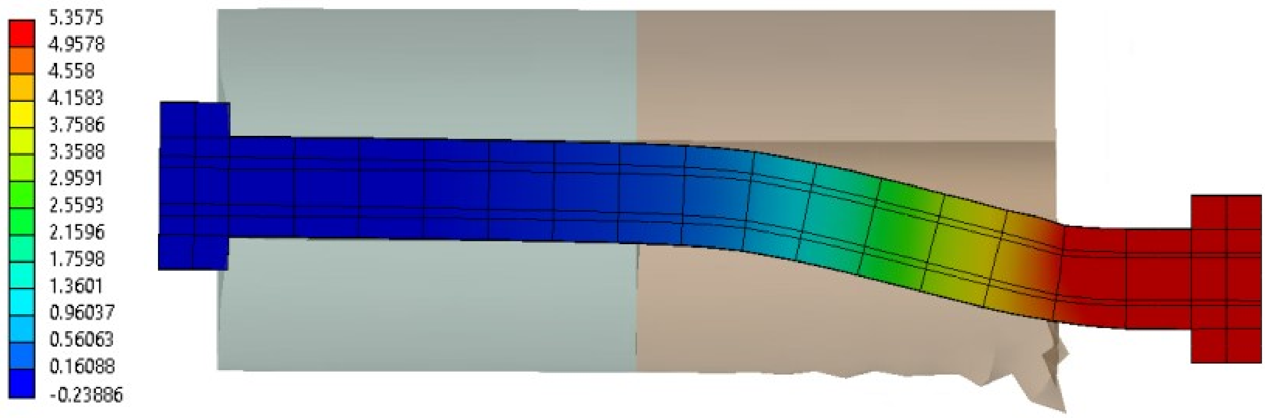

Fig. 6.3. Bolt deformation at failure t = 523 s (mm)

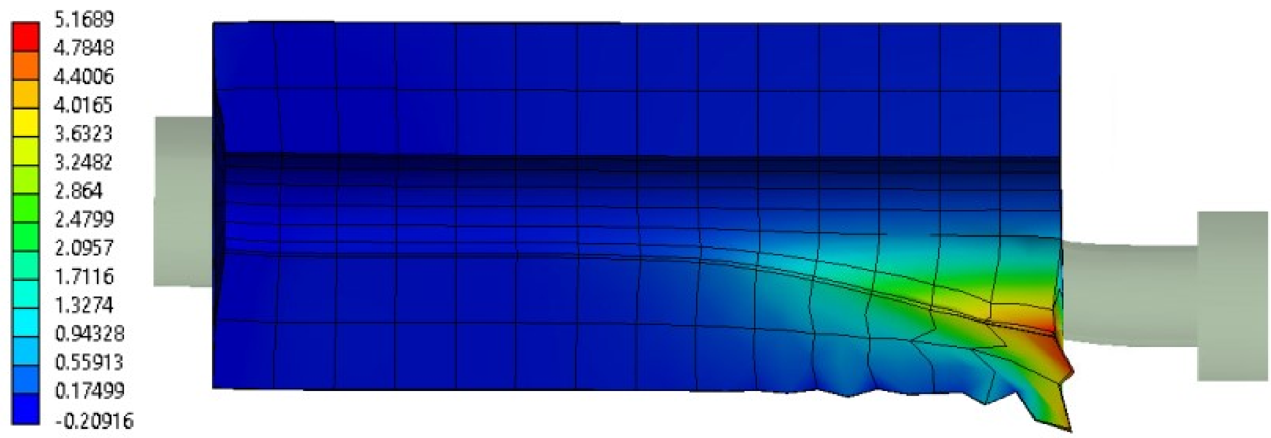

Fig. 6.4. Foundation deformation at failure t = 523 s (mm)

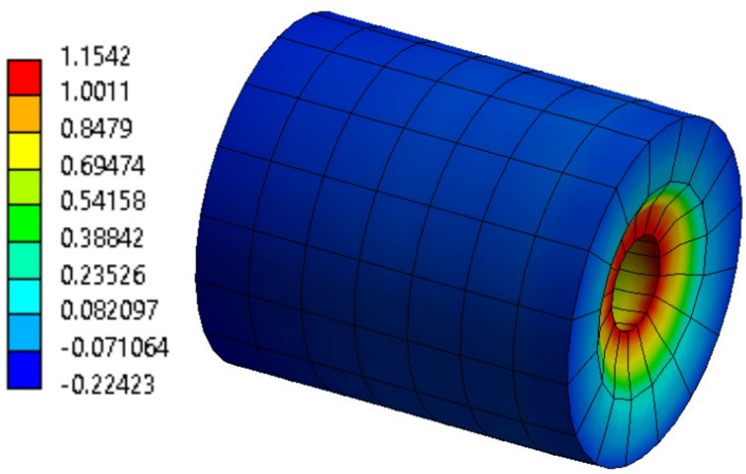

Fig. 6.5. Foundation deformation caused by embedment of bolt head t = 523 s (mm)

6.8 Stress-strain results for the connection

The largest contribution of strain came from the foundations as seen in figure 5.6c. The resulting strain was at 2.3 which was a lot higher than the strain for the other parts. This was not surprising, as the MOE for the foundation was much lower than the MOE for the steel and the general timber material in the rest of the lamellas. Figure 5.6b and 5.6a show that the bilinear isotropic hardening rules for the bolt and the H-section are working as intended, with the slope in the elastic region corresponding to the MOE and the slope of the plastic region corresponding to the tangent modulus. Yield occurred at the specified yield strengths for both the bolt and H-section.

In the experiment, it was reported no observable deformation of the H-section. The stress-strain plot seen in figure 2.7 however indicates that there was considerable strain present in the H-section in the model. Though, at a closer inspection of the plot from Ansys, it became clear that the strain was concentrated to the edge of the hole, with almost zero strain elsewhere. This can be seen in figure 6.6.

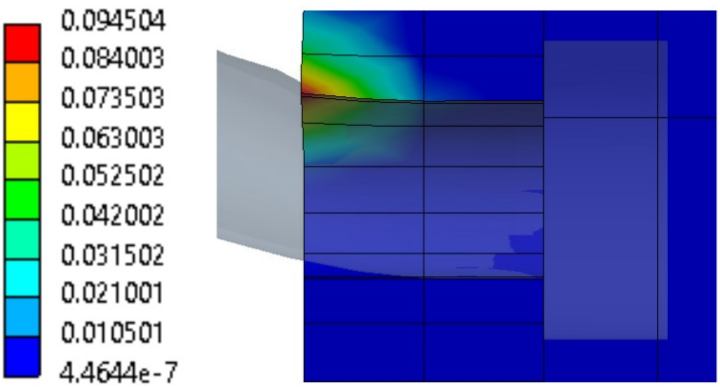

Fig. 6.6. Localized strain in the H-section t = 707 s

6.9 Lamella stress

The stress-strain curve in figure 5.6d for the lamellas experienced a sudden drop at around 0.1 strain. The stress-time curve for the lamellas has been plotted in figure 6.7. A stress peak was reached at 423 seconds, just before the stress reduction occurred. This was caused by the distortion of the elements beneath the foundation material as seen in figure 6.4. As the elements on the edge of the foundation got distorted, the elements in the lamellas were affected. Figure 6.8a show the stress contour plot in the lamellas at 423 seconds, where the elements have not yet been distorted. Figure 6.8b is of the same plot but at 61 seconds later. The elements underwent significant deformation, that resulted in a drop in stress. The stress then began to increase again as shown in figure 6.7.

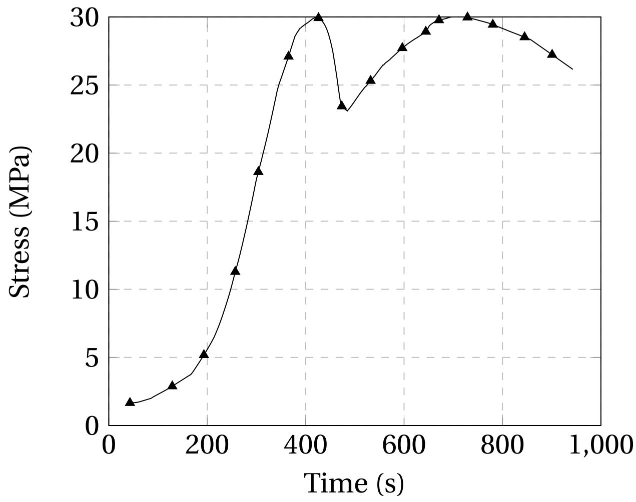

Fig. 6.7. Stress-time curve foundations

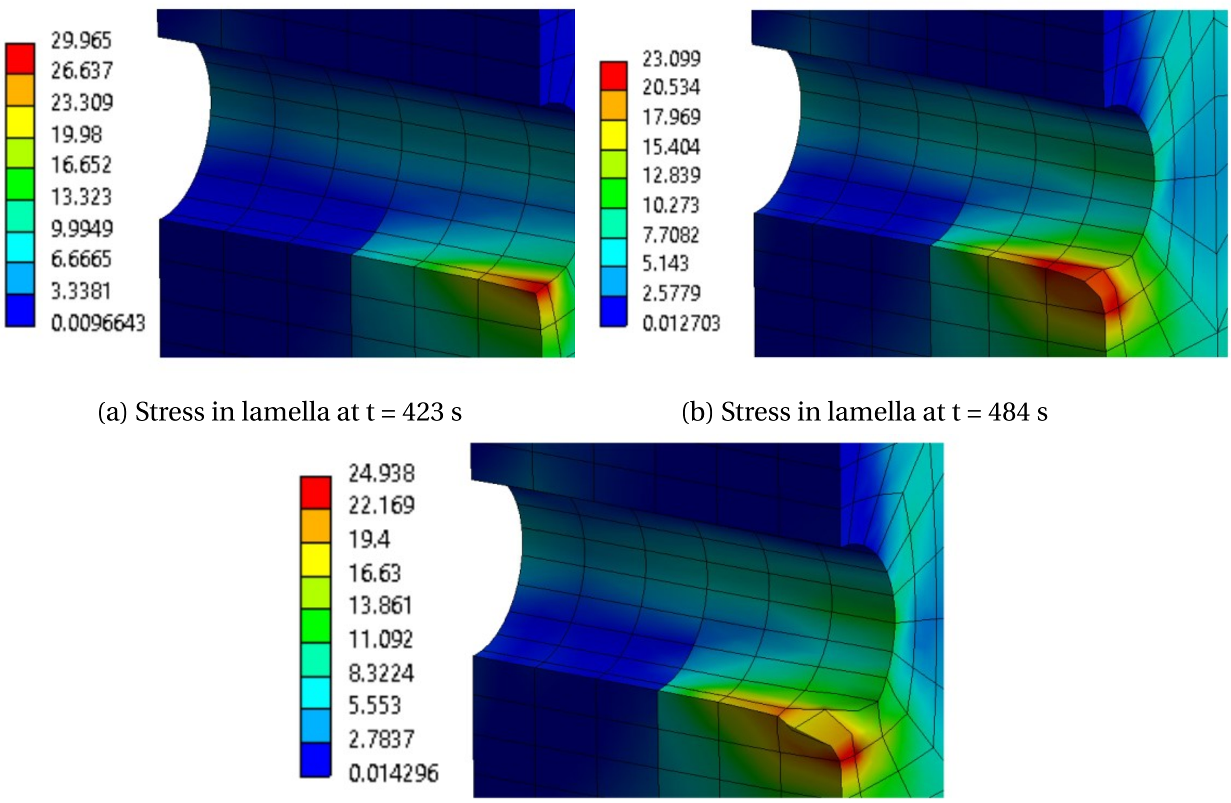

(a) Stress in lamella at t = 423 s

(b) Stress in lamella at t = 484 s

(c) Stress in lamella at t = 523 s

Fig. 6.8. Distortion effect on lamella stress
note: deformations have been scaled up by a factor of 4,7

6.10 Penetration results

As explained in chapter 4, the pure penalty formulation used for the contacts in the model, allows some penetration to occur. It is therefore necessary to assess the penetration, as it may cause unrealistic results. The penetration results of the bolt in figure 5.7 showed that no penetration occurred at the time of failure. The foundations on the other hand, showed penetration of almost 0.3 mm. This was confined to a small area near the most distorted elements at the edge of the hole. The fact that penetration was not present in the bolt is positive, as this would impact the load-slip results. Determining the significance of the penetration caused by the distorted elements however, is more difficult.

The largest contribution to the penetration result came from a single distorted element at the bottom of the foundation. Ideally, no distortion would have occurred. But the penetration would certainly be more alarming if more elements were involved. The impact this single element had on the results, could not easily be quantified. Factors such as the radius of the foundation and its material properties could potentially affect this behaviour. As physical tests were beyond the scope of this work, these factors had to be based on the studies mentioned in section 4.6.

6.11 Post-failure behaviour of the model

The load-slip curve for the model in figure 6.2d shows that after the ultimate load, the slip remains nearly constant at 8.0 mm. In contrast, the slip in experimental results increases. A total of six tests were performed with similar connection configurations, with each showing slight differences in post-failure behaviour. R. Yang et al. (2020) however, concluded that this effect was triggered by a combination of bolt and embedding failure, which caused the connection to be unable to bear the applied load.

The study by Hassanieh et al. (2017) included a model that successfully captured the post-failure behaviour of a similar connection made from CLT. A combination of continuum damage and plasticity for simulating the non-linear behaviour of timber was used. Included in the timber material definition was a separate softening rule for tension, which is initiated after a specified capacity is reached. This takes into account the brittle nature of timber in tension and its ductile nature in compression.

As stated in the aim of this work, the model was intended to simulate the behaviour of the connection up to the point of failure. This was viewed as more essential to engineering applications than the post-failure mode, as structural failure must always be avoided. What happens after the connection has failed, was therefore not a priority. Nevertheless, the model produced results for this stage of the analysis and were therefore discussed.

6.12 Limitations

The load-slip result in figure 6.2d is the basis for the accuracy evaluation of the model. It shows that the model provided promising results and produced a similarly shaped load-slip curve. There are however some inaccuracies, particularly with regards to the initial stiffness of the model and the reduced load capacity. The initial stiffness is higher than what was observed in the experiment. Thus, at this stage of the analysis the model overestimates the stiffness. When the model transitions into plastic behaviour, the results begin to agree better with the experiment. However, the bolts fail when 88 % of the capacity of the physical connection is reached. This is a conservative estimation, which is preferable to an overestimation of capacity. Still, the aim of this work was to simulate the behaviour of the connection as accurately as possible. A conservative result is positive, but improved accuracy is believed to be achievable if some of the limitations are addressed.

The main limitation to this work is that it is a strictly numerical study. The material properties were therefore based on available literature. Some of these properties are not commonly found, particularly the ones for the foundation material. Literature where dowel bearing strength tests had been performed on Dahurian larch with similar bolt diameter, could not be obtained. As a consequence, some values had to be taken from tests where a different timber species was tested, or where a different bolt diameter had been used. The foundation material was the main contributor to the deformation in the model. Its material properties have therefore a great effect on the load-slip results. Some of the most important properties include the MOEs and yield strengths. The MOEs belonged to douglas-fir tested by Leitner (2011), while the yield strengths stem from Dahurian larch tested by R. Gupta and Ethington (1996) but with larger bolts. The use of these material properties would have caused some inaccuracies in the results.

Another consequence of the lack of physical tests, is that calibration of the resulting properties from the dowel bearing tests is not possible. Both Hong (2007) and Leitner (2011) concluded that the inclusion of calibration factors was necessary, in order to implement the material properties in Ansys. The resulting properties from the tests did not provide sufficient accuracy. By comparing numerical models of the dowel bearing tests to the actual tests, calibration factors could be determined which improved the model accuracy. This also allowed them to investigate the size of the foundation material. A similar approach can be done with this model, which may result in improved accuracy. The material properties would also affect the localized distortion in the foundation material, which could potentially benefit the penetration results.

Clearance holes could not be accounted for in the model, because of convergence issues caused by the rigid-body motion of the bolts. For modelling purposes, the holes were therefore made to the same diameter as the bolts. This is likely to affect the connection stiffness, as the added clearance of 0.5 mm on all sides of the bolts, would have allowed them to rotate about the global y-axis as the load was applied. According to dos Santos et al. (2015) who investigated the influence of clearance holes on dowel-type connections, reduction of the clearance hole caused a slight increase in stiffness. They had a similar approach to the timber definition, using Hill's criterion. However, a smaller clearance of 0.3 mm was tested. A fair assumption would therefore be that the larger clearance of 0.5 mm seen in this case, would reduce the stiffness even further. As the initial stiffness seen for the model was too high, the effect of clearance holes could potentially provide a slight improvement of the accuracy.

7. Conclusion

The purpose of this thesis was to simulate the behaviour of a bolted STC connection subjected to a push-out test until failure, by conducting a FEA. The task of simulating the behaviour of timber is a complicated one, due to its inherent imperfections. The experimental load-slip results revealed that a considerable amount of non-linear deformation occurred before failure, which the model had to be able to consider. The predominant cause of this was localized crushing of the timber surrounding the bolts. The simulation of this effect, therefore, became one of the key objectives for this research.

The modelling approach selected for this task was based on the inclusion of a foundation material around the holes. This allowed a separate timber material definition to be assigned for this area, which could account for this localized deformation. A plasticity-based material definition, which included Hill's yield criterion, was used for the timber. The problem was modelled as a three-dimensional static structural analysis.

The model provided promising results, and it was able to capture the main observations from the experiment. The foundation material performed as intended and enabled localized non-linear deformation of the foundation material. A two-hinge yield failure mode of the bolts, similar to the failure mode seen in the experiment, was predicted by the model. An important result from the experiment was the occurrence of a no-slip zone at the beginning of the load-slip result. The model confirmed the comments made in the experiment, that this effect was caused by pretensioning of the bolts. Problem size-reduction measures, such as symmetry, made it possible to complete this analysis in less than an hour.

A conservative estimation of the connection capacity was provided by the model, which in most cases is desirable in engineering applications. The stiffness in the linear region on the other hand, was overestimated. But as the model entered the non-linear region, the results began to agree better with the experiment. A limiting factor was that no physical testing was conducted in this work. This meant that some uncertainties in the material properties for the timber could not be investigated. Dahurian larch glulam members were used in the experiment, but the availability of some of the properties proved to be scarce. Enhanced knowledge about these properties obtained through physical tests, would benefit the validation of the model, as well as facilitate for optimizations to be made.

With the growing interest in hybrid steel-timber construction worldwide, knowledge about the behaviour of STC connections and techniques to predict this behaviour is essential. This research has shown that the foundation material model is capable of simulating the complicated behaviour of a bolted STC connection, exerted in a pull-out test, with the use of modern FEM-software. The capacity as well as the associated deformation of the connection, were possible to calculate with significant accuracy. The use of FEM-software has become a standard practice in the civil engineering industry, which makes the approach presented in this work quite practical.

This work can hopefully contribute to expanding the knowledge on connections in hybrid steel-timber constructions, and how these can be approached with modern FEM-software. As the foundation material approach is a general modelling technique for dowel-type connections in timber, there is a potential for this to be applicable to other dowel-type timber connections. A room for further research into this field exists.

8. Further work

Although the model showed great potential in capturing the behaviour of the connection, there is room for improvements. To enable a better evaluation of the model accuracy, uncertainties concerning the material properties for Dahurian larch should be addressed. This can be done with the inclusion of physical testing, as this was the main limitation of this research.

The following approaches are recommended:

- Dowel bearing strength tests on Dahurian larch with appropriate dowel diameter should be performed. This would allow the orthogonal MOEs, yield and ultimate strengths for the foundation material to be determined.
- Uniaxial strength tests on Dahurian larch to determine the orthogonal MOEs, yield and ultimate strengths for the general timber material, should be conducted.

These tests should be accompanied by numerical studies, so that any necessary calibration of these properties can be done. This would also allow the size of the foundation material to be investigated.

The experiment by R. Yang et al. (2020) which this numerical study was based on, includes several different connection configurations. Various bolt diameters, bolt spacing, timber thicknesses and even self tapping screws were tested. Studying how these parameters affect the performance of the model, could also be of interest.

In addition, testing the validity of the model with other timber species and timber products can also be done. In that case, the use of relevant material properties is required.

Bibliography

Abaimov, A. P., Milyutin, L. I., Lesinski, J. A., & Martinsson, O. (1998). *Variability and ecology of siberian larch species.*

Abrahamsen, R., & Moelven Limtre AS. (2018). Mjøstårnet-18 storey timber building completed.

Ahmed, S., & Arocho, I. (2020). Mass timber building material in the u.s. construction industry: Determining the existing awareness level, construction-related challenges, and recommendations to increase its current acceptance level. *Cleaner Engineering and Technology, 1*, 100007. doi:10.1016/j.clet.2020.100007

ANSYS, Inc. (2004). Ansys contact technology guide. Release 9.0.

ANSYS, Inc. (2009). Theory reference for the mechanical apdl and mechanical applications. Release 12.0.

ANSYS, Inc. (2010). Lecture 3, introduction to contact. Release 13.0.

ANSYS, Inc. (2011). Ansys mechanical apdl element reference. Release 14.0.

ANSYS, Inc. (2020a). Ansys act customization guide for spaceclaim. Release 2020 R2.

ANSYS, Inc. (2020b). Ansys quick start licensing guide. Release 2020 R2.

ANSYS, Inc. (2020c). Ansys r2 2020 capabilities.

APA – The Engineered Wood Association. (n.d). *History of glulam.* Available at: https://www.apawood.org/apas-history. Accessed: 28.04.2021.

Arvidsson, D. (2018). *Additive weld manufacturing and material properties effect on structural margins* (M.Sc thesis). http://urn.kb.se/resolve?urn=urn:nbn:se:kth:diva-243881

ASME. (2010). *ASME B18.2.4.6M-2010: Metric Heavy Hex Nuts.* THE AMERICAN SOCIETY OF MECHANICAL ENGINEERS.

Atanackovic, T. M., & Guran, A. (2000). Hooke's law. *Theory of elasticity for scientists and engineers* (pp. 85–111). Birkhäuser Boston. doi:10.1007/978-1-4612-1330-7_3

Bathe, K. (2006). *Finite element procedures* (2.). Prentice Hall.

Bensabra, H., & Azzouz, N. (2013). Study of rust effect on the corrosion behavior of reinforcement steel using impedance spectroscopy. *Metallurgical and Materials Transactions A, 44*(13), 5703–5710. doi:10.1007/s11661-013-1915-4

Bergstedt, A., Lyck, C., & Landskab, S.
bibinitperiod. (2007). *Forest & landscape working papers: Larch wood - a literature review.* https://books.google.no/books?id=9nK%5C_oAEACAAJ

Bi, Z. (2017). *Finite element analysis applications: A systematic and practical approach.* Elsevier Science. https://books.google.no/books?id=fScsDwAAQBAJ

Boulbes, R. J. (2020). *Troubleshooting finite element modeling with abaqus.* Springer. doi:10.1007/978-3-030-26740-7

Bucalem, M. L., & Bathe, K.-J. (2011). Mathematical models and the finite element solution. hierarchical modeling. *The mechanics of solids and structures - hierarchical modeling and the*

finite element solution (pp. 1–17). Springer Berlin Heidelberg. doi:10.1007/978-3-540-26400-2_1
Cifuentes, A., & Kalbag, A. (1992). A performance study of tetrahedral and hexahedral elements in 3-d finite element structural analysis. *Finite Elements in Analysis and Design*, *12*(3), 313–318. doi:10.1016/0168-874X(92)90040-J
Clemens, H., Mayer, S., & Scheu, C. (2017). Microstructure and properties of engineering materials. doi:10.1002/9783527684489.ch1
Clough, R. W. (1980). The finite element method after twenty-five years: A personal view. *Computers Structures*, *12*(4), 361–370. doi:10.1016/0045-7949(80)90113-3
Clough, R. W. (1990). Original formulation of the finite element method. *Finite Elements in Analysis and Design*, *7*(2), 89–101. doi:10.1016/0168-874X(90)90001-U
Clough, R. (1960). *The finite element method in plane stress analysis*. American Society of Civil Engineers.
Clough, R., Wilson, E., & de Engenharia Civil (Portugal), L. N. (1962). *Stress analysis of a gravity dam by the finite element method*. Laboratório Nacional de Engenharia Civil. https://books.google.no/books?id=qUf-XwAACAAJ
Colby, R. B. (2013). *Equivalent plastic strain for the hill's yield criterion under general three-dimensional loading* (B.S thesis). Massachusetts Institute of Technology.
Courant, R. (1943). Variational methods for the solution of problems of equilibrium and vibrations. *Bulletin of the American Mathematical Society*, *49*(1), 1–23. doi:bams/1183504922
De Brito, J., & Kurda, R. (2021). The past and future of sustainable concrete: A critical review and new strategies on cement-based materials. *Journal of Cleaner Production*, *281*, 123558. doi:10.1016/j.jclepro.2020.123558
de Lumley, H. (1969). A paleolithic camp at nice. *Scientific American*, *220*(5), 42–51. http://www.jstor.org/stable/24926357
Domec, J.-C., & Gartner, B. L. (2002). How do water transport and water storage differ in coniferous earlywood and latewood? *Journal of Experimental Botany*, *53*(379), 2369–2379. doi:10.1093/jxb/erf100
dos Santos, C. L., de Jesus, A. M., & Morais, J. J. (2015). Embedment strength characterization of pine wood. numerical study of the non-linear behaviour. *Ciência Tecnologia dos Materiais*, *27*(1), 15–26. doi:10.1016/j.ctmat.2015.04.003
Eckelman, C., & Service, P. U. C. E. (2000). *The shrinking and swelling of wood and its effect on furniture*. Purdue University Cooperative Extension Service. https://books.google.no/books?id=-WEMPwAACAAJ
Embury, D. (2012). 8 - the formation of pearlite in steels. In E. Pereloma & D. V. Edmonds (Eds.), *Phase transformations in steels* (pp. 276–310). Woodhead Publishing. doi:10.1533/9780857096104.2.276
Farjon, A. (2010). *A handbook of the world's conifers*. Koninklijke Brill NV. doi:10.1163/9789047430629
Farris, T., Murthy, H., & Matlik, J. (2003). 4.11 - fretting fatigue. In I. Milne, R. Ritchie, & B. Karihaloo (Eds.), *Comprehensive structural integrity* (pp. 281–326). Pergamon. doi:10.1016/B0-08-043749-4/04080-5
Featherstone, S. (2015). 5 - metal containers for canned foods. In S. Featherstone (Ed.), *A complete course in canning and related processes (fourteenth edition)* (Fourteenth Edition, pp. 75–117). Woodhead Publishing. doi:10.1016/B978-0-85709-678-4.00005-1
Ferris, T. (2020). *3 steps to improve fea models*. Available at: https://www.ansys.com/blog/how-to-improve-fea. Accessed: 12.05.2021.
Forest Products Laboratory. (2013). *Wood handbook: Wood as an engineering material*. CreateSpace Independent Publishing Platform. https://books.google.no/books?id=NH3HAQAACAAJ

Garrison, W. (2001). Steels: Classifications. In K. J. Buschow, R. W. Cahn, M. C. Flemings, B. Ilschner, E. J. Kramer, S. Mahajan, & P. Veyssière (Eds.), *Encyclopedia of materials: Science and technology* (pp. 8840–8843). Elsevier. doi:10.1016/B0-08-043152-6/01587-4

Gedeon, M. (2012). *Yield strength and other near-elastic properties.* Materion Brush Performance Alloys.

Gonzaga, R. (2013). Influence of ferrite and pearlite content on mechanical properties of ductile cast irons. *Materials Science and Engineering: A, 567*, 1–8. doi:10.1016/j.msea.2012.12.089

Gross, H. (2013). *Glulam handbook volume 1* (Vol. 1). Skogsindustrierna – The Swedish Forest Industries Federation. https://www.woodcampus.co.uk/wp-content/uploads/2019/05/GLU_HAND_VOLUME-1.pdf

Gupta, K. K., & Meek, J. L. (1996). A brief history of the beginning of the finite element method. *International Journal for Numerical Methods in Engineering, 39*(22), 3761–3774. doi:10.1002/(SICI)1097-0207(19961130)39:22<3761::AID-NME22>3.0.CO;2-5

Gupta, R., & Ethington, R. L. (1996). General physical characteristics of dahurian larch (larix dahurica) from the russian far east. *Forest products journal, 46*(4), 90–93.

Gupta, R., & Vatovec, M. (1996). Evaluation of dahurian larchin mechanical connections. *Forest products journal, 46*(9), 89–93.

Hassanieh, A., Valipour, H., Bradford, M., & Sandhaas, C. (2017). Modelling of steel-timber composite connections: Validation of finite element model and parametric study. *Engineering Structures, 138*, 35–49. doi:10.1016/j.engstruct.2017.02.016

Haynes, R. J. (2017). Chapter three - significance and role of si in crop production. In D. L. Sparks (Ed.). Academic Press. doi:10.1016/bs.agron.2017.06.001

Hong, J. P. (2008). Wood material parameters of numerical model for bolted connections- compression properties and embedment properties. University of British Columbia.

Hong, J. P. (2007). *Three-dimensional nonlinear finite element model for single and multiple dowel-type wood connections* (PhD thesis). University of British Columbia. doi:10.14288/1.0066597

Hu, Q., Dewancker, B., Zhang, T., & Wongbumru, T. (2016). Consumer attitudes towards timber frame houses in china. *Procedia - Social and Behavioral Sciences, 216*, 841–849. doi:10.1016/j.sbspro.2015.12.081

IEA. (2019). *2019 global status report for buildings and construction.* United Nations Environment Programme.

Jokerst, R. (1981). *Finger-jointed wood products.* U.S. Department of Agriculture, Forest Service, Forest Products Laboratory. https://books.google.no/books?id=%5C_0ZrY12Pgd0C

Jones, D., & Ashby, M. (2005). *Engineering materials 2: An introduction to microstructures, processing and design.* Elsevier Science. https://books.google.no/books?id=wkOl953ZG-UC

Katz, J. L., Spencer, P., Wang, Y., Misra, A., Marangos, O., & Friis, L. (2008). On the anisotropic elastic properties of woods. *Journal of Materials Science, 43*(1), 139–145. doi:10.1007/s10853-007-2121-9

Keaton, J. R. (2018). Hooke's law. In P. T. Bobrowsky & B. Marker (Eds.), *Encyclopedia of engineering geology* (pp. 488–489). Springer International Publishing. doi:10.1007/978-3-319-73568-9_157

Kelly, P. (2013). Solid mechanics. *Part I, Lecture notes.* University of Auckland.

Leitner, E. J. (2011). *Three-dimensional modeling of wood moment connections* (M.Sc thesis). Pennsylvania State University.

Leśko, A. (2021). Environment impact on the humidity change of beams from timber and glulam - experimental investigation. *IOP Conference Series: Materials Science and Engineering, 1015*(1), 012076. doi:10.1088/1757-899x/1015/1/012076

Lin, B., Zhang, Z., & Ge, F. (2017). Energy conservation in china's cement industry. *Sustainability, 9*(4), 668. doi:10.3390/su9040668

Loss, C., Piazza, M., & Zandonini, R. (2016). Connections for steel–timber hybrid prefabricated buildings. part i: Experimental tests. *Construction and Building Materials, 122*, 781–795. doi:10.1016/j.conbuildmat.2015.12.002

Mckenzie, W. M., & Karpovich, H. (1968). The frictional behaviour of wood. *Wood Science and Technology, 2*(2), 139–152. doi:10.1007/bf00394962

Miller, H., & Mattuck, A. (2010). *Differential equations.* Massachusetts Institute of Technology: MIT OpenCourseWare. https://ocw.mit.edu/courses/mathematics/18-03-differential-equations-spring-2010/#

Mleziva, M., & Wang, J. (2012). 10.23 - paper. In K. Matyjaszewski & M. Möller (Eds.), *Polymer science: A comprehensive reference* (pp. 397–410). Elsevier. doi:10.1016/B978-0-444-53349-4.00274-0

Moelven Limtre AS. (n.d). *Glulam.* Available at: https://www.moelven.com/about-moelven/glulam/. Accessed: 28.04.2021.

Moody, R. C., & Hernandez, R. (1997). Glued-laminated timber. In S. Smulski (Ed.), *Engineered wood products: A guide for specifiers, designers and users* (pp. 1–39). PFS Research Foundation.

Morris, J. W. (2001). *The influence of grain size on the mechanical properties of steel.* doi:10.2172/861397

National Standard Bureau. (2007). *GB/T 700-2006: Carbon Structural Steels.* National Standard Bureau. China.

Nguyen, H. T., & Kim, S. E. (2009). Finite element modeling of push-out tests for large stud shear connectors. *Journal of Constructional Steel Research, 65*(10), 1909–1920. doi:10.1016/j.jcsr.2009.06.010

Nouri, F., Valipour, H., & Bradford, M. (2019). Structural behaviour of steel-timber composite (stc) beam-to-column connections with double angle web cleats subjected to hogging bending moment. *Engineering Structures, 192*, 1–17. doi:10.1016/j.engstruct.2019.04.092

Pichler, P., Leitner, M., Grün, F., & Guster, C. (2018). Evaluation of wood material models for the numerical assessment of cutting forces in chipping processes. *Wood Science and Technology, 52*(1), 281–294. doi:10.1007/s00226-017-0962-1

Pint, B. A., Dryepondt, S., Put, A. R.-V., & Zhang, Y. (2012). Mechanistic-based lifetime predictions for high-temperature alloys and coatings. *JOM, 64*(12), 1454–1460. doi:10.1007/s11837-012-0474-2

Plevris, V., & Tsiatas, G. C. (2018). Computational structural engineering: Past achievements and future challenges. *Frontiers in Built Environment, 4.* doi:10.3389/fbuil.2018.00021

Pouzet, M., Dubois, M., Charlet, K., & Béakou, A. (2018). From hydrophilic to hydrophobic wood using direct fluorination: A localized treatment. Second Colloque français de chimie du fluor. *Comptes Rendus Chimie, 21*(8), 800–807. doi:10.1016/j.crci.2018.03.009

Ramage, M. H., Burridge, H., Busse-Wicher, M., Fereday, G., Reynolds, T., Shah, D. U., Wu, G., Yu, L., Fleming, P., & Densley-Tingley, D. (2017). The wood from the trees: The use of timber in construction. *Renewable and Sustainable Energy Reviews, 68*, 333–359. doi:10.1016/j.rser.2016.09.107

Rao, J. S. (2011). Fundamentals of elasticity. *History of rotating machinery dynamics* (pp. 45–47). Springer Netherlands. doi:10.1007/978-94-007-1165-5_9

Ravazzolo, F., & Vespignani, J. L. (2017). World steel production: A new monthly indicator of global real economic activity. *SSRN Electronic Journal.* doi:10.2139/ssrn.2992983

Richter, C. (2015). The anatomical structure of wood. *Wood characteristics: Description, causes, prevention, impact on use and technological adaptation* (pp. 3–5). Springer International Publishing. doi:10.1007/978-3-319-07422-1_1

Rohan, P., Lobos, C., Nazari, M. A., Perrier, P., & Payan, Y. (2017). Finite element models of the human tongue: A mixed-element mesh approach. *Computer Methods in Biomechanics and Biomedical Engineering: Imaging & Visualization*, *5*(6), 390–400. doi:10.1080/21681163.2015.1105760

Schober, K.-U., & Tannert, T. (2016). Hybrid connections for timber structures. *European Journal of Wood and Wood Products*, *74*(3), 369–377. doi:10.1007/s00107-016-1024-3

Sedlák, P., Seiner, H., Zídek, J., Janovská, M., & Landa, M. (2014). Determination of all 21 independent elastic coefficients of generally anisotropic solids by resonant ultrasound spectroscopy: Benchmark examples. *Experimental Mechanics*, *54*(6), 1073–1085. doi:10.1007/s11340-014-9862-6

Serano, E., Kliger, R., Hansson, F., Eva, Danielsson, H., Mårtensson, A., Crocetti, R., & Piazza, M. (2015). *Limtreboka* (B. Edlund, Ed.; Vol. 2). Norske Limtreprodusenters Forening.

Shmulsky, R., & Jones, P. D. (2011). Composition and structure of wood cells. *Forest products and wood science an introduction* (pp. 45–63). John Wiley Sons, Ltd. doi:10.1002/9780470960035.ch3

Song, J., Park, J., Kwon, S., & Chung, B. (2002). Idealization in physics: Its types, roles and implications to physics learning.

Sperry, J., Hacke, U., & Pittermann, J. (2006). Size and function in conifer tracheids and angiosperm vessels. *American journal of botany*, *93 10*, 1490–500.

Stein, E. (2014). History of the finite element method – mathematics meets mechanics – part i: Engineering developments. In E. Stein (Ed.), *The history of theoretical, material and computational mechanics - mathematics meets mechanics and engineering* (pp. 399–442). Springer Berlin Heidelberg. doi:10.1007/978-3-642-39905-3_22

The Editors of Encyclopedia Britannica. (2016). *Tracheid*. Available at: https://www.britannica.com/science/tracheid. Encyclopedia Britannica. Accessed: 26.04.2021.

Thompson, M. K., & Thompson, J. M. (2017). Chapter 1 - introduction to ansys and finite element modeling. In M. K. Thompson & J. M. Thompson (Eds.), *Ansys mechanical apdl for finite element analysis* (pp. 1–9). Butterworth-Heinemann. doi:10.1016/B978-0-12-812981-4.00001-0

Toppinen, A., Röhr, A., Pätäri, S., Lähtinen, K., & Toivonen, R. (2018). The future of wooden multistory construction in the forest bioeconomy – a delphi study from finland and sweden. *Journal of Forest Economics*, *31*, 3–10. doi:10.1016/j.jfe.2017.05.001

Tsalkatidis, T., Amara, Y., Embaye, S., & Nathan, E. (2018). Numerical investigation of bolted hybrid steel-timber connections. *Frontiers in Built Environment*, *4*. doi:10.3389/fbuil.2018.00048

Tu, S., Ren, X., He, J., & Zhang, Z. (2020). Stress–strain curves of metallic materials and post-necking strain hardening characterization: A review. *Fatigue Fracture of Engineering Materials Structures*, *43*(1), 3–19. doi:10.1111/ffe.13134

Turner, M. J., Clough, R. W., Martin, H. C., & Topp, L. (1956). Stiffness and deflection analysis of complex structures. *journal of the Aeronautical Sciences*, *23*(9), 805–823.

Union, E. (2003). Wood fibre cell wall structure. https://cordis.europa.eu/project/id/E20

Vaidya, A., & Pathak, K. (2019). 17 - mechanical stability of dental materials. In A. M. Asiri, Inamuddin, & A. Mohammad (Eds.), *Applications of nanocomposite materials in dentistry* (pp. 285–305). Woodhead Publishing. doi:10.1016/B978-0-12-813742-0.00017-1

Valipour, H. (n.d). *The future is multiple: Hybrid and composite steel-timber-concrete structures.* Available at: https://www.cies.unsw.edu.au/the-future-is-multiple-hybrid-and-composite-steel-timber-concrete-structures. Accessed: 26.05.2021.

Vannucci, P. (2018). General anisotropic elasticity. *Direct methods* (pp. 19–73). Direct Methods. doi:10.1007/978-981-10-5439-6_2

Vogiatzis, T., Tsalkatidis, T., & Avdelas, A. (2019). Steel framed structures with cross laminated timber infill shear walls and semi-rigid connections. *International Journal of Engineering Technology*, *8*(4), 433. doi:10.14419/ijet.v8i4.29742

Voort, G. F. V. (2014). Measurement of grain shape uniformity. *Practical Metallography*, *51*(5), 367–374. doi:10.3139/147.110290

Wheeler, E. (2001). Wood: Macroscopic anatomy. In K. J. Buschow, R. W. Cahn, M. C. Flemings, B. Ilschner, E. J. Kramer, S. Mahajan, & P. Veyssière (Eds.), *Encyclopedia of materials: Science and technology* (pp. 9653–9657). Elsevier. doi:10.1016/B0-08-043152-6/01749-6

Wickeler, A. L., & Naguib, H. E. (2020). Novel origami-inspired metamaterials: Design, mechanical testing and finite element modelling. *Materials Design*, *186*, 108242. doi:10.1016/j.matdes.2019.108242

Wilkinson, T., & (U.S.), F. P. L. (1991). *Dowel bearing strength.* U.S. Department of Agriculture, Forest Service, Forest Products Laboratory. https://books.google.no/books?id=ys9tVB0l2hcC

Woodard, A., & Milner, H. (2016). 7 - sustainability of timber and wood in construction. In J. M. Khatib (Ed.), *Sustainability of construction materials (second edition)* (Second Edition, pp. 129–157). Woodhead Publishing. doi:10.1016/B978-0-08-100370-1.00007-X

Yang, B. (2005). 5 - stress analysis in two-dimensional problems. In B. Yang (Ed.), *Stress, strain, and structural dynamics* (pp. 135–156). Academic Press. doi:10.1016/B978-012787767-9/50006-4

Yang, H., Gavras, S., & Dieringa, H. (2021). Creep characteristics of metal matrix composites. *Reference module in materials science and materials engineering.* Elsevier. doi:10.1016/B978-0-12-803581-8.11822-3

Yang, J., Hu, Y., & Wang, Q. (2019). Investigation of effective thermal conductivity for ordered and randomly packed bed with thermal resistance network method. *Energies*, *12*(9), 1666. doi:10.3390/en12091666

Yang, R., Li, H., Lorenzo, R., Ashraf, M., Sun, Y., & Yuan, Q. (2020). Mechanical behaviour of steel timber composite shear connections. *Construction and Building Materials*, *258*, 119605. doi:https://doi.org/10.1016/j.conbuildmat.2020.119605

Yang, Y., Raipala, K., & Holappa, L. (2014). Chapter 1.1 - ironmaking. In S. Seetharaman (Ed.), *Treatise on process metallurgy* (pp. 2–88). Elsevier. doi:10.1016/B978-0-08-096988-6.00017-1

Younis, W. (2010). Chapter 9 - the stress analysis environment. In W. Younis (Ed.), *Up and running with autodesk inventor simulation 2011 (second edition)* (Second Edition, pp. 235–275). Butterworth-Heinemann. doi:10.1016/B978-0-12-382102-7.10009-1

Zadpoor, A., Sinke, J., & Benedictus, R. (2011). 4 - numerical simulation modeling of tailor welded blank forming. In B. L. Kinsey & X. Wu (Eds.), *Tailor welded blanks for advanced manufacturing* (pp. 68–94). Woodhead Publishing. doi:10.1533/9780857093851.1.68

Zhao, J., & Zhao, D. (2015). Two-dimensional heterogeneous lattice model simulation of tensile fracture in dahurian larch. *Materials Research Innovations*, *19*(sup5), S5-941-S5–947. doi:10.1179/1432891714Z.0000000001226

Zhou, G., Wang, Y., Jiang, Y., & Yang, Z. (2002). Estimating biomass and net primary production from forest inventory data: A case study of china's larix forests. The Role of Boreal Forests and Forestry in the Global Carbon Budget. *Forest Ecology and Management*, *169*(1), 149–157. doi:https://doi.org/10.1016/S0378-1127(02)00305-5

Zohdi, T. I. (2018). Weighted residuals and galerkin's method for a generic 1d problem. *A finite element primer for beginners: The basics* (pp. 1–4). Springer International Publishing. doi: 10.1007/978-3-319-70428-9_1

Zrnik, J., Pippan, R., Scheriau, S., Kraus, L., & Fujda, M. (2010). Microstructure and mechanical properties of ufg medium carbon steel processed by hpt at increased temperature. *Journal of Materials Science*, *45*(17), 4822–4826. doi:10.1007/s10853-010-4482-8

Norges miljø- og biovitenskapelige universitet
Noregs miljø- og biovitskapelege universitet
Norwegian University of Life Sciences

Postboks 5003
NO-1432 Ås
Norway